REMOTE MEASUREMENTS OF VOLCANIC GASES USING THERMAL INFRARED HYPERSPECTRAL IMAGING

A DISSERTATION SUBMITTED TO THE GRADUATE DIVISION OF THE UNIVERSITY OF HAWAI‘I AT MĀNOA IN PARTIAL FULFILLMENT OF THE REQUIREMENTS FOR THE DERGEE OF

DOCTOR OF PHILOSOPHY

IN

GEOLOGY AND GEOPHYSICS

April 2018

By

Andrea Gabrieli

Dissertation Committee:

Robert Wright, Chairperson

Paul G. Lucey

John N. Porter

Steven Howell

Scott Rowland

Keywords: volcano, Sulfur Dioxide, flux, ground-based retrieval, Hyperspectral Imaging, InfraRed (IR), inversion algorithm, Partial Least Squares Regression (PLSR)

ACKNOWLEDGEMENTS

As I was finishing my Masters of Science in Volcanology and Geological Hazards at the British University of Lancaster, I could have never thought that my dream of living in Hawai'i to study Hawaiian volcanism was going to become true. Even if I was not thinking of challenging myself with a PhD at that time, when my supervisor Lionel Wilson suggested me to apply for a geophysics and remote sensing PhD in Hawai'i, I accepted his recommendation and contacted Robert Wright, another British scientist who was soon to become my PhD advisor. This was the beginning of an exciting adventure that could not have been successful without the help of the many mentors and friends I had during this challenging time.

In the first place, I want to thank my advisor Robert Wright for this great opportunity, his impressive knowledge, excellent guidance, patient help and clever British humor.

A big thank you or 'mahalo' as the Hawaiians would say to my PhD dissertation committee members: Paul Lucey, John Porter, Steven Howell and Scott Rowland for their excellent suggestions and comments. Their constructive feedback led to an improvement of the work. I particularly thank Paul for his endless creative ideas and John for all the fun time we had together and his precious help for the realization of the Partial Least Squares Regression Algorithm for SO_2 gas retrievals, described in this work.

Mahalo to my comprehensive exam committee members as well: Julia Hammer and Clinton Conrad. I learned a lot from them.

I thank my friends and collaborators Harold Garbeil, Mark Wood, Eric Pilger, Casey Honnibal, Tim Williams and Ethan Kastner for their help in the laboratory and in the field. I specifically want to thank Harold and Mark for their great technical help and assistance.

This PhD experience involved a great amount of administrative work, which has been made easy by Vi Nakahara, Grace Furuya, Karynne Morgan, Rena Lefevre, Susan Van Gorder, Lily Shao, Mars Rei S. Nii and Bill Doi. Many thanks to all of them.

Mahalo to Mario Williamson for his help designing the gas cells described in this dissertation.

I am particularly grateful to Ken Rubin, Mike Garcia and the Department of Geology and Geophysics for their support. I have been awarded two scholarships over the past three years: the Graduate Achievement Award in 2016 and the J. Watumull Merit Scholarship in Geology and Geophysics in 2017.

My deepest gratitude goes to Matt Patrick (Hawai'i Volcanoes Observatory) for his logistics and knowledgeable support on the summit of Kīlauea volcano as we made several expeditions to the active lava lake Halema'uma'u.

I also thank Matt Blackett (Coventry University, UK), for his help with part of the field data collection, and Alexander Berk (Spectral Sciences Inc.) for his insightful suggestions regarding the use of MODTRAN5.

I thank Tobias Fisher (University of New Mexico), Jacopo Taddeucci (Istituto Nazionale di Geofisica e Vulcanologia, Italy), Andrew Harris (Université Clermont Auvergne, Laboratoire Magmas et Volcans, France) and the anonymous reviewers for their comments on the papers we published.

Mahalo to Jay Fidell and all his team at ThinkTech Hawai'i TV for allowing me to be a guest and host for science TV programs.

Thank you also to the Golden Key International Honor Society and particularly to their Hawai‘i chapter for making me a member and for allowing me to join various community-oriented activities during the Academic Years.

A big and joy-filled thank you to my officemates and friends Estelle Bonny, Sarah Crites, Erin Fitch, Caroline Caplan, Melissa Adams, Myriam Lemelin, Hannah Moss-Davies, Tayro Acosta, Tanja Giebner, Katie Robinson, Macey Stanford, Lingzhi Sun, David Frank, and Elizabeth Fisher. Mahalo for the wonderful time we had in and out of the office.

A grand ‘me ka mahalo nui’ to Ku‘ulei Pila-Alesna, Liz Hennessey, Michelle Peng and all the staff of the Sheraton Princess Kaiulani for the many salmon-based breakfasts I had with them!

This experience would not have been the same without the loving and caring Ohana I made in Hawai‘i: Ajith Kumar Antony Daas, Pattie Borges and all her birds, dogs and cats, Vandana Narayan, Frances De Lima Kalīkolehuaopanewa, Ethel Alikpala Ward, Merlyn Labiste, His Royal Highness Ali‘i Sir Herbert Lau, Wendy Loh, Maki Gallagher, Benny Kosasih, Augustina Sri Muylati, Regina Jenkins and Katherine Miller.

Grazie and cheers to all of my Friends in Italy and the U.K.

And above all, I would like to express the most loving and joyful thank you I could possibly imagine to my Family: my dad Alessandro and my mom Adilia Maria for being with me even during the most difficult moments as well as Madame Mary and Her Son. They know why.

Funding for this work was provided by NASA’s Earth Science Technology Office (Instrument Incubator Program, NNX14AE61G). I thank the United States Department of Interior National Parks Service for authorizing collection of the field data reported in dissertation (Permit number HAVO-2015-SCI-0050).

ABSTRACT

Remote measurements of sulfur dioxide (SO_2) emission rate (mass flux), emitted by active volcanoes are important to predict volcanic behavior and for public health. However, an accurate method to carry out these measurements during both day and nighttime has not been established yet. Many volcanic gases of interest have distinctive spectral features in the long wave Thermal InfraRed (8-14 μm), which have potential to be detected by imaging interferometry. The aims of this dissertation project are threefold. Firstly, a newly developed Thermal Hyperspectral Imager (THI) was tested for SO_2 gas measurement capabilities. The system employs a Sagnac interferometer and an uncooled microbolometer in rapid scanning configuration to collect hyperspectral images. Each pixel in the resulting image yields a spectrum with 50 samples between 8 μm and 14 μm. It was found that imaging interferometry can detect SO_2 spectral features at high spatial, spectral and temporal resolution with high signal to noise. Secondly, the dissertation focused on how to convert measured SO_2 gas radiance into SO_2 path-concentrations, needed to derive flux information. It was found that existing techniques for SO_2 gas path-concentrations retrievals, which are based on comparing spectral radiance for portions of the image that correspond to the plume and for adjacent regions of the image that do not (i.e., "clear sky") to isolate the contribution that the plume makes to the measured radiance from the background, do not work if the plume is imaged against a cloudy background with strong heterogeneities. Therefore, a new method was developed. The new algorithm is based on Partial Least Squares Regression techniques to allow for single point SO_2 path-concentration retrievals. It provided good results under both clear and cloudy sky background conditions, but only under low atmospheric water vapor column amounts. Finally, temporal trends of SO_2 fluxes were evaluated during day and nighttime at the summit of Kīlauea volcano under both clear and cloudy sky conditions. The new camera and techniques described in this dissertation provide an effective tool for monitoring SO_2 fluxes remotely under a variety of background conditions (clear and cloudy sky, cold and hot backgrounds).

TABLE OF CONTENTS

LIST OF TABLES

LIST OF FIGURES

LIST OF ABBREVIATIONS AND VARIABLES

Abbreviation/Variable	Definition
A	amplitude
ALTA	Amenable Lookup Table Algorithm
BB	Black Body
BE	Background Emission
BT	Background Transmission
c	speed of light
CPVC	Chlorinated PolyVinyl Chloride
COSPEC	COrrelation SPECtrometer
D&P	Design & Prototype
DOAS	Differential Optical Absorption Spectroscopy
E	first residual matrix for the training of ALTA
EPA	EPAd
F	second residual matrix for the training of ALTA
$\mathcal{F}$	Fourier transform
$F(\nu)$	signal in the frequency domain
$f(t)$	signal in the time domain
FE	Foreground Emission
FLIR	Forward looking InfraRed
FT	Foreground Transmission
FTIR	Fourier Transform InfraRed
g	gravity acceleration
gcT	empty gas cell transmission
H	hydrostatic pressure
Hh	irradiance
HVO	Hawaiian Volcano Observatory
I	Intensity
IR	InfraRed
K	Concentration
L	spectral radiance

l	number of components for the training of ALTA
LUT	LookUp Table
M	mega
m	number of radiances for the training of ALTA
MCT	Mercury Cadmium Telluride detector
MODTRAN	MODerate resolution atmospheric TRANsmission
N	number of frames in a THI hyperspectral data cube
n	case number for the training of ALTA
NEdL	Noise Equivalent Spectral Radiance
NEdT	Noise Equivalent Temperature Difference
NIST	National Institute of Standards and Technology
NWS	National Weather Service
OPD	Optical Path Difference
p	number of SO_2 path-concentrations for the training of ALTA
PE	Plume Emission
PLSR	Partial Least Squares Regression
ppm	parts per million
ppm-m	parts per million meters
ppm-v	parts per million by volume
P	first orthogonal matrix for the training of ALTA
PT	Plume Transmission
Q	second orthogonal matrix for the training of ALTA
r	radius
RSAM	Real-time Seismic Amplitude Measurement
SNR	Signal to Noise Ratio
T	third orthogonal matrix for the training of ALTA
TIR	Thermal InfraRed
THI	Thermal Hyperspectral Imager
U	fourth orthogonal matrix for the training of ALTA
u	velocity
USGS	United States Geological Survey
UV	ultraviolet

V	volume
W	partial pressure
wt%	weight percent
X	input matrix of simulated spectra for the training of ALTA
XX	input matrix of measured spectra, while using ALTA
Y	output matrix of SO_2 path-concentrations for the training of ALTA
XX	output matrix of measured spectra, while using ALTA
γ	fugacity coefficient
δ	space
ε	absorption coefficient
η	viscosity
θ	concentration ratio
μ	micron
ν	frequency
ξ	force
τ	maximum amount of water that can be dissolved in a melt
Φ	fugacity
ω	path-length

CHAPTER 1

INTRODUCTION

According to geologist Leopoldo Pilla, "*i vulcani sono la piu' grande scuola di Fisica del globo*" (volcanoes are the greatest school of physics in the whole world) (Mercalli, 1907) because a volcanic system includes all the endogenic natural phenomena that occur on the Earth. Besides being fascinating examples of the power of nature, 1500 sub-aerial volcanoes caused extensive distruption during the Holocene period (Francis and Oppenheimer, 2004) and many of them claimed hundreds of thousands of lives (Sthoners 1984). The main objective of volcanology is successfully predicting volcanic eruptions in the hope of preventing deaths from future natural disasters.

The physical and geological processes that lead to a sub-aerial volcanic eruption such as mantle dynamics, melt buoyancy and migration, volatiles exsolution, ground shacking, degassing and eventually magma fragmentation have all been identified and many pieces of research have been and are being carried out (e.g., Turcotte 1982; Asimow 2000; Francis et al. 2000; Fisher 2007; Edmonds 2008; Shinohara 2008; Castro et al. 2014). Moreover, extensive networks that combine seismological, geodetic and remote sensing techniques were established to monitor volcanoes that are situated in highly populated areas throughout the world such as the Somma-Vesuvius volcanic complex in the Napoli bay area, Italy and the composite Sakurajima volcano, Japan (Scandone and Giacomelli 2004). For these reasons, volcanologists have achieved a good level of understanding of how magma moves in a volcanic plumbing system and are now able to anticipate the behaviour of a volcano up to few weeks in advance by looking at well-established patterns of pre-eruption unrest (Roman and Gardine 2013). However, long term and months in advance predictions are still extremely complicated, but in this regard new technologies and particularly remote sensing of volcanic gases can make a difference in forecasting volcanic eruptions and providing early warnings for the population who lives in high volcanic hazard areas.

Magma contains many dissolved chemical species under the high pressure of the upper mantle or lower crust. However, as magma rises in volcanic conduits and the pressure it is subjected to decreases, these volatile species begin to exsolve from the silicate melt liquid and form bubbles that are responsible for driving explosive volcanic eruptions (Parfitt and Wilson, 2008). The detection of anomalous concentrations of such chemical components allows volcanologists to estimate whether magma is rising towards the surface and the volcano is about to erupt: volcanic gases are therefore like "*telegrams from the Earth's interior*" (Oppenheimer et al., 1998). However, volcanic volatiles do not behave all in the same way. In fact, certain species, like carbon dioxide (CO_2), are more insoluble than others in magmas and begin to exsolve at greater depths. Nevertheless, the large concentration of CO_2 in the atmosphere (Table 1.1) makes difficult or impossible to distinguish the volatiles exsolved by volcanoes from those that are already present in the atmosphere. For this reason, anomalous field detection of the not so common in the atmosphere sulfur dioxide (Table 1.1) gas has always been considered the undeniable proof that new magma has been injected in a volcano's plumbing system. However, sulfur dioxide (SO_2) is very soluble in magma and as a result, it exsolves when magma is very close to the surface and the volcano may be about to erupt. This is the reason why other more insoluble gases, such as carbon dioxide, which may begin to exsolve even many months before an eruption (Giggenbach, 1983), should be taken into account in order to guarantee earlier warnings and plenty of time for the people that has to move out of the hazardous zones. Fluxes of other volcanic gases are typically found by combining SO_2 flux data with mass ratios (i.e., X/ SO_2) (e.g., Gerlach et al., 1998; Wardell et al., 2001).

Therefore, volcanic degassing provides information on magma flow within a volcanic system (e.g., Aiuppa et al. 2007; Anderson and Segall 2013), eruption rates (Allard et al. 1994), and, hence, mass balance (e.g., Allard et al. 2014). Additionally, detecting volcanic emissions of SO_2, and related acidic sulfate aerosols, is important for public health (EPA 2011). SO_2 reacts chemically with sunlight, dust

particles, oxygen and water to form sulfate aerosols, which can lead to public health issues as well as damages to livestock, cultivations, and infrastructures (e.g., Baxter 1999; Schmidt 2014; Zuccaro et al. 2014). These are additional reasons why it is important to measure gaseous emissions from volcanic plumes.

Table 1.1. Average tropospheric and volcanic concentrations of the three main volcanic volatiles expressed in parts per million (ppm). Sulfur dioxide is the least abundant in the troposphere (Symonds et al., 1994; ESRL-NOAA, 2014)

Volatile species	Tropospheric concentration	Volcanic plume concentration
Water (H_2O)	40 – 40.000 ppm	40 – 40.000 ppm
Carbon dioxide (CO_2)	400 ppm	410 ppm
Sulfur dioxide (SO_2)	0.001 ppm	2 ppm

1.1. The origin of volcanic volatiles

The origin of dissolved volatiles in the mantle dates back to the formation of the Solar System 4.5 billion years ago (e.g., McKenzie and Nimmo 1999) when gravity began to assemble it after an earlier supernova created a planetary nebula of cosmic dust (e.g., Gritschneder et al. 2011). In fact, the gravitational instability of countless and Brownian moving lithic debris called planetesimals (Kenyon and Bromley 2006) and pieces of frozen gas that formed the cosmic dust led to innumerable collisions during the first hundred million years after the birth of the Sun (Montmerle et al. 2006). These crashes enabled the planetesimals to grow by gravitational accretion (Wetherill 1980). As this process continued and many new cosmic dust materials were added to the growing planetesimals, the masses of these objects became sufficiently large that their gravitational energy began to be turned into heat (Montmerle et al. 2006). At this stage, the extremely high pressure of the inner parts of the planetesimals, which are now renamed protoplanets, enabled certain chemicals – including those that will eventually form the current volcanic volatiles (Wallace and Anderson 2000) – to be dissolved in the melt liquid of the silicate-dominated bodies of the forming Solar System (Halliday 2013). Finally, during the so called "telluric era", these objects became shaped and underwent melting processes that enabled a density separation of their melt region into layers of decreasing density called: core, mantle and crust and became the silicate-dominated planets (Lissauer 1993; Montmerle et al. 2006).

On the Earth, the largest of the terrestrial planets, the mantle is the 2850 km thick layer that surrounds the metallic core and is predominantly composed of crystalline silicate rocks (Jeanloz 2000). In fact, only small percentages of the outermost mantle are melt and these areas are primarily the magmatic and volatile sources of the mid-oceanic ridge and intra plate volcanism (Jeanloz, 2000; Parfitt and Wilson 2008). Nonetheless, these regions of the mantle also represent the magmatic and volatile sources of arc volcanism. In fact, the non-arc volcanism's products, the oceanic lithospheric crust and water, are pushed into the mantle, melt again and recycled in the subduction zones (Wallace 2005).

A variety of chemical volatiles can be dissolved in such silicate melts. Thanks to melt inclusion in phenocrysts and quenched submarine basaltic glass analysis, it was determined that if a 3 to 8 km deep basaltic volcanic magma chamber is considered, the magma stored in it is expected to have 0.5 weight percentage (wt%) of water (H_2O) and less than 1 wt% of carbon dioxide (CO_2) dissolved in it (e.g., Greenland 1987; Wallace and Anderson 2000; Shinohara 2008). H_2O and CO_2 are by far the most abundant volatiles of all (Parfitt and Wilson 2008). In fact, volcanoes are the main pathway for H_2O and CO_2 to escape from inside the Earth to the surface and for this reason they have played a key role in the creation of the Earth's atmosphere and Oceans (Wallace and Anderson 2000; Genda et al. 2013). In fact, recent melt inclusion and high temperature volcanic gas-phased water studies have confirmed that the chemical solution of water and water-enriched minerals, like gypsum $CaSO_4 \cdot 2H_2O$ and calcium hydroxide $Ca(OH)_2$, which is pumped into the zones of subduction, equals the flux of non-meteoric water that is exsolved from subduction zone volcanoes (Fisher 2008).

The third most abundant volcanic volatile is sulfur, which is responsible for generating gas emissions of sulfur dioxide (SO_2), sulfuric acid (H_2SO_4) and the often noticed rotten-egg smell, which is caused by releases of hydrogen sulfide (H_2S) (Symonds et al. 1994). Sulfur is also the source of the famous sulfuric yellow crystals that are deposited near volcanic vents and fumaroles. Additionally, many other chemical species can be found in magmas, including the halogens that form hydrogen chloride (HCl) and hydrogen fluoride (HF), and minor amounts of noble gases like helium (He) and argon (Ar) (Symonds et al. 1994; Wallace and Anderson 2000; Parfitt and Wilson 2008). It was observed that the concentration of the different volatiles in magma is strictly dependent on the magma composition itself: Table 1.2. shows the averaged concentrations in different types of magmas.

Table 1.2. Concentrations of various volcanic volatiles in different melts. References: ** Wallace 2005 (Melt inclusions); * Shinohara 2008; * Giggenbach 1996**

Volatile species	Concentration in basalt	Concentration in andesite	Concentration in rhyolite
H_2O	10000−80000 ppm *		
CO_2	10000 ppm *		
S	910−3000 ppm**		
Cl	530−2240 ppm**		
F	100-300 ppm**	300-600 ppm***	400-600 ppm***

The pressure, the chemical composition and the temperature of magmas are the key factors that control how soluble a volatile is (Parfitt and Wilson 2008) and more specifically, these processes are ruled by a series of empirical physical laws called solubility laws. A variety of experiments on melts have been carried out since Hamilton et al. (1964) performed the first ones that provided data regarding the solubility of H_2O in magma. In these experiments, samples from various volcanoes with different silica content were brought back to their specific magma chamber conditions in controlled environments and melted. During this process, external H_2O was added to the sample and allowed to dissolve into it until it was possible i.e. the sample did not reach the saturation point (Moore et al., 1998). The maximum amount of water τ given as a weight percentage (wt%) that can be dissolved in basalt $\tau_{water\ \text{in basalt}}$ and rhyolite $\tau_{water\ in\ rhyolite}$ are displayed in function of the partial pressure W_w of the water.

$$\tau_{water\ in\ basalt} = 0.1078\ {W_w}^{0.7} \tag{1.1}$$

$$\tau_{water\ in\ rhyolite} = 0.4111\ {W_w}^{0.5} \tag{1.2}$$

The solubility of CO_2 does not depend as strictly as the one of the water on the chemical composition of magma and as long as the pressure does not exceed 300 MPa (Wallace and Anderson 2000), its solubility for most types of magma is described by the following equation:

$$\tau_{carbon\ dioxide} = 0.0023\ W_c \tag{1.3},$$

where $\tau_{carbon\ dioxide}$ is the amount of carbon dioxide that can be dissolved in magma expressed as a weight percentage (wt%) and W_c is the partial pressure of the CO_2 (Parfitt and Wilson 2008).

The graph in Figure 1.1 emphasizes that these solubility relationships for H_2O are strongly nonlinear. In fact, the solubility function of H_2O is approximately a square root function of the H_2O partial pressure (Shinohara 2008). Conversely, the solubility of CO_2 is a linear function of the CO_2 partial pressure. Furthermore, they also imply how less soluble than water carbon dioxide is. In fact, the quantity of CO_2 that can be dissolved in both rhyolite and basalt is 100 times less than those of water at the same thermodynamic conditions (Wallace and Anderson 2000). CO_2 is the most insoluble of all the volatiles (not considering noble gases). In this regards, Giggenbach 1996 inferred that CO_2 begins to exsolve at a depth of about 80 km and its exsolution rate peaks at a depth that ranges between 30 and 10 km

(Wallace and Anderson 2000; Wallace 2005; Shinohara 2008). On the other hand, H_2O turns into its gas phase at much shallower depth (2-6 Km) (Wallace and Anderson 2000). Figure 1.2 shows a cartoon that illustrates how the exolution rate of various volcanic volatiles is linked with depth. This means that when magma rises in a volcanic conduit, the initial gas phase composition is CO_2-dominated, whereas when it reaches shallower depth (i.e. when H_2O begins to exsolve) it becomes more H_2O-rich (Holloway 1976). This is the reason why H_2O is considered the most important volatile in driving volcanic eruptions (Fisher 2008).

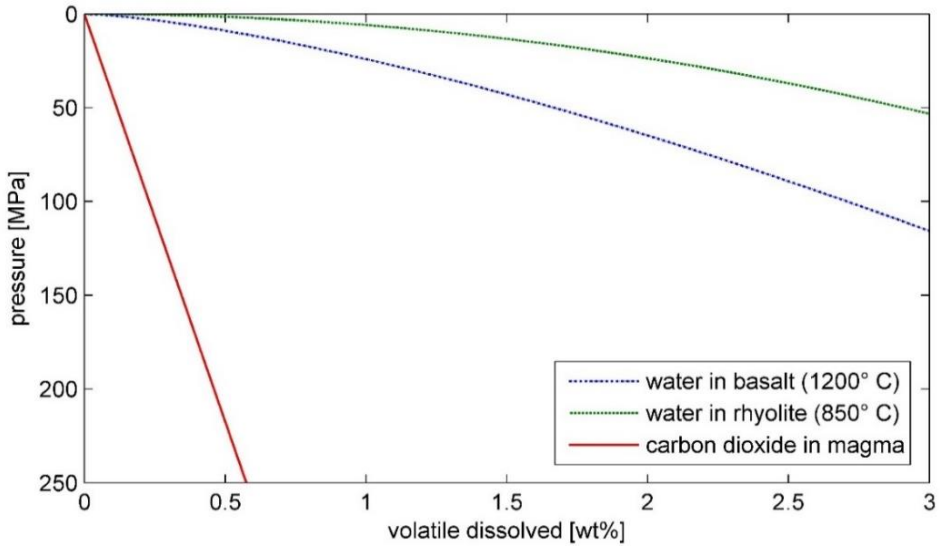

Figure 1.1. Solubility curves of H_2O and CO_2. The graph shows the experimental determination of the amount of volatiles (water and carbon dioxide) given as weight percentage (wt%) that can be dissolved in various types of magmas (basalt and rhyolite) at different pressures expressed in Mega Pascal. The solubility of CO_2 is lower than that of H_2O.

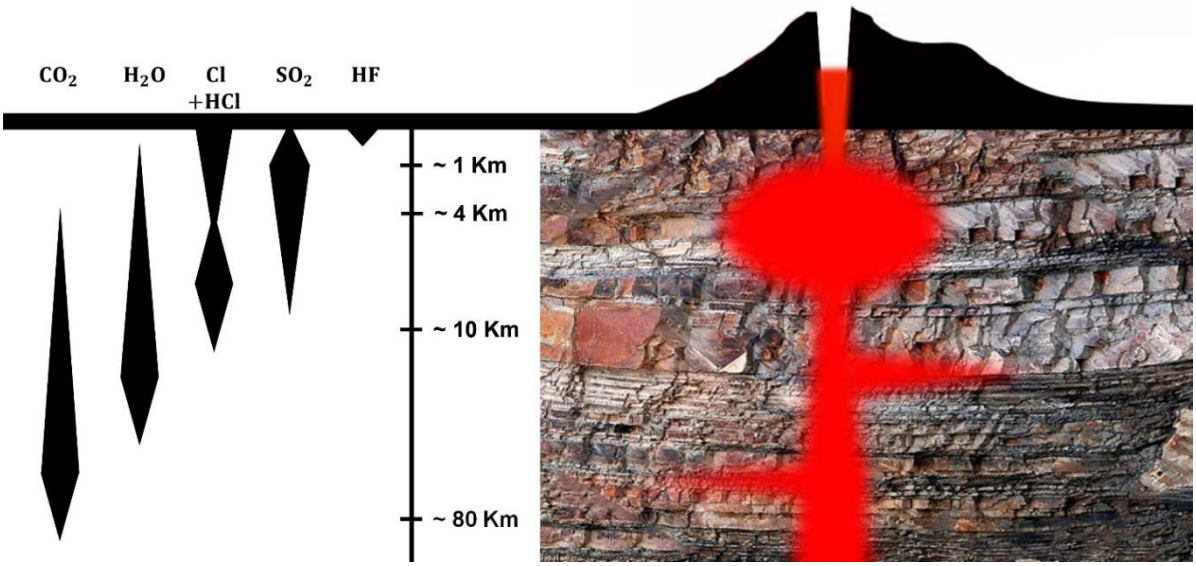

Figure 1.2. Schematic diagram of the approximate depths of volatile exolution at a basaltic volcano. The wider the band, the higher is the rate of exolution. It can be seen that CO2 begins to exsolve at a depth of about 80 km and its exolution rate peaks at a depth that ranges between 30 and 10 km.

From a theoretical point of view, Equations (1-3) are only valid if one species of volatile was present in the magma. In fact, they were determined by equilibrating the melt with a single gas component (Wallace and Anderson 2000). However, the picture is much more complicated if two or more volatiles are present in the melt because they may start interacting with one another and with the magma itself: when the most soluble one begins to exsolve, small amounts of the others may actually begin to diffuse into the newly formed bubbles even if they have not reached their exsolution point yet (Parfitt and Wilson 2008). Nonetheless, considering the solubility of two species of volatiles dissolved in the same magma as if they were independent is generally acceptable and the description provided by the solubility laws for H_2O and CO_2 is considered accurate enough (Parfitt and Wilson 2008), providing that the melt does not reach its volatile vapour-saturated condition (Wallace and Anderson 2000).

In fact, when this happens, the solubility of single volatiles is strongly influenced by the presence of other gas-phased volatiles and more advanced thermochemical models that deal also with the speciation of both water and carbon dioxide have to be considered (Wallace and Anderson, Jr., 2000). In fact, recent spectroscopy studies on melts have determined that liquid-phased water and carbon dioxide occur in different species in melts (Wallace and Anderson 2000; Schmincke 2004). H_2O is present both as hydroxyl ion OH^- and as molecular H_2O both in basalt and high-silica melts (Grezechnik and McMillan 1998), whereas the speciation of CO_2 is largely dependent on the silicate melt composition: in silica-poor magmas it is present as a bound carbonate (CO_3^{2-}) and in granitic magmas simply as CO_2 molecules (Duncan and Dasgupta 2013).

The behaviour of liquid-phased sulfur in the silicate melt of the magma is more complicated because this volatile is present in different oxidation states, more commonly sulphides S^{2-} and sulphates $(SO_4)^{2-}$ (Jugo et al. 2005), but also as an immiscible Fe-S-O liquid (Larocque et al. 2000; Shinohara 2008), depending on the magmatic oxygen fugacity [1](Wallace and Anderson 2000). At low oxygen fugacity, sulfur occurs as a sulfide, conversely, at high oxygen fugacity, it is mostly present as a sulfate (Jugo et al. 2005). For this reason, the solubility of sulfur dioxide (SO_2) cannot simply be expressed as a function of the partial pressure of SO_2 like H_2O and CO_2 (Shinohara 2008), but has to be represented as the ratio θ of its gas $K_s{}^{gas}$ and liquid-phased $K_s{}^{melt}$ concentrations (Keppler 1999), both given as wt%.

$$\theta = \frac{K_s{}^{gas}}{K_s{}^{melt}} \tag{1.4}$$

The maximum amount of sulfur that can be dissolved in the silicate melt liquid is not only controlled by the pressure and the composition of the magma, but also by the saturation of the melt with an S-bearing phase. At relatively low oxygen fugacity, this phase can be either an iron-rich sulphide liquid in basaltic melts, or pyrrhotite or a Cu-Fe sulphide in andesitic and ryholitic melts, whereas at relatively high oxygen fugacity, this process is controlled by the sulphate mineral anhydrite ($CaSO_4$) that crystalizes in a variety of melt compositions (Wallace and Anderson 2000). The solubility of SO_2 increases with the Fe concentration in the melt (Wallace and Carmichael 1992) and is larger than those of the other volatiles. Consequentially, it begins to exsolve later than the others i.e. when the magma is just a few kilometres from the surface (Sparks 2003).

The depths at which CO_2 and particularly H_2O exsolve can strongly influence the behaviour of the volcanic system as a whole. In fact by the time the magma is close to the surface and H_2O begins to exsolve from the silicate melt liquid, the majority of the CO_2 has already left the system because of its low solubility (Gerlach, T.M. 1986; Allard et al. 1991; Hards 2005; Fisher 2008). Measurements at Etna volcano support this hypothesis. In fact, the volcano has a very deep magma chamber and releases most

[1] The oxygen fugacity is a measure of the tendency of the liquid-phased oxygen to vaporize from the melt. It is useful to remember that the fugacity Φ_i is defined as the partial pressure P_i of the i-th non-ideal chemical gas component i dissolved in a mixture that satisfies the equation of the ideal gases. Therefore:

$$\Phi_i = \gamma_i P_i \,,$$

where γ_i is the fugacity coefficient of the i-th gas component of the mixture, which is equal to 1 for an ideal gas.

of its CO_2, which accounts for 40% of the world's volcanic carbon dioxide, during dormancy i.e. when magma is stored deep in its magma chamber and the only volatile that can exsolve is CO_2 itself (Gerlach 1991). Conversely, Mount Etna releases mostly H_2O during its eruptive phases (Gerlach 1991). Similar behaviour is observed at Kīlauea volcano, where carbon dioxide is mainly degassed in the caldera i.e. from the magma chamber, rather than the its rift zones, where SO_2-dominated emissions, which represent fractionation during crustal storage, prevail (Gerlach 1986; Symonds et al. 1994). This particular two stage degassing process is typical of the majority of hot spot and divergent plate volcanoes (Gerlach and Graeber 1985).

In order to generalize these shallow magma degassing processes, geoscientists distinguish between those that occur at non-arc and arc volcanoes (Symonds et al. 1994). In fact, the actual physical degassing phenomena and the composition of the exsolved volatiles are very different from hot spot and divergent plate volcanoes, such as Kīlauea located on the Big Island of Hawai'i and Erta Ale set along the African Rift Zone on the Ethiopian Highlands, and convergent plate volcanoes such as the White Island Volcanic Complex in New Zealand (Symonds et al. 1994). As previously discussed, non-arc volcanism degassing occurs predominantly as a two stage process. However, some exceptions have also been studied. In fact, the venting at the Antartic alkaline intra-plate Mount Erebus volcano occurs as a single stage process and its degassing consists mainly of water and carbon dioxide-enriched emissions from its sustained summit lava lake (Wardell et al. 2004). At arc volcanoes, degassing processes are more difficult to study not only because of their related hazards, but also because each arc has its own geochemical and geophysical features (Fisher, 2008). Furthermore, felsic petrogenesis implies that only the latest stages of melt evolution can be recorded in melt inclusions (Edmonds 2008). However, there are several examples of long-term gas monitoring at these kind of trench volcanoes such as those at Mount Saint Helens, United States, Showa-Shinzan dacitic dome, Japan and White Island volcano, New Zealand. All the studies that have been carried out suggested that rising magma in a dormant volcano may be initially accompanied by releases of C and O-dominated gases and later by S. Then, during a volcanic eruption, the magma is ejected and fragmented mainly due to water and finally, after the volcanic eruption, the H content of the gases increases linearly, whereas the concentrations of C, O and S decrease linearly with time. This has been interpreted with the fact that after an explosive eruption there is a steady reduction of the magmatic component of the gases and an increase of the hydrothermal component (Symonds et al. 1994), such as at Taupo hot springs in New Zealand (Mia et al. 2012).

In order to study how volcanic volatiles are actually able to drive an explosive eruption, it is important to understand how bubble formation and degassing occur at various volcanoes from a physical point of view. The remarkable journey of the volatiles that brings them from the Earth's interior to the atmosphere, begins in a volcanic magma chamber where the pressure exceeds atmospheric levels by 3 000 times (Jaupart 2000). At this stage, the magma is usually undersaturated in volatiles, but as long as it rises towards the surface, it reaches a volatile saturation point determined by solubility laws. In fact, if any kind of magma with a certain quantity of volatiles dissolved in it begins to rise and the pressure it is subjected to starts to decrease, nothing really happens until the solubility curve of that particular species of volatile is reached and intersected. At this point, the quantity of dissolved volatile that is present in the magma is exactly the same as the maximum amount of gas that can actually be dissolved in such type of magma. This is the point at which the magma becomes saturated in gas. As the magma continues to rise towards the surface, it turns into a super-saturated mixture and consequentially, the volatiles are no longer able to stay in solution and begin to exsolve and form gas bubbles (Jaupart 2000).

The process of bubble formation or vesiculation is not a simple process. From a theoretical point of view, bubbles should nucleate when the magma becomes saturated in a certain species of volatile, but practically this does not happen. In fact, at the beginning the strong magmatic surface tension tries to shrink the newly formed bubbles and push them back into the silicate melt liquid. However, this process cannot last for long: when molecules of a same exsolved volatile begin to gather and aggregate, they are able to counterbalance the surface tension forces and form a gas bubble (Lyakhovsky et al. 1996). This spontaneous process of aggregation is called homogenous nucleation. Moreover, there is

another way molecules can minimize the effects of the magmatic surface tension and form bubbles: by gathering onto irregular lithic or crystal surfaces that may be present in a volcanic magma chamber (Jaupart 2000). The scientific literature refers to this second type of nucleation as heterogeneous nucleation (Parfitt and Wilson 2008).

After the volatile bubbles have been formed, there are three main physical processes that enable them to grow: diffusion, decompression and coalescence. Growth by diffusion occurs when a bubble of a certain species of gas is joined by molecules that can be either of the same volatile or even of others less soluble volatiles. This process is controlled by various aspects such as the species of volatiles, the temperature and chemical composition of the melt (Parfitt and Wilson 2008). Secondly, growth by decompression occurs as the bubble rises and the pressure[2] they are subjected to decreases in accordance to the Boyle's gas law, which states that the product HV of the pressure H in the gas and the volume V occupied by the gas is always constant. Finally, growth by coalescence happens when a large and fast bubble overtakes a smaller one and together they form a single bigger bubble (Parfitt and Wilson 2008).

In order to explain how coalescence enable bubbles to grow, it is important to consider the fact that gas bubbles are always buoyant compared with the magma they are dissolved in. Therefore, they will always tend to rise faster than the magma itself. However, the bubble's natural buoyancy force is always opposed by the drag force. If a single gas bubble is considered and assuming that it does not rise too quickly and remains spherically shaped, the buoyancy force ξ_b that acts on it can be defined as:

$$\xi_b = \frac{4}{3}\pi r^3(\rho_m - \rho_g)g \tag{1.5}$$

where ρ_m and ρ_g are respectively the density of the magma and of the gas. Equation 1.5 is known as the Jeffrey's equation. Furthermore, hypothesizing that the radius of the bubble remains small enough so that its size can be controlled by both the viscosity of the magma η and the velocity of the bubble u, the drag force ξ_d that acts on the bubble can be expressed by the following equation:

$$\xi_d = 6\pi\eta r u \tag{1.6}$$

At the equilibrium, the condition $\xi_d = \xi_b$ is fulfilled. Therefore:

$$6\pi\eta r u = \frac{4}{3}\pi r^3(\rho_m - \rho_g)g \tag{1.7}$$

If the Equation 1.7 is rearranged and expressed in terms of velocity u of the bubble, it becomes:

$$u = \frac{2\pi(\rho_m - \rho_g)g}{9\pi\eta} r^2 \tag{1.8}$$

This result stresses that the velocity of the bubble is directly proportional to the square of its radius ($u \propto r^2$). In other words: the larger the radius of the bubble, the higher its velocity. This means that larger bubbles rise much faster than smaller ones and it is exactly this discrepancy in speed between the various bubbles than enables coalescence processes. In fact, the higher speed of the larger bubbles allows them to overtake the smaller and slower ones.

Bubble coalescence is a predominant process in mafic low silica-content magmas such as basalt and particularly it is responsible for fuelling Strombolian activity in which a single bubble overtakes all the others, becomes as large as the volcanic conduit itself and causes the magma to be erupted in vigorous explosions (Parfitt and Wilson 2008; Allard 2010). However, it plays an important role even in allowing gases to leave felsic high silica-content magmas such as granite. In this case, bubbles are usually no longer able to easily grow in the melt and rise towards the surface and consequentially, powerful

[2] The pressure the volatiles are subjected to is an hydrostatic pressure H_h that can be expressed in terms of density ρ, depth h and gravity g thanks to the following equation: $H_h = \rho g h$.

explosions, such as those that struck the Puyehue-Cordón Caulle volcano, Chile in 2011, may be generated. However, passive coalescence driven degassing is possible also at rhyolitic volcanoes and recent studies on high-silica melts suggested that gases can escape from such sticky and viscous rhyolitic lavas by creating pathways of transient channels of interconnected bubbles (Berlo et al. 2013).

Therefore, the vesiculation of bubbles rates become larger as the pressure decreases and the magma tends to lose its volatile content. This loss of volatiles is accompanied by rapid release and expansion of gas that can induce the magma to break apart, that means to change it from being poured out as a continuous body of molten rock containing gas bubbles to being erupted as a continuous gas in which lithic clasts are carried along in an explosive way (Wilson and Head 1981). This mechanism is responsible for causing practically all types of activity, including Hawaiian lava fountains, Strombolian and Vulcanian explosions and also Plinian eruptions, depending on the amount of gas that remains trapped in the silicate melt. This depends in turn on the viscosity of the magma itself: in felsic melts, the venting of the gas may be considerably slowed down by the stickiness of the magma and this may result in gases being trapped in the melt and eventually in powerful explosions (Mader 1998). Moreover, it was proved that the exsolution of volatiles in basaltic magmas results in an increasing of the liquidus temperature of the melt and therefore, in an undercooling of the magma itself (Hort 1997). For this reason, it was inferred that this phenomenon can trigger the formation of small sized-crystals, called nanolites, which are responsible for increasing dramatically the viscosity of the melt, which in turn may induce basaltic volcanoes to erupt very violently. It is exactly this degassing driven undercooling and crystallization that is thought to be the actual physical mechanism that triggered one of the most recent and powerful Plinian eruptions that struck the basaltic volcano Mount Etna, Italy in the 122 BC (Houghton et al. 2004).

1.2. The importance of studying volcanic volatiles.

1.2.1. Volcanic degassing drives eruptions and can help forecasting volcanic activity

Surveying the chemical composition and the amount of high temperature gases released from a volcano, coupled with seismological and ground deformation measurements, allows geoscientists to determine whether new magma is being injected in the plumbing system of a volcano and potentially, estimate whether an eruption is about to occur (Galle et al. 2010).

Volatiles dissolved in the Earth's silicate melt liquid play a fundamental role in driving explosive eruptions. If magma had no volatiles dissolved in it, it would be discharged at the surface simply as basaltic lava flows or as growing lava domes, depending on its chemical composition and effusion rate. However, on the Earth and on the other silicate-dominated bodies of the Solar System gasless magmas do not practically exist and volcanic eruptions always involve some extent of explosiveness (Parfitt and Wilson 2008). This means that the material that is being erupted is fragmented and ejected in a stream of gas. Therefore, the presence of different species of chemical volatiles is ultimately responsible for both a 400 meters high Hawaiian lava fountain, in which clots of basalt up to one meter and more in diameter are steadily erupted from a vent (Head and Wilson 1987), and a Plinian eruption, in which tiny particles of tephra are blasted out the vent and carried up to heights of thousands of meters into the air (Wilson and Walker 1987). Therefore, it is this stream of bubbles of exsolved volatiles that causes the lava being erupted by a volcano to break apart into pieces of materials that have a large variability in size.

This physical phenomenon is somehow similar to what happens when a bottle of Spumante or any other sparkling drinks containing dissolved carbon dioxide (CO_2) is opened. Suddenly, the pressure within the bottle decreases to atmospheric and the solubility of the CO_2 becomes lower. This induces part of the liquid phased CO_2 to exsolve and form gas bubbles that increase their size as long as they rise in the liquid and enable the drink to "fizz". So, as the pressure of a closed bottle of wine is able to keep the phase of the CO_2 liquid, in the same way the high pressure in a magma chamber that is generated by the weight of the overlying rocks suppresses the vesiculation processes in the deep magma and keep the

phase of the volatiles liquid (Jaupart 2000). However, when the magma rises in the plumbing system of any volcano, the pressure begins to decrease and the volatiles are no longer able to be dissolved in the silicate melt liquid and begin to exsolve and form gas bubbles, eventually causing degassing that accompanies many types of volcanic phenomena (Shinohara 2008) and often anticipate a volcanic eruption (Symonds et al. 1994).

1.2.2. Volcanic degassing impacts the Earth's atmosphere and creates environmental issues for people, living creatures, and infrastructures.

Another reason why volcanic gases studies are relevant is determining how strongly they can affect the atmosphere of the Earth and people's life. CO_2 is a powerful greenhouse and toxic gas, but it rarely poses a direct threat to human life because it is usually diluted quickly enough in the air that its concentration does not reach lethal levels. Nonetheless, being denser than the air, if this colourless gas gathers in fractures or other deep features and reaches high concentrations, it can be lethal to people and animals. The most famous episode of people gassed and killed by carbon dioxide occurred on the evening of August the 21st, 1986 in the West African country of Cameroon when the volcanic Lake Nyos emitted a dense cloud of carbon dioxide that flowed across the area and inundated a nearby valley that channelled the gas into the farmers' villages of Nyos and Kam killing almost 1.250 people (Freeth 1992).

SO_2 reacts chemically with sunlight, dust particles, oxygen and water to form sulfate aerosols, which can threaten public health, be harmful to animals and plants, and damaging to infrastructures (e.g., Baxter 1999; Schmidt 2014; Zuccaro et al. 2014). The effects of SO_2 and other sulphate aerosols do also have strong effects on people, causing pollution, respiratory problems and skin irritation. Sulfur dioxide emissions are particularly monitored in a careful way on the leeward side of the Big Island of Hawai'i, which is often subjected to volcanic smog or "vog". The North and South Kona districts are particularly impacted by the vog throughout the year because of the Kona coast's unique wind and rain patterns. The west facing slopes of the giant Mauna Loa and Hualālai volcanoes are in a trade winds-shadow area. However, the North-Eastern Pacific trade winds are able to reach even these locations as the mass of Mauna Loa makes them curve back and flow around its southern slopes. This, coupled with the land-ocean afternoon breezes that develop daily along the Kona coast, enables the vog to accumulate and stagnate almost persistently on the leeward side of the island causing potential health problems and acid rains (Giambelluca et al. 2013). Moreover, SO_2, H_2S and H_2SO_4 aerosols can also impact the environment in a very serious way (Wallace 2001). In fact, it was observed that high sulphate concentrations (particularly those of anhydrite) in the erupted magmas can impact the weather on a global scale both after explosive and effusive eruptions (Sigurdsson, 1982). In fact, the Pinatubo's climatic eruption, which struck the island of Luzon in the Philippine Islands in 1991, and the 1783 eruption of the Lakagígar crater-row in Iceland injected respectively $2\ 10^6$ tons and $6.3\ 10^7$ tons of SO_2 into the atmosphere (Self et al., 1999; Sigurdsson, 1982). As a result, the first one triggered a 0.6 °C cooling of the Earth's surface in the Northern Hemisphere (Rampino and Ambrose 2000; Jugo et al. 2005) and the second one was responsible for causing one of the most important and socially repercussive events of the last thousand years (Sigurdsson, 1982). However, recent studies have pointed out that not only sulphates, but also sulphides can be responsible for volcanic global cooling like after the most powerful 1835 eruption at Cosigüina volcano, Nicaragua (Longpré et al. 2014).

1.3. Monitoring volcanic volatiles

Detecting volcanic emissions of SO_2, and related acidic sulfate aerosols, is important for volcanic eruption prediction and public health (EPA 2011). In fact, volcanic degassing provides information on magma flow within a volcanic system (e.g., Aiuppa et al. 2007; Anderson and Segall 2013; Gabrieli et al. 2015), eruption rates (Allard et al. 1994), and, hence, mass balance (e.g., Allard et al. 2014). Additionally, SO_2 and its related sulfate aerosols are particularly harmful to public health, animals, plants, and infrastructure. For these reasons, it is important to measure SO_2 gaseous emissions from volcanic plumes.

1.3.1. The first studies

Volcanic gases have been documented and studied since the very first observations of volcanic activity in Southern Italy performed by Greeks and later even Romans. In fact, the Greek and later Roman historian Plutarch stressed the dangers of these gases by describing how important toxic gases from the Earth's interior were in driving the ecstatic inspiration of the Pythia priestess at the Oracle of Delphi (Spiller et al. 2000; De Boer et al. 2001) and the philosopher Seneca indicated gases as the main factor that drives volcanic eruptions (Mercalli 1907). However, investigations of active volcanoes from a truly scientific point of view started only in the XVII century. According to the great Italian volcanologist and Roman Catholic priest Giuseppe Mercalli, modern volcanology began with the eruptions of Vesuvius and Monti Rossi at Etna volcano respectively in 1631 and 1669. These eruptions were extremely important because they resulted in the very first modern scientific publications in volcanology as more than 200 papers dealing with the distinction between central and lateral eruptions, earthquakes as precursors of volcanic eruptions and volcanic gases as the main driving force for eruptions were brought out for the first time (Mercalli 1907).

Nowadays, volcanic gases are considered extremely important in volcanology because it is known that they may help in forecasting eruptions. Secondly, they were responsible for the creation of the Earth's atmosphere and still play a crucial role in controlling its physical dynamics. Moreover, as it was already highlighted by the Ancients, their toxicity can pose a hazard to people who live downwind or near active vents and fumaroles.

1.3.2. Direct sampling techniques

In order to effectively study volcanic emissions, a variety of techniques where developed since the Cornish chemist Humphry Davy collected volcanic gases for the first time using wine bottles on the Ferdinandea island, Italy in 1831 (Francis et al. 2000). The most common method for studying volcanic gases is direct sampling. However, carrying out this method requires lots of attention due to the hazards related to it. In fact, the collection of high temperature volcanic gases can be dangerous not only because of the toxicity of the gases, but also because of possible and sudden eruptions (Symonds et al. 1994). One of the latest fatal accidents related to gas sampling occurred when Galeras volcano in Colombia suddenly exploded in 1993 killing six volcanologists and three tourists who were taking gravimetric and gas measurements on the active summit cone within the caldera rim of the volcano (Baxter and Gresham, 1997). Direct sampling is possible thanks to a solution-filled sampling bottle technique, which was developed by Giggenbach in 1975 and later improved by Giggenbach and Goguel in 1989. The volcanic gases are collected with a setup that consists of a titanium or silica tube inserted directly into the volatiles source and attached to a condensation minimizer silica tube that in turn is connected to an evacuated pre-weighed collection flask, which has to be partly filled with a chemical solution of 4N NaOH. During the sampling, water condenses and the other volcanic gases are absorbed by the solution in accordance to a series of well-known chemical equations.

$$CO_2 + 2\ OH^-(aq) \rightarrow CO_3^{2-}(aq) + H_2O \quad (1.9)$$

$$4\ SO_2 + 7\ OH^-(aq) \rightarrow 3\ SO_4^{2-}(aq) + HS^-(aq) + 3H_2O \quad (1.10)$$

$$H_2S + OH^-(aq) \rightarrow HS^-(aq) + H_2O \quad (1.11)$$

$$HCl + 2\ OH^-(aq) \rightarrow 2Cl^-(aq) + H_2O \quad (1.12)$$

$$HF + 2\ OH^-(aq) \rightarrow 2F^-(aq) + H_2O \quad (1.13)$$

Moreover, the other gases present in the mixture that are insoluble in the 4N NaOH solution, such as hydrogen (H_2), carbon monoxide (CO), methane (CH_4), carbonyl sulphide (COS), nitrogen (N_2), oxygen (O_2) and argon (Ar), gather in the headspace of the evacuated collection bottles (Giggenbach, 1975). After the gases have been sampled, the collected bottles are brought in a laboratory where they are re-weighed and then the headspace gases and the ones in solution are analysed with a chromatography

technique that allows to determine the original molar concentrations of all the sampled gas species (Symonds et al. 1994). The water content is then obtained by calculating the difference between the weight gain and the weight of all the non-water gas species. However, samples collected with this solution-filled bottle method may be affected by severe biases both related to the sampling technique and to geophysical and geochemical processes that may affect the gases during or after the sampling (Symonds et al., 1994). In fact firstly, minor amounts of sulfur may be lost by natural depositing before the gas enters the sampling setup and oxygen can react dramatically with certain volcanic gas species such as sulfur itself. Secondly, temperature variation-induced condensation or re-evaporation of liquid in the samples can significantly affect water, sulfur and carbon dioxide contents (Giggenbach and Matsuo 1991). Furthermore, spilling of solution can affect water content and chemical reactions between volcanic gases and the titanium tubing system can produce more gas-Hydrogen (H_2) than expected. Finally, it is impossible to collect only magmatic volatiles because more often volcanic gas samples are a mixture of air, steam, fractioned volcanic volatiles and other gases originated from hydrothermal systems (Symonds et al., 1994). Another method of direct sampling is the in-situ chromatography. This guarantees immediate results directly in the field nonetheless, HCl and HF cannot be measured with this technique and have to be collected by the solution-filled sampling bottle technique anyway (Le Guern et al. 1982).

High temperature volcanic gas samples that were actually collected at high temperature are generally a good indication that the sampled gases were originated from a magmatic source and this also guarantees that samples are close to their thermodynamic equilibrium phase (Symonds et al., 1994). In fact, this is extremely important for collecting reliable samples because previous studies have shown that hot volcanic gases are naturally close to their thermodynamic equilibrium, which means that the temperature and the composition are spatially and temporally uniform throughout the gas (Gerlach and Casadevall 1986; Giggenach 1987). Observations suggested that this thermodynamic equilibrium is the last equilibrium condition in which gases can interact with each other before cooling begins (Gerlach and Casadevall 1986; Gerlach 1993a,b). The literature generally assumes that high temperature volcanic gas samples with a quenched equilibrium describe in a better way the degassed volatiles from shallow magma (Symonds et al., 1994). In order to assess whether a sample is in its quenched equilibrium composition, a thermodynamic evaluation is computed. Disequilibrium samples may be caused by a variety of factors such as poor sampling techniques, extraneous gas components, oxidation and gain or losses of water (Gerlach 1993b). If the sample is not in its thermodynamic equilibrium, a retrieval of equilibrium composition technique may be applied (Symonds et al. 1994). It is assumed that restored equilibrium compositions represent magmatic volatile compositions just as effectively as equilibrium compositions do. After their collection, volcanic gases can be analyzed in several ways. Stable isotope data are extremely important when assessing whether gases are actually exsolved from magma or some other sources like meteoric fluids or water (Allard 1983; Taylor 1986).

Direct gas sampling in areas of high volcanic hazard, especially during vulcanian or Plinian eruptions, is strongly limited for obvious reasons (Scandone and Giacomelli 2004). Furthermore, considering the volumes and the size of eruption plumes and how fast and largely they can expand into the atmosphere, direct sampling is not often the best way of acquiring pieces of information about volcanic volatiles. In fact, in these large eruption cases a synoptic view is certainly much more beneficial in order to obtain reliable data. It is a matter of fact that the plume from Puyehue-Cordón Caulle volcano, Chile in 2011 was able to circle the Southern hemisphere of the Earth in less than ten days (Raga et al. 2013). Furthermore, direct sampling does not guarantee reliable estimates of magmatic volatile contents in areas of high contamination from other gases and it does not allow to measure gases in terms of fluxes. For these reasons, new monitoring techniques were and are still being developed. Such techniques are commonly called remote sensing techniques and allow data collection about volcanic gases without making physical contact with them. This can be done from the ground by simply pointing an instrument at a volcanic plume or even from airplanes and satellites orbiting the Earth (Scandone and Giacomelli 2004). These new techniques are extremely valuable for a variety of reasons. Remote sensing techniques

guarantee much more safety because gases can be monitored from a safe distance. This is extremely important if the volcano is located in a very remote area, like Mount Erebus in Antarctica. Secondly, they give reliable estimates of magmatic volatile contents in areas of high contamination from other gases and allow to measure gases in terms of fluxes. Moreover they give almost instantaneous results and allow detection of precursory activity to volcanic hazards (Hooper et al. 2013). Finally, remote sensing techniques can be potentially applied to many gases (other than sulfur dioxide). This type of measurement has not been widely conducted at active volcanoes because of the technological difficulties, low budgets and signal to noise ratios of the volcanic and atmospheric gas contents (Hooper at al. 2013; Parks et al. 2013). In fact, the two most abundant volcanic gases (carbon dioxide and water) are found in great concentrations in the Earth's atmosphere and therefore, they are very difficult to detect (Symonds et al. 1994).

1.3.3. Remote Sensing

Quenzel (1984) defines remote sensing as the technique by which "*from the state of a field at one location conclusions are drawn about quantities that influenced the field at a different location*". The field carrying information is generally the electromagnetic radiation in the optical wavelength from the UltraViolet (UV) to the InfraRed (IR) parts of the electromagnetic spectrum (Millán 2008). These remote sensing techniques are all based on the radiation transfer problem and on the fact that the concentration of volcanic volatiles present in plumes can be compared with the atmospheric one (William-Jones et al. 2008). However, the abundance of some chemical species may be greater in the atmosphere than in volcanic plumes and moreover, as soon as the venting takes place and the gases are released into the atmosphere, they begin to be diluted. Therefore, if the ratio between the concentration of volcanic gases and their counterparts in the atmosphere (i.e. the signal to noise ratio) is low and close to 1, remote sensing may be very difficult, if not impossible (Scandone and Giacomelli 2004). The only volatile that has a very good signal to noise ratio in the atmosphere (see Table 1.1.) is sulfur dioxide and for this reason, it is very easily measured via remote sensing techniques and has always been considered for proving that new magma is actually rising towards the surface in a volcanic plumbing system.

1.3.4. UV-based tecniques

Classically, SO_2 path-concentrations have been measured using passive spectroscopic approaches. Various sensors have been used to perform point measurements and quantify volcanic SO_2 by measuring its absorption features in the UltraViolet (UV) part of the electromagnetic spectrum (e.g., Moffat and Millan 1971; Stoiber and Jepsen 1973; Stoiber et al. 1983). The most common technique to assess sulfur dioxide concentrations is using a remote sensing instrument called ultraviolet COrrelation SPECtrometer (COSPEC) (Oppenheimer et al. 1998). The COSPEC was initially designed for evaluating ambient concentration of sulfur dioxide however, it became soon a standard volcanic monitoring technique since it was first used at Mount Mihara, Japan in 1971 (Francis et al. 2000). This portable and low power instrument, which is able to effortlessly determine volatiles fluxes from volcanoes, has a long story of successes especially when it predicted the reawakening of Mount Pinatubo in the Philippines two weeks before the seismometers clearly indicated that the 1991 unrest was caused by a magmatic intrusion (Daag et al. 1999) and when it was used to monitor from a safe distance the Soufrière Hills volcano's magma rate extrusions in its almost persistent daily low clouds (Young et al. 1998).

The COSPEC makes use of the solar UV light transmitted and scattered by the atmosphere of the Earth as a source of light to measure the light absorption by SO_2 molecules in a volcanic plume and in turn, it converts these pieces of information into concentration transect data by calibration against standard SO_2 reference cells (Symonds et al. 1994). The instrument is a spectroscopy, whose optical system can be divided in three parts: front optics, polychromator section and rear optics (Millán, 2008). The first part is composed of a telescope, which collects light from a suitable background with spectral radiance L (W sr^{-1} m^{-2}) and focuses it on the entrance slit of a polychromator at the beginning of the mid

optics section, where the radiation is collimated by an ebert mirror, which produces a semi-parallel beam of light with irradiance Hh (W m^{-2}), and sent to a grating element that disperses the light into the fundamental wavelengths. These diverging beans are then gathered by a second mirror to form the spectrum. Finally, the rear optics separates specific sets of wavelength intervals and focuses them into a computer connected photo-detector to estimate the sulfur dioxide concentration (Millán 2008).

In order to obtain specific details about SO_2 fluxes from a volcano, its concentration transect datasets have to be multiplied by wind speed measurements. However, this latter piece of data generally represents one the greatest source of uncertainty in COSPEC measurements (Stoiber et al. 1983). In fact, despite the fact that the measurements, which can be taken both from the ground and from the air, may be improved by taking them from an aircraft in order to derive good wind speed data from the aircraft navigational instruments, Francis et al., 2000 remembered that the cumulative source of errors for a COSPEC-based technique may range between 15 and 40%. Large errors are one of the biggest problems in COSPEC measurements. Another disadvantage that has been discussed is that the COSPEC cannot be used in night or very low light conditions and for this reason, it does not guarantee reliable measurements during very powerful eruptions, such as the Plinain ones, in which ash absorbs much of the solar light (Scandone and Giacomelli 2004). Furthermore, since in the air SO_2 is converted to sulphate aerosols, COSPEC-SO_2 estimates can be significantly decreased (Francis et al. 2000). However, the biggest problem that COSPEC instruments have to face is probably the fact that they are no longer produced and as a result, spare parts are going to be very difficult to find (Francis at al., 2000). However, new lightweight UV spectrometers such as FLYSPEC, DOAS and mini-DOAS and RMDI have recently started to replace it (Williams-Jones et al. 2008).

UV imaging has recently been performed at active volcanoes (e.g., Bluth et al. 2007; Mori and Burton 2009; Kern et al. 2013). Such imaging can provide valuable synoptic views of the spatial distributions of SO_2 from which fluxes can be derived (e.g., Bluth et al. 2007). A limitation, however, is that these UV techniques, both imaging and non-imaging, can only be used for SO_2 retrievals and only work during the daytime, not at night.

1.3.5. IR-based techniques

FTIR is one of the most promising techniques for providing rapid and effective remote measurements of a wide range of volcanic phenomena. This geochemistry based technique has only recently been applied to active volcanoes, however, it proved to be extremely effective in acquiring reliable pieces of information for the surveillance of volcanic volatiles and, therefore, for producing robust data that help understanding the mechanisms that rule the chemical equilibria in rising magmas and the atmospheric volcanic degassing and most importantly assessing volcanic hazards (Hooper et al. 2013). This technique is based on the fact that matter and electromagnetic radiation can interact with each other and particularly that some molecules are IR-active. This means that when an IR radiation is passed through an IR-active sample, some of the radiation is absorbed and some of it is transmitted. In fact, the chemical covalent bonds, that enable the atoms to attract each other and form molecules, are able to absorb part of the radiation they are subjected to and utilize it to change energy state and vibrate at their fundamental frequencies according to the Schrödinger equation (Pecsok and Schields 1968; Schwartz et al. 1994). The transmitted part of the radiation that is able to reach the detecting spectrometer is then split into its fundamental frequency components and its spectrum is acquired. In this case, the spectrum can be seen as a sort of molecular fingerprint of the sample. In fact, no two unique molecular structures have the property of creating the very same absorption pattern in the spectrum. Therefore, FTIR spectroscopy is extremely effective determining and quantifying the components of a mixture. In order to be IR-active, a molecule must possess an electric dipole, consequentially, all the main volcanic volatiles (H_2O, CO_2, SO_2, HCl, CO, SiF_4, OCS and HF) are IR-active (Schwartz et al. 1994). SO_2, for example, displays absorption features at 7.3 and 8.6 μm (Watson et al. 2004)

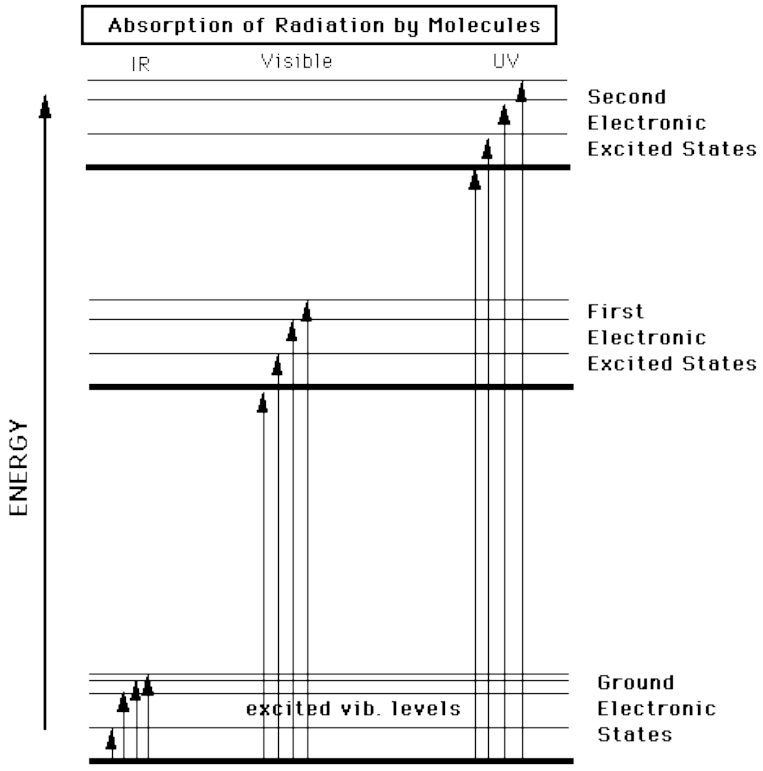

Figure 1.3. Schematics of radiation absorption by molecules. Adapted from Schwartz et al., 1994

Electromagnetic waves propagates at the speed c and are characterized by their frequency ν and amplitude A. Plank's law describes that the energy E of an electromagnetic wave is proportional to the wave's frequency. This means that the higher the frequency, the higher the energy of the wave. It is the IR region of the spectrum energy that is responsible for exciting vibrations in IR-active molecules that are the basic ingredient of the IR spectroscopy. Very energetic waves, such as UV and X-rays, are even able to trigger strong molecule vibrations by forcing electrons to jump from their ground state up to their second electronic excited states and even induce ionization (Figure 1.3) (Schwartz et al. 1994).

FTIR spectroscopy of volcanic plumes consists of detecting the multi-frequency IR radiation emitted by a source (i.e. the sun or an active lava lake) and obtain its spectrum. In fact, the IR-active volcanic gases in the radiation optical path will absorb part of the radiation leaving gaps or absorbance negative pecks in the IR spectrum at the fundamental frequencies the IR-active molecules vibrate (Oppenheimer et al. 1998). The depth of the negative peaks can be related to the concentration of the gas K thanks to the Lambert-Beer Law, which states that:

$$I_\nu = I_{0\nu} e^{\varepsilon_\nu K \omega} \tag{1.14}$$

where $I_{0\nu}$ is the initial intensity of the IR electromagnetic wave, I_ν is the measured intensity at a specific frequency ν, K is the concentration of the species, ε_ν is a coefficient that describes how strongly a chemical substance absorbs IR radiation and ω is the path length. Converting Equation 1.14 into its logarithmic form, it is possible to write:

$$\log\left(\frac{I_\nu}{I_{0\nu}}\right) = \varepsilon_\nu K \omega \tag{1.15}$$

This means that the logarithm of the ratio between the intensity of the sample and the background equals the absorbance of the IR electromagnetic wave that occurs along a certain optical path where a certain volatile is present (Oppenheimer et al. 1998). The standard configuration of an FTIR

spectrometer in the field includes a Michelson interferometer, a cooled broad band computer-controlled detector and its fore-optics (Ferrec et al. 2006).

The Michelson interferometer is an instrument with a particular optical configuration that allows optical interferometry of two beams of light. It consists of two mirrors that are normal to the incoming radiation and one beam splitter. The electromagnetic wave emitted by a source is partly transmitted and partly reflected by the beam-splitter. As a result, the two splitted beams are subjected to two different optical paths and are sent to the two mirrors that reflect them back to the beam-splitter. This recombines them into one beam that is sent to a detector. The difference in the length of the two optical paths of the transmitted and the reflected beams allow them to interfere with each other and create an interference pattern. In the Michelson interferometer part of the FTIR spectrometer the two mirrors are replaced by two reflective cube corners. Furthermore, one of them is placed on a computer driven translation plate that makes a δ difference in the optical path of the two beams every time it makes a $\delta/2$ move. The signal acquisition is run by a computer in a synchronic way with the cube transaction so that the whole interferogram can be measured and plotted against δ.

The most important property of the interferogram is that every data point, which makes up the signal and is a function of the position of the moving reflective cube, contains pieces of information regarding every IR frequency of the transmitted radiation. For this reason, in order to obtain pieces of information regarding the spectrum of the signal, it is necessary to decode the interferogram into its individual frequencies. This can be done thanks to the well-known Fourier Transform analysis.

The Fourier Transform is one of the most important mathematical functions for manipulating signals. It was firstly introduced in 1822 by the French mathematician and physicist Jean Baptiste Fourier. Since then, this remarkable function has been widely used in science, particularly in physics and engineering. In fact it allows to transform a signal from the time or space domains to the frequency domain. Therefore, if $f(t)$ is a general signal in the time t or space δ domains, the Fourier transform $\mathcal{F}$ *enables to obtain a new function* $\mathrm{F}(\nu)$ *in the frequency* ν *domain.*

$$f(t) \overset{\mathcal{F}}{\Rightarrow} F(\nu) \tag{1.16}$$

This is extremely important because a complex signal, which can be seen as the result of the combination of many simpler signals, can be expressed in terms of the frequencies that actually form it. Therefore, this remarkable tool enables to determine the main components of a signal in terms of frequency just as like a soup filter allows a chef to determine whether a soup has more broccoli or black-eyed beans!

The Fourier Transform can be calculated for any general signal according to the following definition:

$$F(\nu) = \mathcal{F}[\mathrm{f(t)}] = \int_{-\infty}^{+\infty} \mathrm{f(t)} e^{-2\pi i \nu t} dt \tag{1.17}$$

Furthermore, it is reversible. So, the following operation is allowed:

$$f(t) \overset{\mathcal{F}}{\Leftarrow} F(\nu) \tag{1.18}$$

The Inverse Fourier Transform is defined as:

$$f(t) = \mathcal{F}^{-1}[\mathcal{F}(\nu)] = \int_{-\infty}^{+\infty} \mathcal{F}(\nu) e^{2\pi i \nu t} d\nu \tag{1.19}$$

The Parseval's identity enables to calculate the energy of a certain signal. In fact,

$$\int_{-\infty}^{+\infty} |f(t)|^2 dt = \int_{-\infty}^{+\infty} |F(\nu)|^2 d\nu \quad (1.20)$$

where $\int_{-\infty}^{+\infty} |F(\nu)|^2 df$ represents the energy of the signal, $|F(\nu)|^2$ is the energy of the signal in every infinitesimal interval of frequency $d\omega$ and $|F(\nu)|^2$ is the energy spectral density.

Open-path Fourier Transform InfraRed (FTIR) spectroscopy can be employed for retrieving various gas path-concentrations (SO_2, CO_2, H_2O, and SiF_4), which have spectral features in the TIR part of the electromagnetic spectrum, both during the day and night (Love et al. 1998; Francis et al. 1998; Oppenheimer et al. 1998; Goff et al. 2001; Oppenheimer et al. 2006; La Spina et al. 2015). Despite the high spectral resolution and the possibility of multiple gas retrievals, FTIR is still mostly based on point measurements. Recently, both low spectral resolution and hyperspectral thermal imaging have been performed, respectively by Prata and Bernardo (2014).

1.4. The main objectives of the dissertation

As part of this project, results from IR hyperspectral imaging at high resolution are described. The goal of this project is to combine the advantages of both FTIR's night time measurements and high spectral resolution and UV's imaging capabilities. A newly developed remote sensing long-wave Thermal IR (TIR) hyperspectral imaging spectrometer (Thermal Hyperspectral Imager, THI; Wright et al. 2012) was built and tested. The sensor is suitable for acquiring high spectral resolution images of volcanic plumes from which SO_2 emission and absorption spectra can be retrieved. Theoretically, there is no reason why other volcanic gases, which have spectral features in the 8-14 μm infrared wavelengths range, cannot also be quantified.

The main goal of this project is to test the applicability of Thermal InfraRed (TIR) hyperspectral imaging spectroscopy for retrievals of volcanic gas flux. Volcanic volatiles targets have distinctive absorption spectra in the long wave infrared (Schwartz et al. 1994). Therefore, it is inferred that ground-based interferometry has a remarkable potential for detecting these targets at high spatial, spectral and temporal resolution. This new piece of research will be conducted both in the field, specifically at Kīlauea volcano, Hawai'i, and in the lab to prove that the new technology is actually able to detect and quantify the concentration of various volcanic volatiles. The main results were summarized in three main chapters.

The second chapter is entitled: "THI: Characterization and initial field test of a 8-14 micron thermal infrared hyperspectral imager for measuring SO2 in volcanic plumes" and illustrates the sensitivity study for measuring sulfur dioxide, which was carried out both in the field and the lab with well calibrated laboratory experiments. The third chapter is: "Validating the Accuracy of SO2 Gas Retrievals in the Thermal InfraRed (8-14 μm)" and deals with comparing published retrieval algorithms with a new one, based on Partial Least Squares Regression, that was created as part of this dissertation project. The fourth chapter is "Applications of Quantitative Thermal InfraRed Hyperspectral Imaging (8-14 μm): Measuring Volcanic SO2 Fluxes and Determination of Plume Transport Speed Using a Single Sensor". This last chapter brings together the first two by describing field measurements at Kīlauea volcano, which were carried out with the characterized sensor, described in chapter 2, and the new inversion algorithm, tested in chapter 3.

CHAPTER 2

CHARACTERIZATION AND INITIAL FIELD TEST OF A 8-14 MICRON THERMAL INFRARED HYPERSPECTRAL IMAGER FOR MEASURING SO_2 IN VOLCANIC PLUMES

Published as: Gabrieli, A., Wright, R., Lucey, P.G., Porter, J.N., Garbeil, H., Pilger, E., Wood, M. (2016). Characterization and initial field test of a 8-14 μm thermal infrared hyperspectral imager for measuring SO_2 in volcanic plumes. Bulletin of Volcanology, doi: 10.1007/s00445-016-1068-6

Abstract — The ability to image and quantify SO_2 path-concentrations in volcanic plumes, either by day or by night, is beneficial to volcanologists. Gas emission rates are affected by the chemical equilibria in rising magmas and a better understanding of this relationship would be useful for short term eruption prediction. A newly developed remote sensing long-wave thermal InfraRed (IR) imaging hyperspectral sensor – the Thermal Hyperspectral Imager (THI) – was built and tested. The system employs a Sagnac interferometer and an uncooled microbolometer in rapid scanning configuration to collect hyperspectral images of volcanic plumes. Each pixel in the resulting image yields a spectrum with 50 samples between 8 μm and 14 μm. Images are spectrally and radiometrically calibrated using an IR source with a narrow band filter and two blackbodies. In this chapter, the sensitivity of the instrument is evaluated for the purposes of quantifying SO_2 using well constrained laboratory experiments and initial field results from Kīlauea volcano, Hawai'i, are presented. The sensitivity of THI was determined using gas cells filled with known concentrations of SO_2 and using National Institute of Standards and Technology (NIST)-traceable blackbodies to simulate a range of realistic background conditions. Measurements made by THI were then benchmarked against a high spectral resolution off-the-shelf Michelson FTIR instrument. Theoretical thermal IR spectral radiances were computed with MODTRAN5 for the same optical conditions, to evaluate how well the (known) concentration of SO_2 in the gas cells could be retrieved from the resulting THI spectra. Finally, THI was recently field-tested at Kīlauea to evaluate its ability to image the concentration of SO_2 in a real volcanic plume. A path-concentration of 7 150 ppm-m was retrieved from measurements made near the Halema'uma'u vent.

2.1. Introduction and background

Volcanic degassing measurements are a key component of monitoring active volcanoes. The composition and emission rates of volcanic gases are linked with magma dynamics and magma composition in volcanic plumbing systems that could fuel eruptions (Parfitt and Wilson 2008). Measuring both passive and explosive degassing is key to obtaining gas flux information, which reflects both magma supply rate and magma permeability, i.e. closed or open degassing, or a superposition of both (Stix and Gaonac'h 2000). Water vapor (H_2O), carbon dioxide (CO_2), sulfur dioxide (SO_2), and smaller contributions of H_2S, CO, H_2, N_2, HCl, HF, SiF_4, and HBr are dissolved in magma under the high pressure of the upper mantle or lower crust (e.g., Wallace et al. 2015). As magma rises in volcanic conduits and the pressure decreases, the volatiles begin to exsolve from the silicate melt liquid and form gas-phased bubbles. As these bubbles rise and grow by diffusion, decompression and coalescence, they lower the bulk density of magma. The rate of degassing becomes larger as the pressure decreases and the magma rises and tends to lose its volatile content (Parfitt and Wilson 2008). This loss of volatiles is accompanied by rapid release and expansion of gas that can induce the magma to break apart and be erupted explosively (Wilson and Walker 1987).

Volcanic gases provide insights into short term volcanic eruption prediction (e.g., Parfitt and Wilson, 2008). The detection of anomalous concentration of volcanic volatiles, which in high temperature volcanic gas emissions consist mainly of H_2O, CO_2 and SO_2, helps volcanologists to infer the physical and chemical processes magma is subjected to within volcanic systems. Emission rates are often correlated with explosive activity, in some cases preceding it by days or weeks. For instance, Noguchi and Kamiya (1963) and Werner et al. (2013) showed respectively that eruptions of Mount Asama, Japan and of Mt. Redoubt (Alaska) could be forecast with some degree of accuracy by measuring the variations of CO_2 and especially SO_2 emissions from their active craters. In fact, unlike CO_2 and H_2O, the presence of non-volcanic SO_2 in the troposphere is negligible and therefore, its detection is much easier compared with detecting volcanic CO_2 and H_2O. Information on magma movements can therefore, be derived from the short-term variability of SO_2 volcanic gas emissions, as well as their correlation with seismic and geodetic measurements. Therefore, monitoring techniques are needed to effectively study volcanic emissions and plumes.

SO_2 gas has absorption bands in the Ultra-Violet (UV) region (300 nm - 320 nm) of the electromagnetic spectrum. Various sensors have been used to measure SO_2 absorption features from which SO_2 gas concentrations were derived. COSPEC sensors employ scanning monochromators (e.g., Moffat and Millan 1971; Stoiber and Jepsen 1973 and Stoiber et al. 1983). DOAS, FLYSPEC, mini-DOAS sensors use a multi-wavelength spectrometer to measure all the wavelengths simultaneously (e.g., Weibring et al. 1998; Weibring et al. 2002 and Horton et al. 2006). These various methods have been used at activate volcanoes to estimate SO_2 emissions (e.g., Daag et al. 1996; Galle et al. 2002; Williams-Jones et al. 2008 and Dalton et al. 2009), but do not provide image data. UV imaging of SO_2 plumes is less common, but has been performed for stack plumes (Exton 1976) and active volcanoes (Mori and Burton 2006; Mori and Burton 2009 and Kern et al. 2015). Such imaging can provide valuable information on how SO_2 concentration varies spatially within the plume, and how this varies with time, and the derivation of gas fluxes. A limitation, however, is that these techniques, imaging or non-imaging, only allow for the retrieval of SO_2, and then only during the day not at night.

Open-path Fourier Transform InfraRed (FTIR) spectroscopy can be used to measure both spectral absorption and emission features of multiple gases (SO_2, CO_2, H_2O, and SiF_4) at 3-5 μm and 8-14 μm infrared wavelengths, and has been demonstrated to be useful at active volcanoes many times (e.g., Love et al. 1998; Francis et al. 1998; Oppenheimer et al. 1998; Goff et al. 2001; Oppenheimer et al. 2006 and La Spina et al. 2015). Although measurements made using this technique are of high spectral resolution (e.g. 0.5 cm^{-1}) over the wavelength range required to allow for retrieval of multiple gases, they are still point measurements, not imaging techniques. More recently, low spectral resolution (three wavelengths) thermal imaging of volcanic plumes has been demonstrated by Prata and Bernado 2014.

In this chapter, I describe results from IR hyperspectral imaging at high resolution to combine the advantages of FTIR's night time measurement and high spectral resolution capabilities and UV's imaging abilities. A newly developed remote sensing long-wave Thermal IR (TIR) hyperspectral imaging spectrometer (Thermal Hyperspectral Imager, THI; Wright et al. 2012) is described in this chapter, which is suitable for acquiring high spectral resolution images of volcanic plumes from which SO_2 emission and absorption spectra can be retrieved. THI employs a Sagnac interferometer (Figure 2.1; Lucey et al. 2008), which comprises three mirrors aligned at 90° angles, and a zinc selenide (ZnSe) beam splitter. Light from the scene enters the interferometer and upon striking the beam splitter is split into a reflected and transmitted component, which travel around the cube in opposite directions and with different path-lengths. Upon being recombined at the beam splitter a phase shift will have been introduced by the differing path-lengths, resulting in interference. This modulated light is then focused onto an uncooled microbolometer array (a FLIR Photon 320). Microbolometers are attractive because they are cheap, simple to use, mechanically robust, and consume relatively little power. However, they are much less sensitive than cooled photon detectors, resulting in low signal-to-noise ratios if filters (or a dispersive method) are used to generate the spectral information. By using an interferometric technique high SNRs can be attained even with the uncooled detector array, as a result of the multiplex advantage (Fellgett 1949).

Figure 2.2 illustrates how THI works. A single frame contains all Optical Path Differences (OPD), one per column, which are needed to construct an interference pattern and spectrum (in Figure 2.2 grains of quartz on a microscope stage are used for illustration). However, in a single frame each OPD samples a different scene element, whereas a spectrum of a scene element requires all OPDs. These are obtained by scanning the scene through the continuously varying OPD field of the camera (Lucey et al. 2008). This is done by employing a high precision scanning mount. Therefore, imaging requires that the interference pattern be scanned across the scene (Lucey et al. 2008) so that light from all scene elements can be sampled at all the optical path differences generated by the interferometer (e.g. the quartz grain marked with a red arrow). Co-registering the frames then allows an interferogram to be retrieved for each scene element, from which a spectrum can be derived using standard Fourier Transform processing (specifically following Mertz 1965). Spectral errors introduced as a function of the registration error are minimal in case of poorly defined boundaries of slow moving objects with very little thermal contrast such as volcanic plumes. To convert "magnitude vs. frequency" to "spectral radiance vs. wavelength" the data must be spectrally and radiometrically calibrated. Images are spectrally calibrated by using an IR source with a narrow band filter, while the data are radiometrically calibrated using two blackbodies set at known temperatures. Each pixel in the resulting image cube contains a spectrum of 50 samples covering wavelengths from 8 μm to 14 μm. The spectral resolution is linear in wavenumber space (40 cm^{-1}; in wavelength units, resolution is inversely proportional to wavelength with bandwidths ranging from 0.25 μm at 8 μm to 0.3 μm at 14 μm.

The spectral and imaging capabilities of THI make it ideal for mapping SO_2 volcanic emissions. In this chapter, we first describe a series of well calibrated laboratory experiments aimed at determining the sensitivity of the instrument and measurement technique for quantifying volcanic SO_2 gas concentrations. We then show preliminary results of how THI can be used to quantify SO_2 in real volcanic plumes, using measurements made at Kīlauea volcano, Hawai'i.

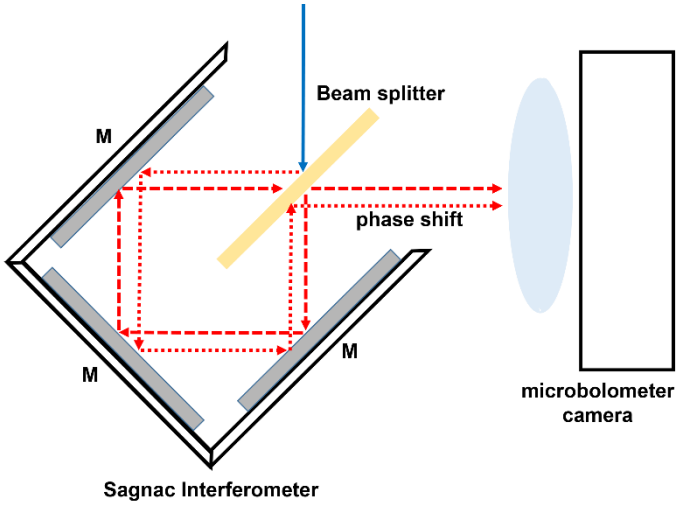

Figure 2.1. The Sagnac interferometer, which is employed in THI. The input beam of light (blue line) is divided into reflected (red dotted line) and transmitted (red dashed line) components by the beam splitter (displayed in yellow). The two beams are reflected by three mirrors (M) before being recombined at the beam splitter, and focused onto the microbolometer.

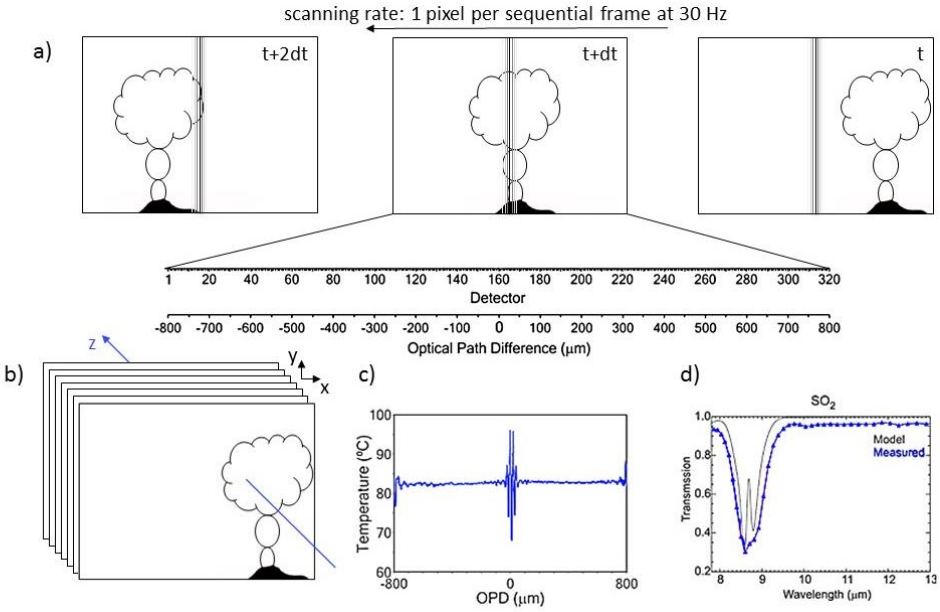

Figure 2.2. a) Schematics of raw data-images acquired by THI of a sulfur dioxide-rich volcanic plume. The interference fringes are apparent and can be seen as vertical lines in the center of the THI frames. Light from each element of the target is phase-shifted so that it varies linearly across the array from left to right. The center burst of the interferogram is at zero path difference (ZPD). THI frames are acquired at a rate of 30 Hz. **b-c)** Illustration of how an interferogram can be obtained for each scene element via spatial autocorrelation of a sequence of images frames. **d)** A measured spectrum of sulfur dioxide gas obtained with THI (blue dotted line). A high resolution laboratory spectrum of sulfur dioxide gas (black solid line) is also shown for comparison purposes.

2.2. Sensitivity analysis: simulating volcanic plume measurements in the laboratory

Laboratory measurements were carried out to validate the THI-derived spectral radiance-to-SO_2 path-concentration inversion process. Figure 2.3 shows the experimental set-up schematically. In the field the sensor would occupy a position on one side of the plume. Light from the opposite side of the plume (the background, in this example from the sky) passes through the plume, with light at certain wavelengths being absorbed by SO_2 at the characteristic wavelengths. If the temperature of the

background is known then the amount of light that enters the plume can be predicted accurately. If no SO_2 is present, then all of the light will make it to the sensor to be detected. But if SO_2 is present, light at the characteristic wavelengths (i.e. a spectral feature centered at 8.6 µm) will be absorbed by the plume, resulting in a reduction in the amount of energy detected at such wavelengths. In addition, the plume will emit light of its own. The net effect is that the spectra measured by THI would be the sum of light transmitted by the plume from the background plus light emitted by the plume itself, which THI measures at each of the 50 wavelengths between 8 µm and 14 µm. THI measurements of TIR spectral radiance, which include both emission and transmission information, were carried out in the laboratory using custom gas cells (10.16 cm diameter and 10 cm long), fabricated using CPVC material and IR-transparent zinc selenide (ZnSe) windows, and a temperature controlled NIST-traceable blackbody (Figure 2.4). The gas cell and gas concentrations used in this study were selected so that the path-concentration (ppm concentration times distance) of SO_2 was comparable to that which might be found in a volcanic plume. Grutter et al. 2008, Elias and Sutton 2012, Kern et al. 2012, and Kern et al. 2013 reported SO_2 path-concentrations ranging from 0 ppm-m to 16 000 ppm-m at volcanoes situated in various geological settings (e.g., hot spot and subductions zones) and various plume widths (i.e., > 500 m). At Kīlauea, DOAS and FLYSPEC measurements at the summit indicate SO_2 path-concentrations of up to 10 000 ppm-m (Kern et al. 2012 and Kern et al. 2013). A 10 cm long gas cell, filled with 7% SO_2 gas (with inert N_2 balance at ambient pressure) has a path-concentration of 7 000 ppm-m.

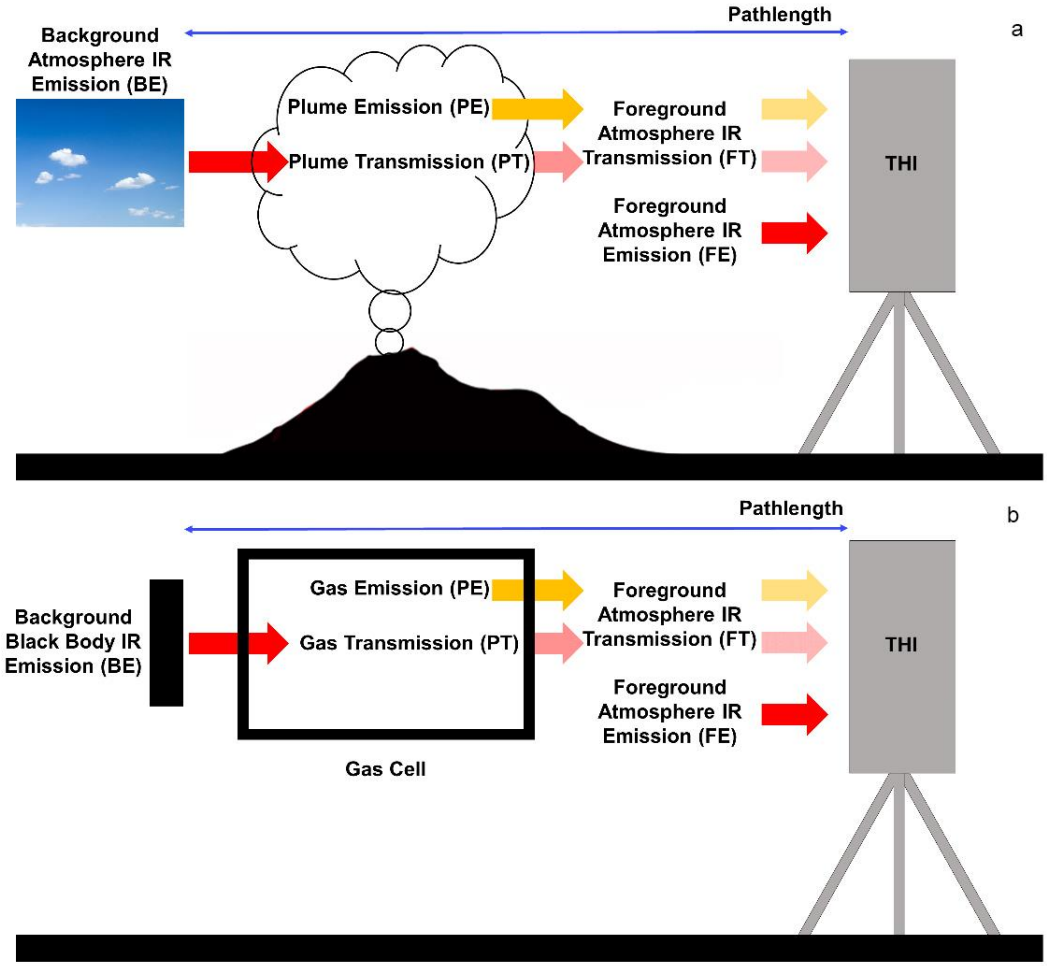

Figure 2.3. Simulating volcanic plume conditions. **a)** Above: on the left the background atmosphere provides Background Emission (BE). Within the volcanic plume, BE is attenuated and Plume Emission (PE) is occurring. Within the foreground region, both PE and the attenuated BE are further attenuated. **b)** The same scenario is modelled with the gas cell.

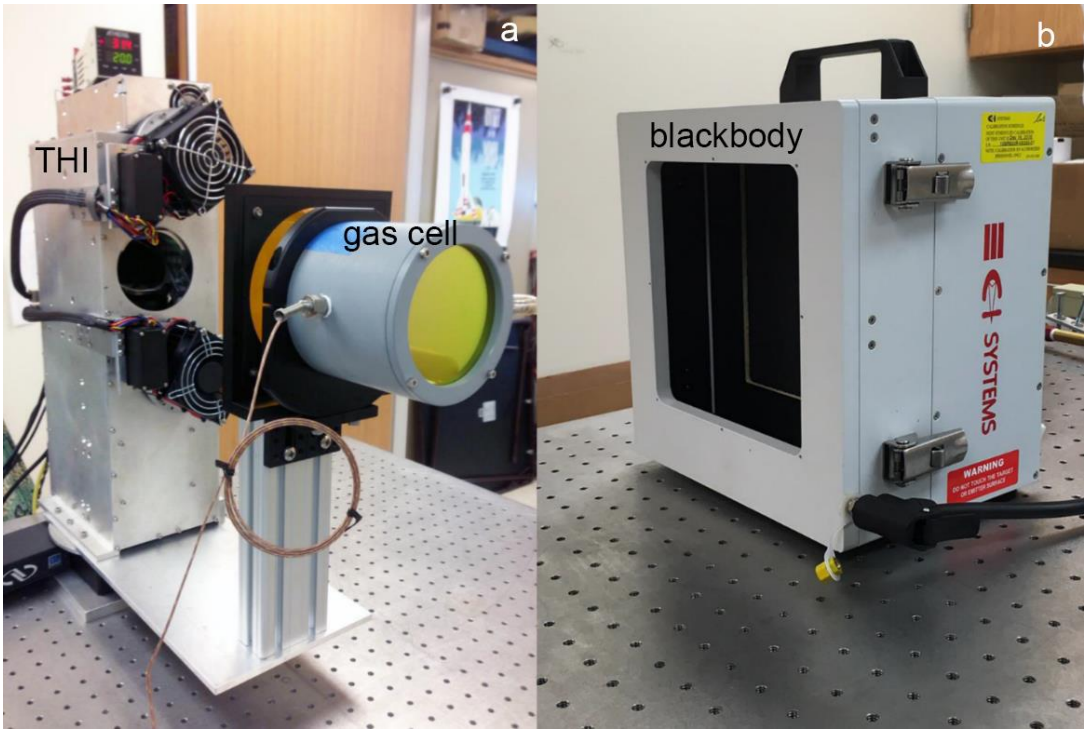

Figure 2.4. a) THI with a custom gas cell (diameter = 10.16 cm and length = 10 cm) mounted in front of its aperture for simulating the volcanic plume. **b)** A temperature controllable NIST-traceable blackbody used to simulate the background THI-characterization studies in the lab.

The temperature of the night sky depends on environmental and atmospheric conditions, and elevation angle. For example, the temperature of the night sky at an elevation angle of 90 ° is close to 80 °K (Love et al. 1998 and Goforth et al. 2002). In our case, it was necessary to consider a lower elevation angle in order to effectively simulate the necessary slant paths for observing volcanic plumes. The Swinbank formula allows for estimates of the temperature of the night sky at various elevation angles, relative humidity and atmospheric conditions. Assuming elevation angles lower than 30 °, a clear night on the summit of Kīlauea with a typical temperature of + 15 °C and a relative humidity of 25 % for the Swinbank formula, a blackbody temperature of - 10 °C was chosen for modelling the temperature of the night sky. Similarly, a temperature + 10 °C was obtained for daytime (Swinbank 1963 and Goforth et al. 2002). The gas cells were filled with various SO_2 gas concentrations and the blackbody temperature was varied from - 10 °C to + 10 °C to simulate background conditions such as daytime and night time skies, and then up to + 50 °C to simulate hot background conditions such as rocks heated by the sun. The effects of emission and absorption from the windows of the gas cell and the temperature effects of the SO_2 gas were accounted for in the study. The SO_2 gas was maintained at constant temperature and actively controlled by using a thermocouple and a regulator-controlled heating tape.

For these laboratory conditions, the THI observed spectral radiances depend upon the blackbody temperature, the blackbody spectral emissivity, the gas cell concentration, the gas temperature, the absorption and emission of the windows, the effect of the intervening atmosphere, and the spectral response of THI. The NIST-traceable blackbody spectral emissivity was assumed to be unity. The THI spectral response was determined by observing the spectral radiances from the blackbody at different temperatures. The various source terms are interrelated and are defined by Equation 2.1 and Figure 2.3, which summarize both laboratory and plume measurement scenarios:

$$L = FT \cdot (BE \cdot PT + PE) + FE \tag{2.1}$$

The THI measured spectral radiance (L) depends upon the Background Emission (BE). This could be the sky behind the plume or the blackbody behind the gas cell. PT is the Plume Transmission or the

gas transmission (within the gas cell). PE refers to the Plume Emission or the emission from the gas (within the gas cell). FE and FT are respectively the Foreground Emission and the Foreground Transmission (for either the lab or the field conditions). For example, if THI spectral radiance measurements were made using SO_2 gas concentration of 0 %, 2 %, and 7 % (i.e., null case, 2 000 ppm-m, and 7 000 ppm-m) and blackbody temperatures of + 5 and + 50°C, the following pair of linear equations can be solved and emission and transmission components of the THI spectra retrieved.

$$\begin{cases} L_5 = FT \cdot (BE_5 \cdot PT \cdot gcT + PE) + FE \\ L_{50} = FT \cdot (BE_{50} \cdot PT \cdot gcT + PE) + FE' \end{cases} \quad (2.2)$$

where: BE_5 is the background emission of the blackbody set at + 5 °C, BE_{50} is the background emission of the blackbody set at + 50 °C and gcT is the transmission of the empty gas cell.

Similarly, a pair of linear equations can be solved if the gas cell is empty. In this case:

$$\begin{cases} \widetilde{L_5} = FT \cdot (BE_5 \cdot PT \cdot gcT + PE) + FE \\ \widetilde{L_{50}} = FT \cdot (BE_{50} \cdot PT \cdot gcT + PE) + FE' \end{cases} \quad (2.3)$$

where: $\widetilde{L_{50}}$ is the spectral radiance measured when looking through the empty gas cell at the background blackbody set at + 50 °C (PT=1) and $\widetilde{L_5}$ is the spectral radiance measured when looking through the empty gas cell at the background blackbody set at + 5 °C.

Solving for PE and PT, leads to

$$\begin{cases} PT = \dfrac{L_{50} - L_5}{\widetilde{L_{50}} - \widetilde{L_5}} \\ PE = L_{50} - (\widetilde{L_5} \cdot PT) \end{cases}, \quad (2.4)$$

This inversion algorithm is possible in the laboratory because the temperature of the background is known, providing at least two background temperatures for setting up the required simultaneous equations.

2.3. Results: laboratory characterization of the THI instrument

In order to study the sensitivity of the instrument for SO_2 retrieval, THI measurements of TIR spectral radiances were carried out in the laboratory using custom gas cells and a temperature controlled NIST-traceable blackbody. Initially, in order to isolate SO_2 emission and transmission spectral information, measurements were carried out with the background blackbody at two different temperatures, and for empty and SO_2-filled gas cells (0 %, 2 %, and 7 % at the constant temperature of + 20 °C). For this purpose, the simplified inversion algorithm of Equation 2.4 was used. Figure 2.5 shows spectral radiances for different background temperatures and different SO_2 concentrations measured with THI.

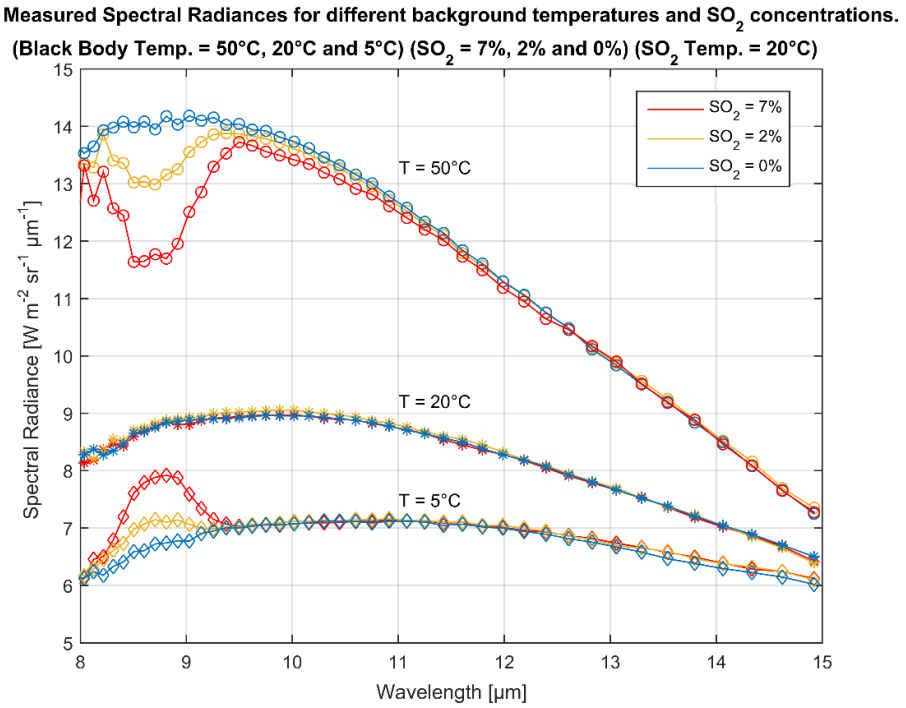

Figure 2.5. THI measured spectral radiances for different background temperatures (+ 5 °C, + 20 °C, and +50 °C) and different SO_2 concentrations (0 %, 2 %, and 7%). The shape of the SO_2 spectral feature at 8.6 µm clearly depends on the background temperature.

When the background temperature is higher than the gas temperature, the SO_2 gas causes a reduction in the measured spectral radiance at 8.6 µm (i.e. absorption of background radiance by the gas is more important than emission from the gas). Conversely, if the background temperature is lower than the gas temperature, the SO_2 gas induces an increase in the measured spectral radiance in the same wavelength region. Finally, if the background blackbody emits at the same temperature of the SO_2 gas, the SO_2 gas effects cannot be seen, because emission and absorption cancel out. Clearly, the instrument can distinguish between these gas concentrations, in both absorption and emission. Additionally, this emphasizes how critical the temperature of the plume is for retrieving SO_2 gas path-concentrations: if the plume temperature is not known accurately, then it will be very difficult to estimate SO_2 path-concentrations.

To confirm the robustness of the THI measurements they were benchmarked against those obtained from a commercial off-the-shelf non-imaging Michelson FTIR spectrometer. The Design & Prototypes (D&P) Model 102 spectrometer uses a Michelson interferometer and a cryogenically cooled InSb/MCT detector to yield high signal-to-noise point spectra between 2-16 µm, with a spectral resolution of 4 cm^{-1}, substantially higher than THI. Figures 2.6a and 2.6b show SO_2 emission and transmission curves derived from THI and D&P measurements following Equation 2.4. The D&P spectrometer has a higher spectral resolution (4 cm^{-1}) than THI (40 cm^{-1}) and therefore, the resolution of the D&P data was reduced by applying a weighted average. The general location and features of the SO_2 emission and absorption curves are similar for both THI and D&P observations, confirming that the THI measurements are robust.

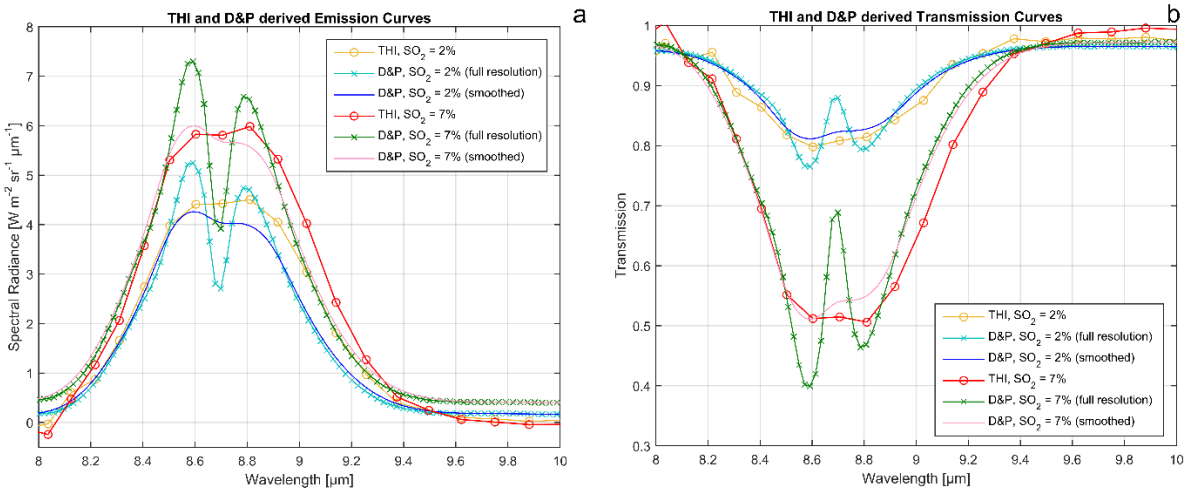

Figure 2.6. a) Comparison between the spectral SO_2 emission curves derived from the THI measurements (yellow and red lines) and a separate non-imaging higher resolution Thermal IR D&P spectrometer. **b)** Comparison between the spectral SO_2 transmission curves derived from the THI measurements (yellow and red lines) and a separate non-imaging higher resolution Thermal IR D&P spectrometer. The D&P spectrometer has higher spectral resolution (4 cm^{-1}) than THI and therefore, D&P data were smoothed to similar THI resolutions.

Following from these initial experiments, we examined how well THI could discriminate between a wider range of SO_2 concentrations. The temperature of the SO_2 gas was set to +20 °C and the blackbody was set to either -10 °C or +10 °C to simulate the temperature of the sky in tropical regions during night time and daytime (at low elevation angles, with typical ambient temperatures of 15°C and relative humidity of 25%) to try to encompass something of the natural variability that would be encountered in the field (Swinbank, 1963; Goforth et al., 2002).

Measurements were conducted at each background temperature (−10°C and +10°C) with SO_2 concentrations equivalent to 100 ppm-m, 300 ppm-m, 500 ppm-m, 1 000 ppm-m, 2 000 ppm-m, 3 000 ppm-m, 4 000 ppm-m, 5 000 ppm-m, 6 000 ppm-m, and 7 000 ppm-m. For each experiment 50 THI spectra were obtained to establish repeatability, and the mean and standard deviation of the spectral radiance at each wavelength were computed (Figure 2.7a and 2.7b). In order to express the THI sensitivity in SO_2 units, ratios of measured spectral radiance obtained when looking through a filled gas cell and an empty gas cell were determined (Figure 2.7c and 2.7d). To aid interpretation, we note that the results on the left hand side (2.7a and 2.7c) are indicative of best-case instrument performance (i.e., good plume-background contrast), while the figures on the right hand side (7b and 7d) are indicative of worst case performance (i.e. poorer plume-background contrast). Assuming a Kīlauea-like volcanic plume width of 500 m (Kern et al. 2012), THI can detect SO_2 gas path-concentrations as low as 100 ppm-m with a background temperature of −10°C (i.e., somewhat ideal observation conditions, at night with a high elevation angle; Figure 2.7b) and as low as 1 000 ppm-m with a background temperature of +10°C (i.e., much less ideal observations conditions, during the day, at low elevation angles; Figure 2.7a). Figure 2.8 shows path-concentrations observed at Kīlauea by Kern et al. (2012), and it appears that, with the established daytime and nighttime sensitivity, THI would be able to resolve the same temporal trends in SO_2 degassing.

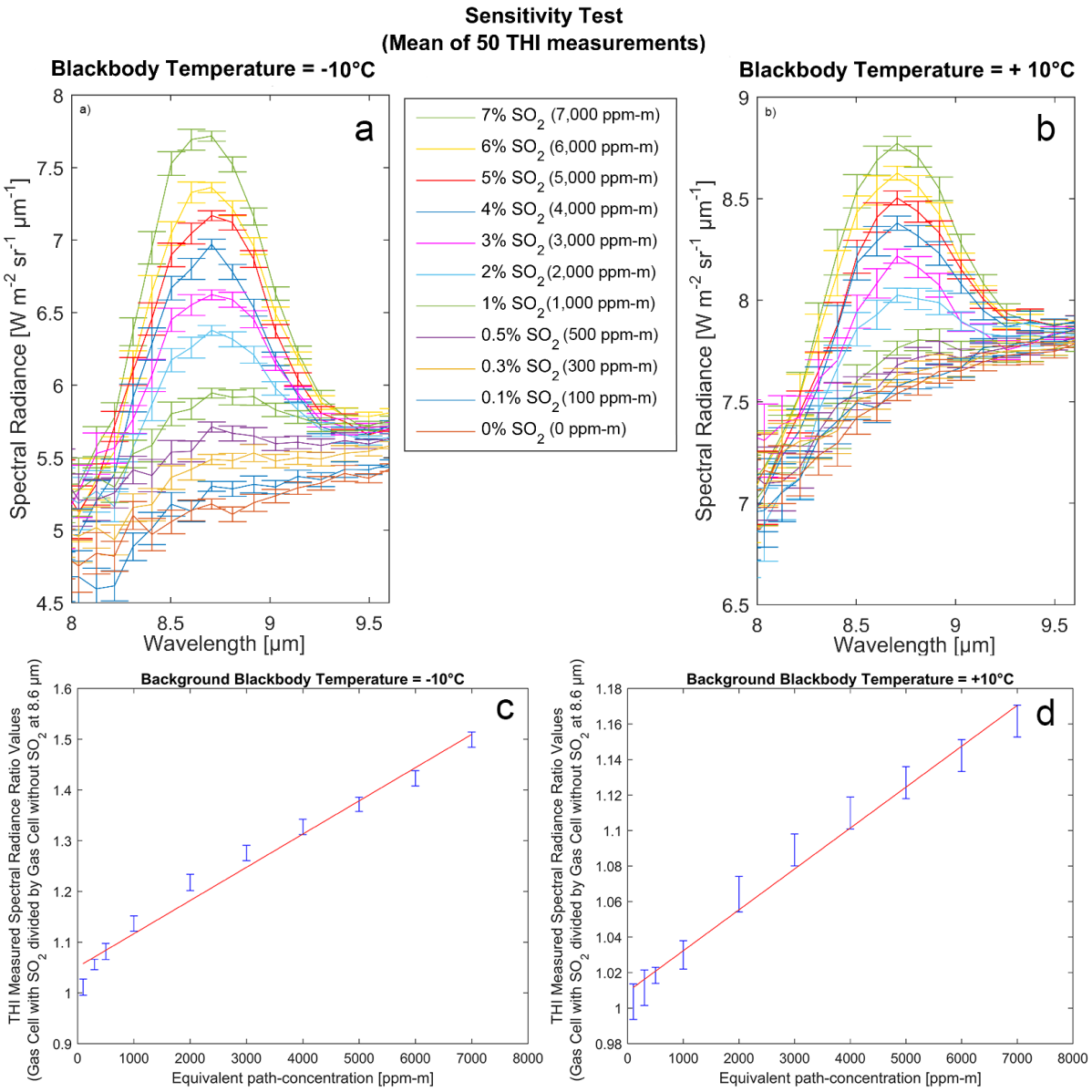

Figure 2.7. a) Average and standard deviation obtained for 50 THI measurements of a blackbody (- 10 °C) as seen through the gas cell. **b)** Average and standard deviation obtained for 50 THI measurements of a blackbody (+ 10 °C) as seen through the gas cell. The gas concentrations that were used to fill the gas cells are shown in percentage. The equivalent values in ppm·m (assuming Kīlauea-like plume widths) are also given. **c)** THI measured spectral radiance ratio (Gas cell with various concentrations of SO_2 divided by gas cell without SO_2) values obtained from Figure 2.7a. A linear interpolation was carried out for the data. **d)** THI measured spectral radiance ratio (Gas cell with various concentrations of SO_2 divided by gas cell without SO_2) values obtained from Figure 2.7b. A linear interpolation was carried out for the data. The error was estimated by using the propagation of the errors formula.

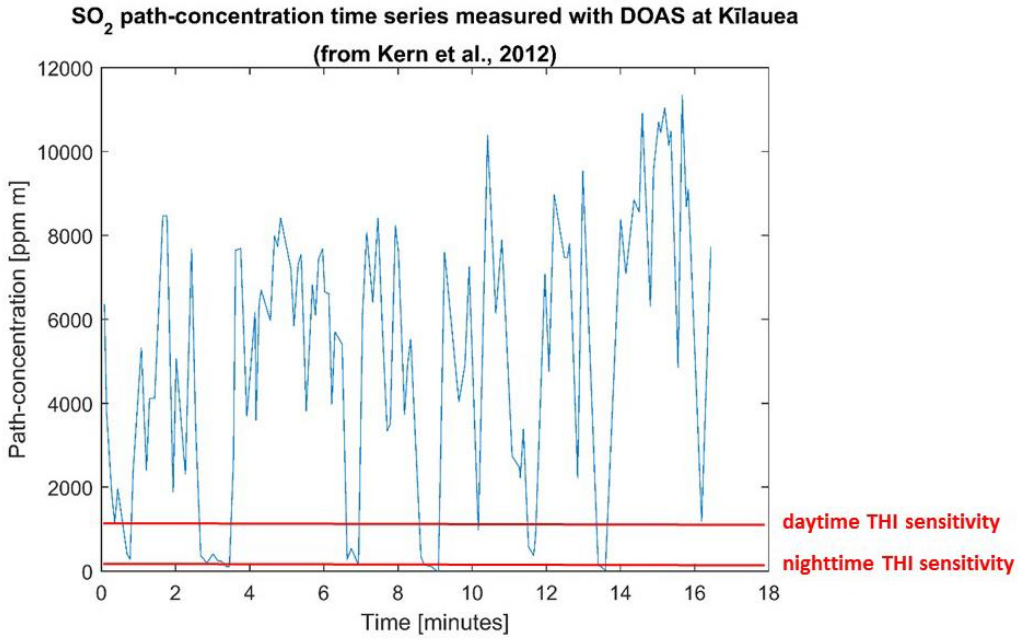

Figure 2.8. SO_2 path-concentration time series (starting on 09/28/12 at 10:20:52 am, HST,) measured with DOAS at Kīlauea volcano, Hawai'i (from Kern et al. 2012). Daytime and nighttime THI sensitivity are also reported. It appears THI would be able to resolve similar trends at basaltic volcanoes.

In order to evaluate the performance of THI for quantifying volcanic SO_2 emissions, THI measurements of TIR spectral radiances were also compared with theoretical spectral radiances computed with MODTRAN5. MODTRAN5 is a radiative transfer model developed by the US Air Force Research Laboratory, which can simulate absorption and emission in TIR for different gas concentrations and temperatures. Matlab code to control MODTRAN5 was developed as part of this project using the mod5 function developed by Derek Griffith (Matlab File Exchange 2012).

THI measurements were carried out with the background blackbody at two different temperatures, and for empty and SO_2-filled gas cells (0 %, 2 %, and 7 % at the constant temperature of + 20 °C). The THI-measured spectral radiances were compared with theoretical thermal IR spectral radiances computed with MODTRAN5 for the same optical conditions. The presence of the gas cell filled with known concentrations of SO_2 gas between the detector and the background blackbody (set at + 50 °C) were simulated in MODTRAN5 and the simplified inversion process of Equation 2.4 was employed to evaluate how well the (known) concentration of SO_2 in the gas cells could be retrieved from the resulting THI spectra. Figures 2.9a and 2.9b show a comparison between the spectral SO_2 emission and transmission curves derived from THI and from MODTRAN5 simulations (dotted lines). Measured and theoretical curves are in reasonably good agreement.

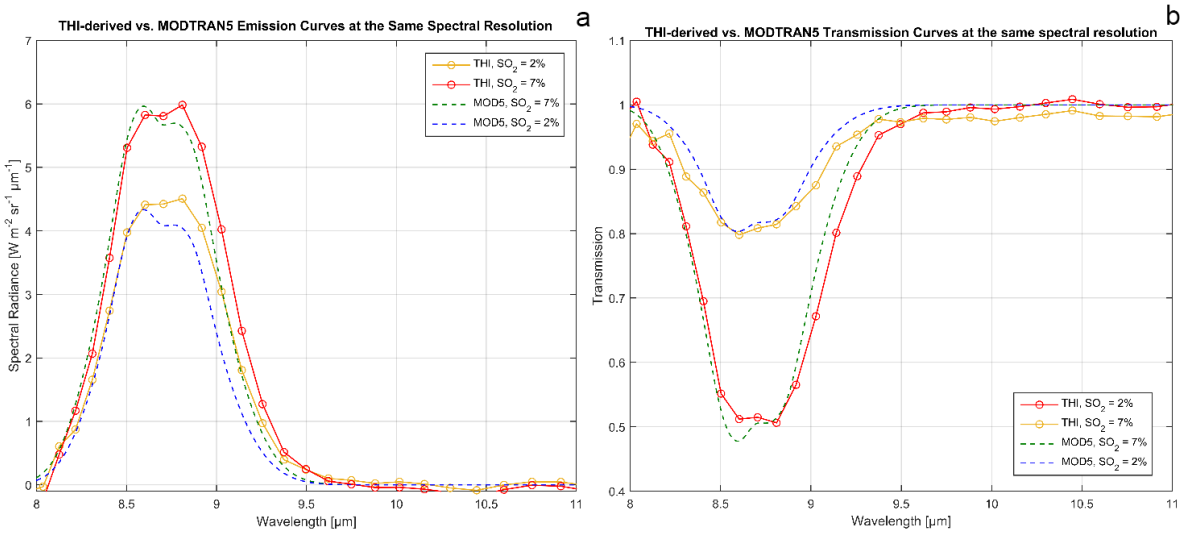

Figure 2.9. a) Comparison between the spectral SO_2 emission curves derived from the THI measurements and MODTRAN5 simulations (dotted lines) at different concentrations (2 % and 7 %). **b)** Comparison between the spectral SO_2 transmission curves derived from the THI data and MODTRAN5 simulations (dotted lines) at different concentrations (2 % and 7 %).

2.4. Initial field-testing of THI at Kīlauea volcano

The instrument was field-tested at Kīlauea volcano, Hawai'i. THI was placed near the parking lot of the Jaggar Museum in the Hawai'i Volcanoes National Park overlooking the volcanic plume rising from the Halema'uma'u vent. Measurements were collected both during daytime and nighttime in light and variable easterly trade winds conditions with clear, hazy and cloudy backgrounds (Figure 2.10).

Figure 2.10. THI scanning across the volcanic plume and quantifying SO_2 path-concentrations at the summit of Kīlauea volcano, Hawai'i, USA.

Figure 2.11 is a THI-obtained color map that shows the relative concentration of SO_2 contained in the volcanic plume derived from a simple two-channel approach. The 8.6 µm band, where the peak SO_2 spectral feature occurs, was subtracted from the 10 µm band, where the atmosphere is mostly transparent. This simple radiance difference can provide a qualitative map of the SO_2 relative path-concentration in the volcanic plume. The scan was taken on 12/8/2015 in the afternoon. The SO_2 volcanic plume vented from the Halema'uma'u vent on the summit of Kīlauea volcano can be seen rising above the caldera of the volcano and its non-homogenous structure can be observed.

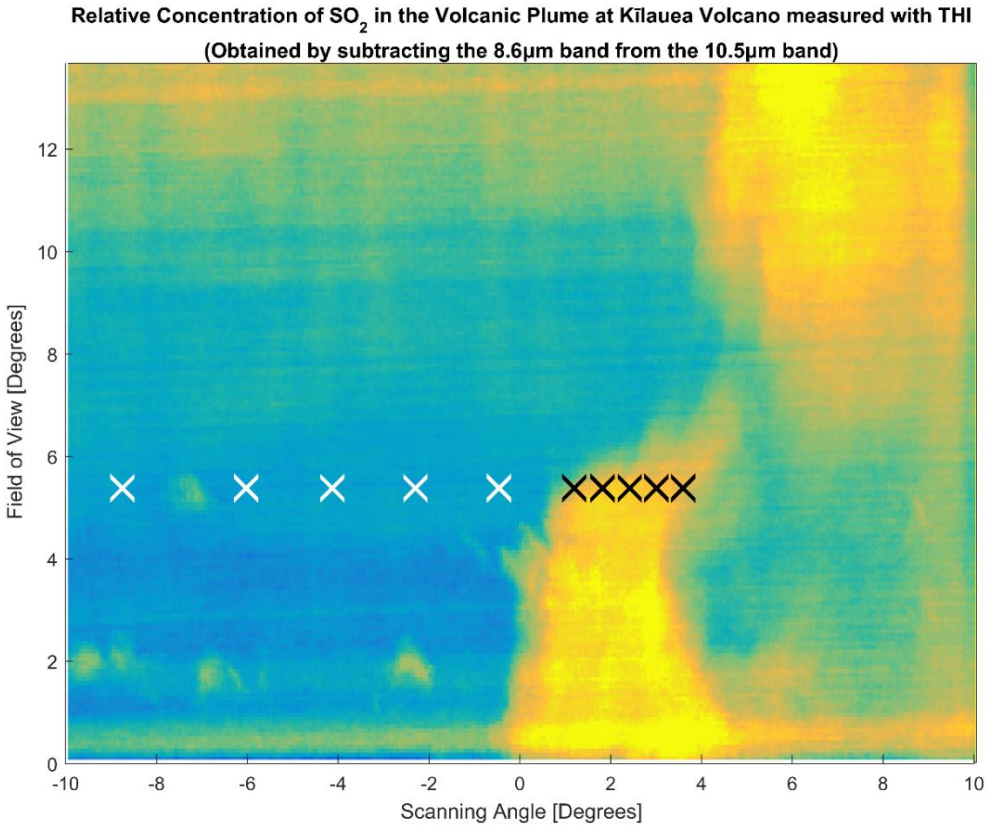

Figure 2.11. Color map showing the relative concentration of SO_2 in the volcanic plume vented from the Halema'uma'u vent on the summit of Kīlauea volcano. The white marks show locations which were selected to represent background (out of plume) conditions. The black marks indicate locations which were selected to represent SO_2 (in plume) conditions. These spectra were used for figure 2.13 calculations.

In order to carry out preliminary tests of this technique, average SO_2 path-concentrations were initially considered. In the next two chapters, each pixel will be used to obtain an individual SO_2 path-concentration and averages will no longer be used. Regions inside and outside of the plume (Figure 2.11) were selected to derive the average SO_2 path-concentration in the plume. The white marks show locations selected to represent background (out of plume) conditions. The black marks (Figure 2.11) indicate locations that were selected to represent SO_2 (in plume) conditions. The selected background and plume spectra were averaged (Figure 2.12) and the ratio (in plume divided by out of plume) was calculated to highlight the volcanic SO_2 spectral signature (Figure 2.13). Ratios within the SO_2 peak region (from 8.3 μm to 9.3 μm) are larger than 1.5 while those outside the SO_2 peak region deviate from 1 by less than 0.25. This deviation may be due to variations in background conditions, temperature, water vapor, clouds and sensor noise. A preliminary inversion algorithm was developed and MODTRAN5 was used to calculate spectral radiances in and out of the plume for viewing geometries similar to those of the measurements carried out here (Figure 2.14a). The calculations were based on an afternoon (2 pm, HST) atmospheric sounding (Figure 2.14b) obtained from Hilo (ITO) airport via the University of Wyoming's Upper Air Sounding website (Upper Air Sounding 2016). The temperature of the plume in the assessed region (black marks in Figure 2.11) was assumed to be ambient. In fact, the measurements were carried out in the region where the plume was no longer rising. During standard trade winds conditions, the plume is observed to rise for a short duration and then remain at a constant height. At that point, the plume is no longer buoyant due to entrainment of environmental air. This was also confirmed by our observations using thermal cameras wherein we observed that the plume was visible near the source and soon became invisible as it left the source. The computed spectral radiances were used to calculate a ratio for spectra in and outside the volcanic plume (in plume divided by out of

plume). These ratio calculations were compared to the measured ratio (Figure 2.13). In order to match the height of the THI-observed SO_2 ratio peak, a path concentration of 7 150 ppm-m and plume width of 500 m was used for the MODTRAN5 simulation. This SO_2 path-concentration is within the range of those reported by Grutter et al. 2008, Elias and Sutton 2012, Kern et al. 2012, and Kern et al. 2013 at the Kīlauea volcanic plume. The ratio values of 5 150 and 9 150 ppm-m are also shown (Figure 2.13).

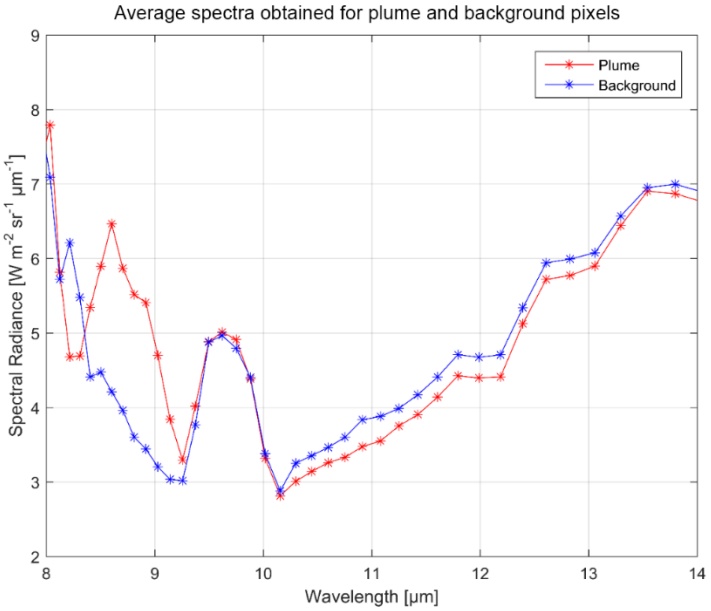

Figure 2.12. The averaged spectra obtained for background (out of plume) and plume pixels. The two averaged spectra differ significantly in the SO_2 peak region (from 8.3 µm to 9.3 µm). The peak at 9.6 µm is stratospheric ozone.

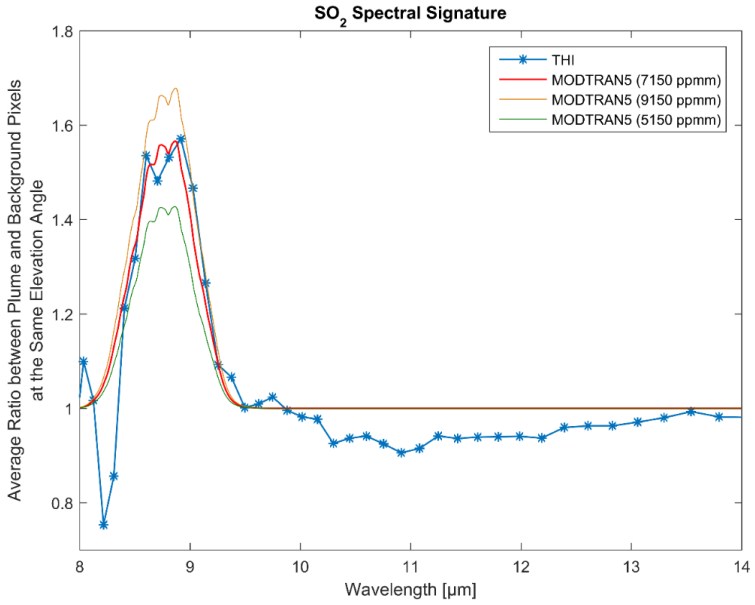

Figure 2.13. SO_2 spectral signature obtained from the average ratio of spectra derived from plume (black marks in Figure 2.9) and background pixels (white marks in Figure 2.9). The MODTRAN5-computed ratio values for 7 150 ppm-m, 5 150 ppm-m, and 9 150 ppm-m are also shown.

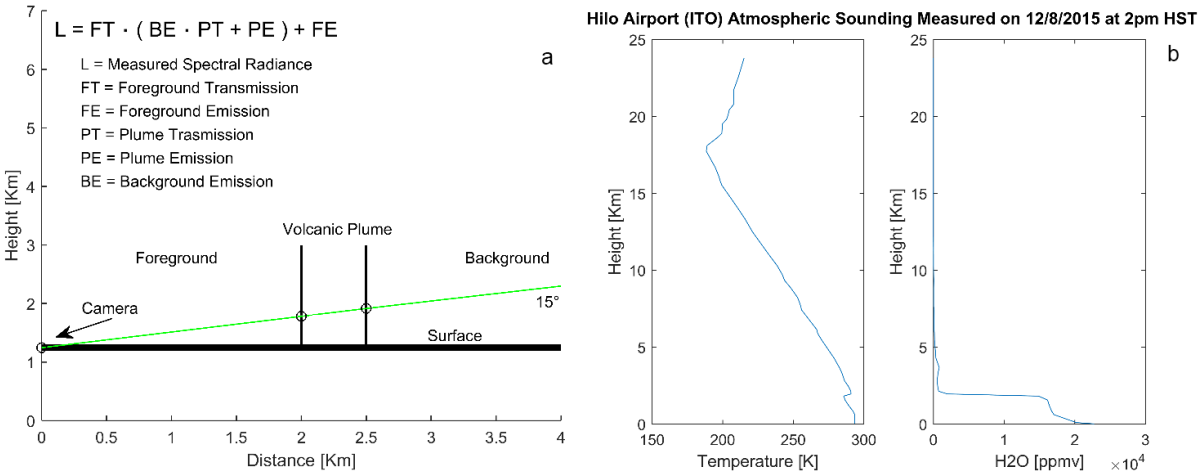

Figure 2.14. a) A sketch showing the geometry assumed to solve the radiative transfer problem via Equation 2.1 in MODTRAN5 and estimate the SO_2 path-concentration. **b)** The afternoon (2 pm, HST) atmospheric sounding obtained from HILO (ITO) airport for the day of the measurements. This sounding was used in the MODTRAN5 calculations.

2.5. Discussion and Conclusion

Thermal IR imaging offers unique advantages for measuring volcanic plume emissions during both daytime and nighttime. Spectral absorption and emission features are present in the thermal IR for many gases, including SO_2, CO_2 and H_2O and, with appropriate methods, it is possible to derive plume gas path-concentrations. This study focused on the potential for THI, a thermal IR hyperspectral imaging system, to make SO_2 volcanic plume measurements. THI employs a Sagnac interferometer and an uncooled microbolometer in rapid scanning configuration to collect hyperspectral images of volcanic plumes. Each pixel in the resulting image yields a spectrum with 50 samples between 8 µm and 14 µm. Images are spectrally and radiometrically calibrated using respectively an IR source with a narrow band filter and two blackbodies. THI measured within the spectral region from 8 µm to 14 µm, which covers a SO_2 absorption and emission band (centered at 8.6 µm). THI sensitivity to measure SO_2 was determined using gas cells filled with known concentrations of SO_2 and using NIST-traceable blackbodies to simulate a range of realistic background conditions. To confirm the robustness of the THI measurements, THI data were benchmarked against those obtained from a commercial off-the-shelf non-imaging Michelson FTIR spectrometer.

Laboratory measurements were carried out to determine how well THI could discriminate between a wider range of SO_2 concentrations. The temperature of the blackbody was set to either -10°C or $+10$°C to simulate the temperature of the sky in tropical regions during nighttime and daytime, to simulate the natural variability that would be encountered in the field. I showed that THI is able to detect SO_2 gas path-concentrations as low as 100 ppm-m with a background temperature of -10°C (i.e., somewhat ideal observation conditions, at night with a high elevation angle) and as low as 1 000 ppm-m with a background temperature of $+10$°C (i.e., much less ideal observations conditions, during the day, at low elevation angles). Additionally, theoretical thermal IR spectral radiances were computed with MODTRAN5 for the same optical conditions, to evaluate how well the (known) concentration of SO_2 is the gas cells could be retrived from the resulting THI spectra. A good agreement between THI measured and theoretical spectra under controlled conditions was shown. These laboratory studies confirm that THI would be able to resolve temporal trends in SO_2 degassing at volcanoes located in different geologic settings (Grutter et al. 2008; Elias and Sutton 2012; Kern et al. 2012 and Kern et al. 2013).

THI was also field-tested at Kīlauea volcano, Hawai‘i by imaging the volcanic plume raising from the Halema‘uma‘u vent. The hyperspectral thermal IR data cube, collected by THI, was processed using a

simplified MODTRAN5-based inversion algorithm based on measured spectral radiance ratio calculations between the averages of in plume and out of plume pixels. Spectra collected in and out of the plume were used to illustrate the SO_2 absorption-emission band. This SO_2 feature was modeled with MODTRAN5, using the same geometry and environmental conditions of the day of the measurements. A path-concentration of 7 150 ppm-m was retrieved from measurements made near the Halemaʻumaʻu vent. This SO_2 path-concentration is within the range of those reported by Grutter et al. 2008, Elias and Sutton 2012, Kern et al. 2012, and Kern et al. 2013 at the Kīlauea volcanic plume.

The exploratory study carried out here suggests that thermal IR hyperspectral imaging can be successfully employed to image volcanic plumes and derive SO_2 path concentrations, which in turn can be converted into mass flux. In fact, each pixel yields a path-concentration of SO_2. Summing each line in the x-dimension of the image and then multiplying by the plume velocity in the y-dimension (obtained from the image itself) yields the SO_2 mass flux. The fact that the plume rises while the camera is scanning is an issue if the plume has strong heterogeneities in temperature and SO_2 abundance, and if the plume is rising fast compared with the scanning rate of the camera. This temporal "blurring" issue is also common to other techniques such as COSPEC, DOAS, scanning DOAS, and Prata's IR camera technique (Moffat and Millan 1971; Mori and Burton, 2006 and Prata and Bernardo 2014). For the measurements carried out here, a complete scan of the plume was carried out in approximately one second. This time is short relative to plume motion occurring kilometers away. The fact that both the plume and background temperatures affect the thermal IR spectral radiances requires an inversion algorithm to be employed. Chapter 3 is going to deal with such inversion algorithm.

CHAPTER 3

VALIDATING THE ACCURACY OF SO_2 GAS RETRIEVALS IN THE THERMAL INFRARED (8-14 MICRON)

Published as: Gabrieli, A., Porter, J.N., Wright, R., Lucey, P.G. (2017). Validating the accuracy of SO_2 gas retrievals in the thermal infrared (8–14 μm). Bulletin of Volcanology, doi: 10.1007/s00445-017-1163-3

Abstract — Quantifying sulfur dioxide (SO_2) in volcanic plumes is important for eruption predictions and public health. Ground-based remote sensing of plumes contains spectral radiance information on the path-concentration of SO_2. However, reliable inversion algorithms are needed to convert plume spectral radiance measurements into SO_2 path-concentrations. Various techniques have been used for this purpose. Recent approaches have employed Thermal InfraRed (TIR) imaging between 8 μm and 14 μm to provide two-dimensional mapping of plume SO_2 path-concentration, using what might be described as "dual-view" techniques. In this approach, the radiance (or its surrogate brightness temperature) is computed for portions of the image that correspond to the plume and compared with spectral radiance obtained for adjacent regions of the image that do not (i.e., "clear sky"). In this way, the contribution that the plume makes to the measured radiance can be isolated from the background atmospheric contribution: this residual signal is then converted into an estimate of gas path-concentration via radiative transfer modelling. These dual-view approaches suffer from several issues, mainly the assumption of clear sky background conditions. At this time, the various inversion algorithms remain poorly validated. This paper makes two contributions. Firstly, it validates the aforementioned dual-view approaches, using hyperspectral TIR imaging data. Secondly, it introduces a new method to derive SO_2 path-concentrations, which allows for single point SO_2 path-concentration retrievals, suitable for hyperspectral imaging with clear or cloudy background conditions. The SO_2Amenable Lookup Table Algorithm (SO_2–ALTA) uses the MODTRAN5 radiative transfer model to compute radiance for a variety (millions) of plume and atmospheric conditions. Rather than searching this lookup table to find the best fit for each measured spectrum, the lookup table was used to train a Partial Least Square Regression (PLSR) model. The coefficients of this model are used to invert measured radiance spectra to path-concentration on a pixel-by-pixel basis. In order to validate the algorithms, TIR hyperspectral measurements were carried out by measuring sky radiance when looking through gas cells filled with known amounts of SO_2. SO_2–ALTA was also tested on retrieving SO_2 path-concentrations from the Kīlauea volcano, Hawai'i. For cloud free conditions, all three techniques worked well. In cases where background clouds were present, then only SO_2–ALTA was found to provide good results, but only under low atmospheric water vapor column amounts.

3.1. Introduction

Detecting volcanic emissions of SO_2, and related acidic sulfate aerosols, is important for volcanic eruption prediction and public health (EPA 2011). SO_2 reacts chemically with sunlight, dust particles, oxygen and water to form sulfate aerosols, which can threaten public health, be harmful to animals and plants, and damaging to infrastructures (e.g., Baxter 1999; Schmidt 2014; Zuccaro et al. 2014). Volcanic degassing also provides information on magma supply within a volcanic system (e.g., Aiuppa et al. 2007; Anderson and Segall 2013; Gabrieli et al. 2015), eruption rates (Allard et al. 1994), and, hence, mass balance (e.g., Allard et al. 2014). For these reasons, it is important to measure gaseous emissions from volcanic plumes.

Classically, SO_2 path-concentrations have been measured using passive spectroscopic approaches. Various sensors have been used to perform point measurements and quantify volcanic SO_2 by measuring its absorption features in the UltraViolet (UV) part of the electromagnetic spectrum (e.g., Moffat and Millan 1971; Stoiber and Jepsen 1973; Stoiber et al. 1983). UV imaging has recently been performed at active volcanoes (e.g., Bluth et al. 2007; Mori and Burton 2009; Kern et al. 2013). Such imaging can provide valuable synoptic views of the spatial distributions of SO_2 from which fluxes can be derived (e.g., Bluth et al. 2007). A limitation, however, is that these UV techniques, both imaging and non-imaging, can only be used for SO_2 retrievals and only work during the daytime, not at night. Open-path Fourier Transform InfraRed (FTIR) spectroscopy can be employed for retrieving various gas path-concentrations (SO_2, CO_2, H_2O, and SiF_4) both during the day and night (Love et al. 1998; Francis et al. 1998; Oppenheimer et al. 1998; Goff et al. 2001; Oppenheimer et al. 2006; La Spina et al. 2015). Despite the high spectral resolution and the possibility of multiple gas retrievals, FTIR is still mostly based on point measurements. Recently, both low spectral resolution and hyperspectral thermal imaging techniques have been developed, respectively by Prata and Bernardo (2014) and by Gabrieli et al. (2016).

Ground-based Thermal InfraRed (TIR) remote sensing retrievals of SO_2 path-concentrations are complicated by the fact that both emission and absorption occur from and within the plume, the background, and the foreground atmosphere (Collins et al. 2001). For these reasons, environmental conditions strongly affect TIR SO_2 gas retrievals, making the retrieval process complex (Realmuto and Worden 2000, Prata and Bernardo 2014). In short, the TIR spectral radiance measured by an imaging system is the convolution of 1) the spectral radiance emitted by the atmosphere behind the plume, 2) the portion of this which is transmitted through the plume (i.e., not absorbed by gases in the plume including, but not limited to, SO_2), 3) the spectral radiance emitted by the plume itself by virtue of its temperature and its emissivity, and 4) how this plume radiance is then attenuated by the atmosphere that lies between the plume and the sensor; this atmosphere also emits spectral radiance to the sensor. Radiative transfer modelling can then be used to convert the measured spectral radiance to an estimate of gas path-concentration for each pixel in the image. Thus, there are many sources of potential uncertainty in SO_2 retrieval procedures, so that error is usually quite significant, typically being plus or minus 20% (e.g., Prata and Bernardo 2014). Hence careful validation is required and uncertainties have to be assessed, as approaches are in continual need of refinement and update as technology and capability develop. This is the aim of this paper.

3.1.1 The dual view approach

Recent approaches have employed TIR imaging between 8 μm and 14 μm to provide two-dimensional mapping of plume SO_2 path-concentration, using what might be described as "dual-view" techniques. In this case, measured radiance or its surrogate brightness temperature are computed for portions of the image that correspond to the plume and compared with spectral radiance obtained for adjacent regions of the image that do not (i.e., "clear sky"). In this way, the contribution that the plume makes to the measured radiance can be isolated from the background atmospheric contribution: this residual signal being converted to an estimate of gas path-concentration via radiative transfer modelling.

Prata and Bernardo (2014) developed a dual-view algorithm to retrieve SO_2 path concentrations. Their approach employs brightness temperature differences, from the plume and the background, at three TIR wavelengths (8.6 μm, 10 μm, and 12 μm) which are incorporated into a modified Schwarzchild radiative transfer equation. Prata and Bernardo selected the three wavelengths to account for the SO_2 absorption/emission feature at 8.6 μm, the temperature of the plume, the atmospheric background, and instrumental effects. Their method has been tested at various volcanoes and at industrial sites under clear sky conditions. Meteoric clouds were flagged as bad data points. Gabrieli et al. (2016) also implemented a dual-view SO_2 retrieval approach using radiance measurements from the plume and the background. Their approach employs radiance differences, from the plume and the background at ~50 spectral measurements between 8 μm and 14 μm, carried out with a TIR hyperspectral imaging sensor. To derive SO_2 path concentrations, MODTRAN5 was run iteratively, for different plume conditions, to obtain the best fit between the spectral radiance measurements and the MODTRAN5 simulations. MODTRAN5 was selected for this purpose because it is one of the most frequently employed and well validated atmospheric modeling codes (Berk et al. 2008; Cramer et al. 2015). Gabrieli et al. (2016) tested this dual-view approach by deriving SO_2 path-concentrations in the volcanic plume rising from the Halema‘uma‘u crater on the summit of Kīlauea volcano, Hawai‘i. Only cloud free conditions were tested. While the Prata and Bernardo (2014) and the Gabrieli et al. (2016) are implemented differently, the fact that they both use dual-view measurements suggest that they will perform similarly.

Dual view approaches are limited by the presence of meteoric clouds and atmospheric absorption and emission between the sensor and the plume. The process of comparing regions in and out of the plume assumes the background sky is homogeneous. In Prata and Bernardo (2014), clouds were flagged as bad data points. In Gabrieli et al., (2016), the dual-view approach was only tested under clear sky conditions. Unfortunately, sub-visual cirrus clouds, which are defined as those cloudy layers whose optical thickness is less than 0.3, are often present and difficult to detect (Sun et al. 2011). An additional problem with dual-view approaches is the fact that they do not properly account for the effect that the foreground atmosphere (between the plume and the sensor) has on the SO_2 emission/absorption spectral feature at 8.6 μm. At this time, the dual-view approach, as implemented by both Gabrieli et al. (2016) and by Prata and Bernardo (2014), remain poorly validated.

The aims of this chapter are twofold. Firstly, we validate the accuracy and precision of the aforementioned dual-view approaches under ideal (clear sky) conditions, using gas cells containing known amounts of SO_2 and under non-ideal (cloudy sky) conditions. Secondly, we present an alternative approach for SO_2 retrievals from hyperspectral TIR image data that estimates SO_2 path-concentrations on a pixel-by-pixel basis, and demonstrate the performance of that new approach under ideal and non-ideal observation conditions.

3.2. The THI instrument

The Thermal Hyperspectral Imager (THI) (Wright et al. 2013; Gabrieli et al. 2016) was used for this validation study. THI consists of a Sagnac interferometer and an uncooled microbolometer (a FLIR Photon 320) in rapid scanning configuration to collect hyperspectral images (Lucey et al. 2008). THI is capable of acquiring moderate spectral resolution images (40 cm^{-1}) from which SO_2 emission and absorption spectra can be retrieved. A spectrum containing 50 samples between 8 μm and 14 μm is available at each pixel in the resulting image cube. Images are radiometrically calibrated using two blackbodies at 20 °C and 70 °C and spectrally calibrated with an IR lamp with a 9.75 μm narrow band filter (Gabrieli et al. 2016).

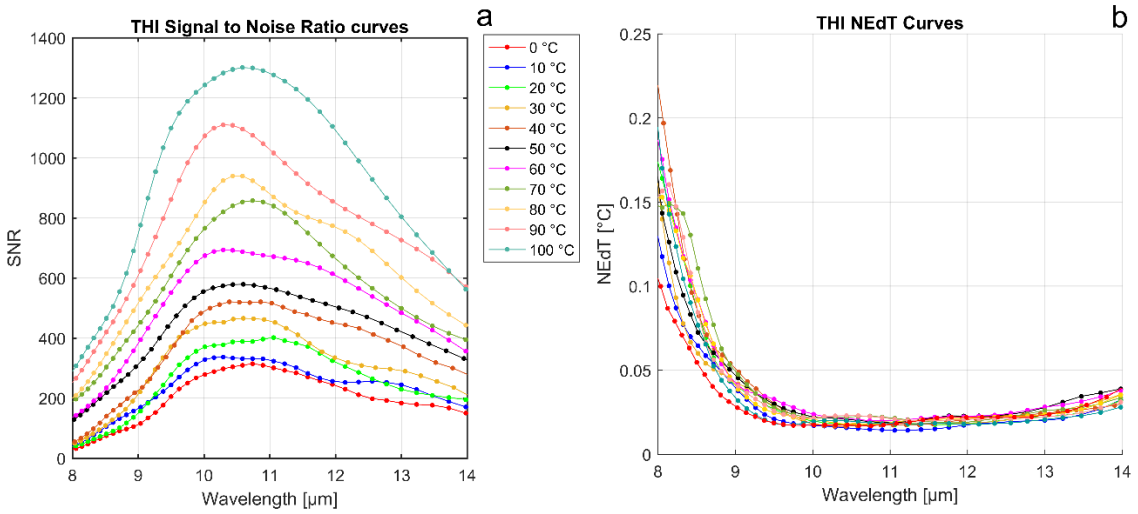

Figure 3.1. (a) Signal-to-noise ratio curves of the THI instrument for various background temperatures. **(b)** The NEdT curves of the THI instrument for various background temperatures.

The THI sensitivity in detecting SO_2 was determined using gas cells filled with known concentrations of SO_2 and using National Institute of Standards and Technology (NIST)-traceable blackbodies. Gabrieli et al. (2016) showed that, under ideal observation conditions, at night with a high elevation angle and strong temperature contrast between the temperature of the background and the gas, THI can detect SO_2 gas path-concentrations as low as 100 ppm-m. Figure 3.1 summarizes the sensitivity of the THI instrument. Figure 3.1a shows the signal-to-noise ratio (SNR) performance of THI, obtained for various blackbody temperatures. Figure 3.1b shows the noise-equivalent temperature difference (NEdT) of the spectral channels, a fundamental measure of the quality of the measurements. The THI signal-to-noise ratio curves range from 200 to 1 300 for temperatures between 0 °C and 100 °C. The instrument has relatively flat signal-to-noise ratios between 10 µm and 12 µm and that the NEdT curves are about 0.025 °C at the same wavelengths. The signal-to-noise ratios and the NEdT curves respectively decrease and increase significantly towards 8 and 14 µm due to the performance of the microbolometer camera.

3.3. Validation test

To validate the performance of the dual-view approaches, it was necessary to simulate measurements that would be carried out for a volcanic plume seen against the background sky. THI measurements of sky radiance were collected using gas cells filled with known SO_2 gas concentrations to replicate a volcanic plume. The gas cells were 10 cm in length and equipped with IR transparent zinc-selenide windows. The distance between the aperture of THI and the gas cell was set to 19.05 cm. Gas concentrations were chosen such that, when combined with the 10 cm length of the cell, they contained volcanically realistic SO_2 path concentrations (in ppm-m). The gas cells were filled with gas concentrations equivalent to 0 ppm-m, 1 000 ppm-m, 2 000 ppm-m, 3 000 ppm-m, 4 000 ppm-m, 5 000 ppm-m, 6 000 ppm-m and 7 000 ppm-m, representative of volcanic plumes (Kern et al. 2012; Kern et al. 2013). The gas temperature was kept constant at +20 °C.

The experiments were conducted under different atmospheric conditions where the Gabrieli et al. (2016) method was tested for a clear sky (ideal) background and completely cloudy (non-ideal) background. Although the Prata and Bernardo (2014) and the Gabrieli et al. (2016) algorithms are implemented differently, they both use dual-view measurements. This suggests that their performance will be similar under non-ideal conditions. Therefore, the cloud test carried out for Gabrieli et al. (2016) is also representative of the Prata and Bernardo (2014) approach. Figure 3.2 shows the experimental setup with THI and the SO_2 gas cells. Figure 3.2a shows THI acquiring images of clear sky when viewed through the SO_2 gas cell on 07/12/2016. Figure 3.2b shows THI acquiring images of a background composed of primarily altostratus clouds and also patches of blue sky on 05/17/2016, 2016. Figures 3.2c, 3.2d, and 3.2e are raw THI images of the sky as seen through the SO_2 gas cell. They were obtained by subtracting the 8.6 µm channel from the 10 µm channel.

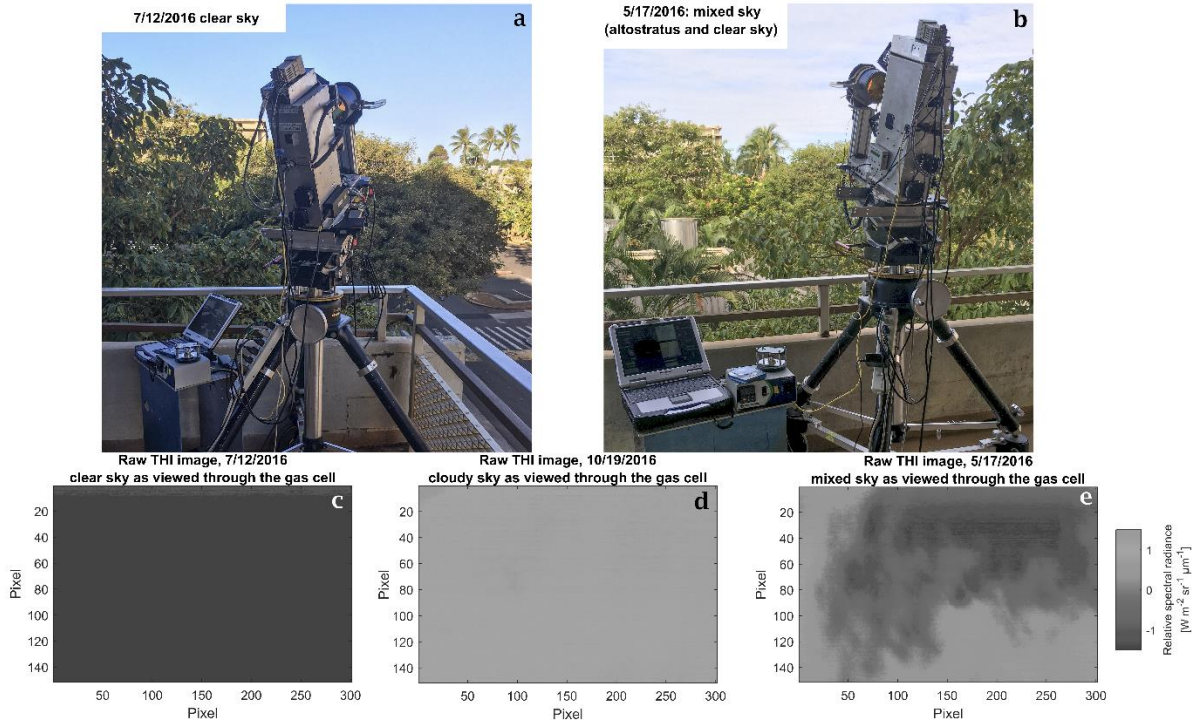

Figure 3.2. (a) THI acquiring images of clear sky when viewed through the SO_2 gas cell on 07/12/2016. **(b)** THI acquiring images of a background composed of primarily altostratus clouds and also patches of blue sky on 05/17/2016. **(c)-(e)** Un-processed (raw) THI images of sky radiance obtained, when looking through the gas cell, by subtracting the 8.6 μm channel from the 10 μm channel. **(c)** Raw THI image of clear sky obtained on 07/12/2016. **(d)** Raw THI image of overcast sky obtained on 10/19/2016. **(e)** Raw THI image of a mixture of cloud free and cloudy sky obtained on 05/17/2016.

Measurements were collected at elevation angles of 20 °, 30 °, and 40 °. The field of view of THI is approximately 10 ° and this was accounted for when applying the inversion algorithms. Clear sky THI measurements were obtained over three mornings between 07/10 and 07/12/2016. Measurements of cloudy sky (altostratus and cumulus clouds) with high humidity conditions were acquired on 10/19/2016, in the early morning. Measurements of both clouds (cumulus clouds and altostratus) and clear sky were obtained on 05/17/2016.

For this study, the two inversion algorithms were modified to account for the gas cell configuration and the gas cells were kept at constant temperature of 20 °C. The data were processed using the two dual-view inversion techniques: Gabrieli et al., (2016) and Prata and Bernardo (2014). In this way, the performance of the two approaches was compared, and their precision and accuracy were evaluated (i.e., how accurately and precisely do they report the path-concentration of SO_2 present in the gas cells?)

3.4. Testing SO_2 plume inversions: dual-view approaches

3.4.1. Clear Sky Conditions

For the Gabrieli et al. (2016) approach, difference spectra between gas-filled cells and air-filled cells were obtained for each pixel in the images acquired under clear sky conditions. MODTRAN5 was then used to invert these spectra to path-concentrations, assuming the viewing geometries of the measurements carried out here. Rather than using one of the Standard Atmospheres available in MODTRAN5, local Hawai'i atmospheric soundings for the days of the measurements were used via the University of Wyoming's Upper Air Sounding website (Upper Air Sounding, 2016). For the Prata and Bernardo (2014) analysis, brightness temperature differences at three wavelengths (8.6 μm, 10 μm, and 12 μm) were used to characterize the plume temperature, the atmospheric background, and the SO_2 path-concentrations (Prata and Bernardo 2014).

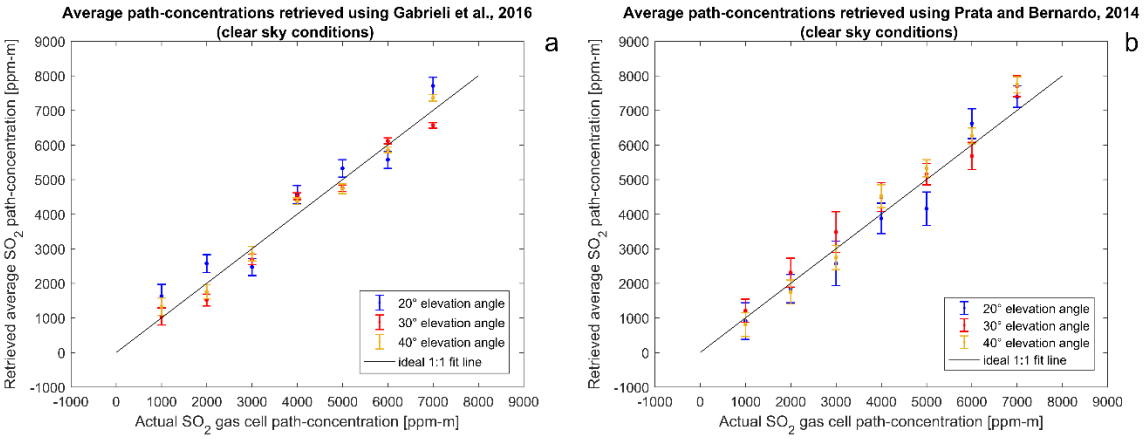

Figure 3.3. (a) Average path-concentrations retrieved using the Gabrieli et al. (2016) approach under clear sky background conditions at various elevation angles. **(b)** Average path-concentrations retrieved using the Prata and Bernardo (2014) approach under the same conditions. The values were obtained by averaging the retrieved SO_2 at each pixel for each THI image. Standard deviation bars are displayed as well as an ideal 1:1 black fit line. Ideally, the data points should fall on the black line.

Figure 3.3 shows the average path-concentrations retrieved using the Gabrieli et al. (2016) and the Prata and Bernardo (2014) approaches under clear sky conditions at different elevation angles. The values were obtained by averaging the retrieved SO_2 at each pixel for each THI image. Both approaches were found to perform well under clear sky conditions. The coefficients of determination (R-squared) are 0.9924 and 0.9902, respectively for the Gabrieli et al. (2016) and the Prata and Bernardo (2014) techniques.

3.4.2. Fully Cloudy Conditions

The Gabrieli et al. (2016) approach was used to process the images. The cloud test carried out here is representative of both the Gabrieli et al. (2016) and the Prata and Bernardo (2014) approaches. Very low temperature contrast between the temperature of the sky and the temperature of the gas was observed, under cloudy conditions, and the algorithm performed very poorly at all of the elevation angles. Figure 3.4 shows the average path-concentrations retrieved using the Gabrieli et al. (2016) approach under cloudy conditions at a 40° elevation angle. The values were obtained by averaging the retrieved SO_2 at each pixel for each THI image. It appears that the inversion algorithm developed by Gabrieli et al. (2016) performs very poorly when trying to retrieve SO_2 path-concentrations under cloudy background conditions. This cloud test illustrates how a dual-view inversion algorithm, which was designed for clear sky conditions, performs with a non-ideal cloudy background. This test suggests that dual view approaches cannot be employed under cloudy background conditions.

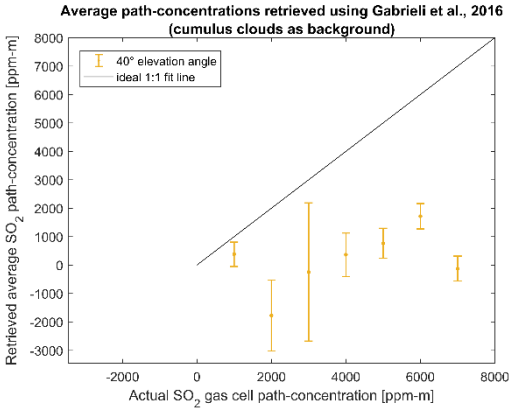

Figure 3.4. Average path-concentrations retrieved using the Gabrieli et al. (2016) approach under cloudy background conditions at various elevation angles. The values were obtained by averaging the retrieved SO_2 at each pixel for each THI image. Standard deviation bars are displayed as well as an ideal 1:1 black fit line. Ideally, the data points should fall on the black line.

3.5. Validation of dual-view approaches: summary

The two dual-view approaches implemented by Gabrieli et al. (2016) and Prata and Bernardo (2014) were tested using TIR measurements when looking through SO_2 gas cells, filled with known concentrations of SO_2. The Gabrieli et al. (2016) and the Prata and Bernardo (2014) approaches were used to retrieve the known path-concentrations in the cells. Both clear and cloudy background conditions were tested.

Both approaches performed well in clear sky conditions if the distance to the plume (i.e., the gas cell, in this case) is known. Prata and Bernardo (2014) assume errors of 20% when using their approach. This was confirmed by the study carried out here. The Gabrieli et al. (2016) approach was more precise, but less accurate in retrieving the known SO_2 path-concentrations than the Prata and Bernardo (2014) inversion procedure. The retrieved averaged SO_2 path-concentrations using Prata and Bernardo's approach were 10-20% closer to the actual SO_2 gas cell concentration than Gabrieli et al.'s method. However, the uncertainties were 50-60% larger than those obtained using Gabrieli et al.'s approach. When clouds were present in the background, then dual-view approaches did not work.

This validation study showed that dual-view approaches (Gabrieli et al. 2016 and Prata and Bernardo 2014) can successfully be employed for SO_2 path-concentration retrievals under clear sky conditions. However, cloudy backgrounds drastically reduce performance and unfortunately, sub-visual cirrus clouds are difficult to detect, but often present.

3.6. Single point SO_2 inversion algorithms: SO_2–ALTA.

It would be ideal to have an SO_2 retrieval algorithm that is accurate for both the presence of both clear and cloudy backgrounds. To meet this goal, a new approach was developed. The SO_2 Amenable Lookup Table Algorithm (SO_2–ALTA) consists of a new SO_2 gas retrieval algorithm. SO_2–ALTA is designed for observations carried out at a single point with cloud free or cloudy backgrounds. SO_2–ALTA is written in Matlab and uses a Matlab Class Wrapper (Mod5.m), developed by Derek Griffith (Matlab File Exchange 2012), to call MODTRAN5.

SO_2–ALTA uses a library of calculated spectra, which were obtained using MODTRAN5 (version 5.3.2, Anderson et al. 2009) for a variety of plume and viewing conditions, as reported in Table 3.1. Conceptually, the TIR spectral radiance retrieved from any given image of a volcanic plume is a unique function of the composition and state of the plume (which we are interested in) and the background (which we are not). MODTRAN5 allows us to model this complexity and predict at-sensor spectral radiance for, theoretically, all possible plume/background and composition/state combinations. We vary SO_2 plume gas concentrations, plume locations, plume sizes, viewing geometries, in an attempt to simulate atmospheric conditions that occur at the summit of Kīlauea volcano, in Hawai'i, and in analogous tropical volcanic scenarios.

To simulate atmospheric variability, it was necessary to include a reasonable number of measured atmospheric soundings with different water vapor column abundances. Water vapor is the main atmospheric trace gas that can affect SO_2 gas retrievals because it is highly variable (Prata and Bernardo 2014; Realmuto and Worden 2000). Long time-series data analysis has revealed that precipitable water vapor in tropical areas ranges between 10 and 50 mm and that it is log-normally distributed around the peak value of about 30 mm (Foster et al. 2006). We found that 400 daily soundings from three tropical locations (Hilo and Līh'ue, in Hawai'i, and San Juan, in Puerto Rico), and obtained from the University of Wyoming's Upper Air Sounding website (Upper Air Sounding 2016), produced the same log-normal precipitable water vapor distribution observed by Foster et al. (2006) and can therefore, explain most of this variability (see Figure 3.5).

Table 3.1. Conditions used to develop the lookup table used to develop SO_2-ALTA

Environmental and geometrical parameters	Values used to train SO_2-ALTA
SO_2 Concentrations	0, 1, 3, 5, 7, 9, 11, 13, 15, and 17 ppm-v
Temperature and Humidity Profile	Standard tropical atmosphere and 400 daily soundings from 3 tropical locations. (365 soundings from Hilo and Līhʻue, Hawaiʻi, and 35 from San Juan, Puerto Rico. Only daytime soundings were used for Hilo).
Viewing Elevation Angles	5, 10, 20, 30, 40, 50, 60, 70, 80 and 89 °
Camera Height	0, 0.5, 1 km
Plume-Ambient Temperature Difference	0, 5, 10 °C
Plume-Camera Distances	0, 0.5, 1, 2, 5 km
Plume Widths	0.1, 0.3, 0.5, 1 km
Plume Base Height (above ground)	0 km
Plume Top Height	2.5 km
Clouds Types	Cumulus cloud layer: base 0.66 km, top 3.0 km Altostratus cloud layer: base 2.4 km, top 3.0 km. MODTRAN5 standard cirrus and sub-visual cirrus clouds
Horizontal cloud sizes	0.001, 0.005, 0.01, 0.02, 0.03, 0.07, 0.1, 0.3, 0.5, 1 km
Cloud-Camera Distances	0.25, 0.5, 0.75, 1, 2, 5 km (not applicable to cirrus clouds)

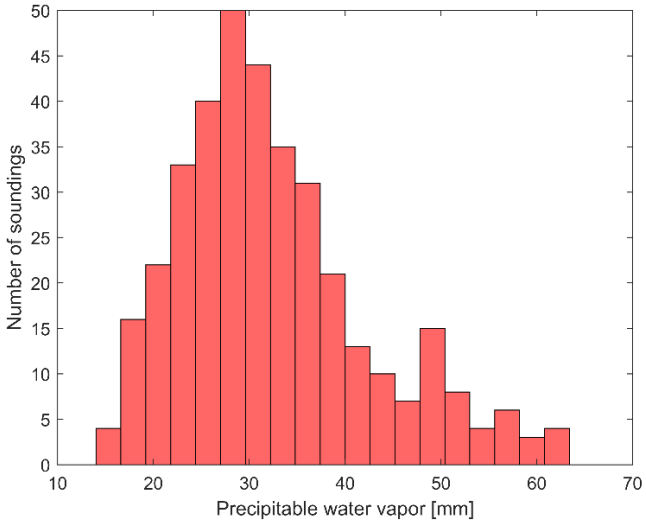

Figure 3.5. Histogram of the log-normal distribution of the precipitable water vapor for 400 daily soundings from 3 tropical locations (Līhʻue and Hilo, in Hawaiʻi, and San Juan, in Puerto Rico). The selected soundings were obtained in the months of January, March, April, July, and September of 2015 and in the months of June, August, September, and November of 2016 from the University of Wyoming's Upper Air Sounding website (Upper Air Sounding 2016)

We generated 10 800 000 spectra for each elevation angle with clear, fully cloudy, and partially cloudy conditions, each associated with a known SO_2 path-concentration. An individual THI TIR spectrum could be taken and matched against the best fit spectrum in the SO_2–ALTA library (or Look Up Table, LUT) by brute force methods to invert spectral radiance to SO_2 path-concentration. However, this is time consuming and computationally intensive, especially in field situations or where information has to be derived rapidly. Rather than using the LUT of spectra to convert radiance to path-concentration, the table was thus used to train a Partial Least Squared Regression (PLSR) model. PLSR is a powerful and amenable statistical tool, which predicts outputs (here, SO_2 path-concentrations) based on many input variables (here, spectral radiances between 8 and 14 μm), where the inputs and outputs can be redundant, collinear and/or not independent (Hoskuldsson 1988; Martens and Naes 1989; Mattu et al. 2000; Rosipal and Kramer 2006; Hecker et al. 2012; Lopez et al. 2013). PLSR selects the best weight for each of the wavelengths based on the input for finding the output. It also allows for a fast and

efficient way to implement the SO_2 inversion, without employing time-consuming curve matching algorithms iteratively.

The PLSR training of SO_2-ALTA is carried out by mapping and associating each spectrum in the MODTRAN5-generated look-up table with the corresponding SO_2 path-concentration, which would be retrieved from such a spectrum at each of the environmental and viewing conditions reported in table 3.1. We define m as the number of radiances for each wavelength, n as the individual case, and p as the SO_2 path-concentration. Assuming X is a $m \times n$ input matrix of MODTRAN5-simulated spectra and Y is a $n \times p$ output matrix of the SO_2 concentrations that would be obtained from each of the spectra in X, the model is created by finding relationships between X and Y by modelling the covariance structures in X and Y. This is carried out by finding the multidimensional direction in the input X, which can explain the maximum multidimensional variance in the output Y (Abdi 2010). The general equations governing PLSR models can be written as:

$$X = TP' + E \tag{3.1}$$

$$Y = UQ' + F \tag{3.2}$$

where T and U are the $n \times l$ matrices that are the X score component and the projection of Y, respectively. P and Q are $m \times l$ and $p \times l$ orthogonal matrices, where l is the number of components, and E and F are the error terms. The PLSR model makes the decomposition of X and Y so that it maximizes the covariance between the X score component and the projection of Y. The result is a set of coefficients (T, P', U, Q') which relate the input (X, which, in our case, is the measured spectral radiance) to the desired output (Y, which, for us, is the SO_2 path-concentration). In developing the model (and arriving at the coefficients) care is needed when selecting the number of PLSR components in order to obtain the best possible model while avoiding over-training it (this is equivalent to fitting the noise in the training dataset) (Yang et al. 2003). Once the SO_2-ALTA model is created from the known X and Y training datasets, it can be used to find unknown SO_2 path-concentrations YY from measured spectra XX.

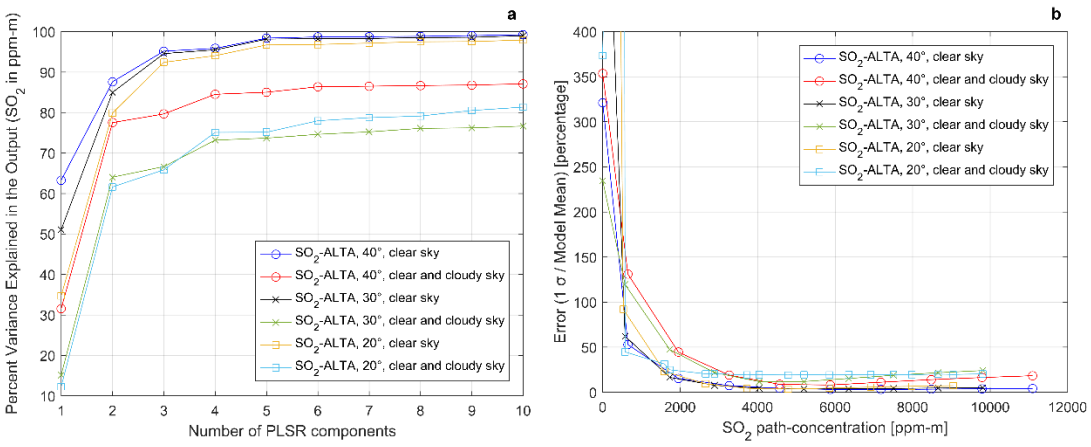

Figure 3.6. (a) Percent variance explained by six SO_2-ALTAs for a viewing angle of 20°, 30°, and 40° for both clear and cloudy sky. The number of components used to train the model was not set to greater than five in order to avoid over training the model with noise. **(b)** Error (1 standard deviation divided by the model mean) on the same six SO_2-ALTAs. For SO_2 path-concentrations higher than 3 000 ppm-m, the error is lower than 20%.

Figure 3.6 shows an example of the performance of six SO_2-ALTAs, trained for the conditions reported in Table 3.1 at the elevation angles of 20°, 30°, and 40° for both clear sky conditions and cloudy background. The models created for clouds contain also clear sky spectra to account for partly cloudy background conditions. Figure 3.6a shows the percent variance that is explained by the models in the

output *Y*, which is the SO_2 path-concentration. It can be seen that five PLSR components explains 95% of the variance in the output for clear sky conditions at 20°, 30°, and 40° elevation angles. For a cloudy background, five PLSR components explain 85% of the variance at 40° elevation angle, and 75% at 30° and 20°. If more PLSR components were used, the algorithm performed poorly in each of the cases. The number of components used to train the model was therefore not set to greater than five to avoid over training the model with noise. Figure 3.6b shows the percent error on the SO_2-ALTA models, where the error decreases rapidly with increased SO_2 path-concentration. It can also be seen that for SO_2 path-concentrations greater than 3 000 ppm-m, the error is less than 20%. Other elevation angles, which were not used during the validation study discussed below, were tested and similar results were obtained.

3.6.1. Validation of the SO_2–ALTA

A validation study of the new SO_2–ALTA was carried out using the same image data that were used to test the two dual-view approaches implemented by Gabrieli et al. (2016) and Prata and Bernardo (2014). In addition to the THI images of clear and cloudy sky when looking through the gas cells, THI images of both clear sky and isolated cumulus clouds in the field of view, acquired on 05/17/2016, were used. The SO_2–ALTA processed THI images are given in the electronic supporting material section. Weather conditions for this latter dataset consisted of trade winds from the North-East and low humidity. These images were processed using SO_2–ALTA to test the capability of the new algorithm to retrieve SO_2 path-concentrations in the presence of strong background heterogeneities.

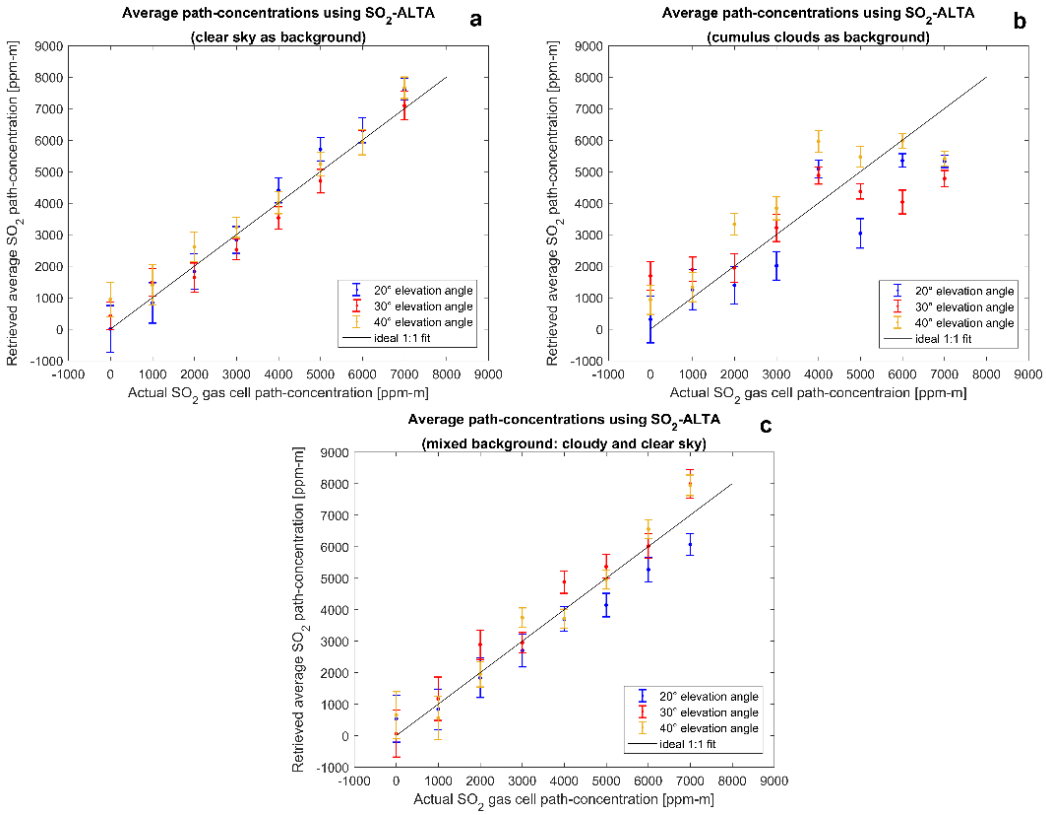

Figure 3.7. Average path-concentrations retrieved using SO_2–ALTA under the three weather conditions: clear sky (**a**), fully cloudy (**b**), and partially cloudy (**c**). The values were obtained by averaging the retrieved SO_2 at each pixel for each THI image. Standard deviation bars are displayed as well as an ideal 1:1 fit (black line). Ideally, the data points should fall on the black line.

Figure 3.7 compares known and retrieved average path-concentrations using SO_2–ALTA under the three weather conditions. The different colors indicate different elevation angles. The black line is a 1:1 fit and, ideally, each data point should fall close to the line. Figure 3.7a shows that under clear sky conditions, SO_2–ALTA performs similarly to dual view approaches. Figure 3.7b shows that this novel single point approach performs better for clouds than the dual-view method (cf. Figure 3.4). Figure 3.7c

shows that, despite strong background heterogeneities created by the presence of both clouds and patches of clear sky in the same image, SO_2–ALTA performed well. The lower the elevation angle is, the lower is the thermal contrast. So, measurements become more difficult at low elevation angles. The coefficients of determination were 0.9926, 0.7842, and 0.9764, respectively for clear sky, cloudy sky, and mixed backgrounds.

Figure 3.8 shows the average THI spectra for each image acquired at the 40° elevation angle, under clear sky conditions, but observed over a three day period. The fact that radiance does not change systematically as gas concentration increases shows that, although the clear-sky conditions prevailed for each measurement, the atmospheric properties (predominantly temperature and humidity) were changing. Despite this variability, the algorithm was able to effectively retrieve the SO_2 path-concentration that was in the gas cells.

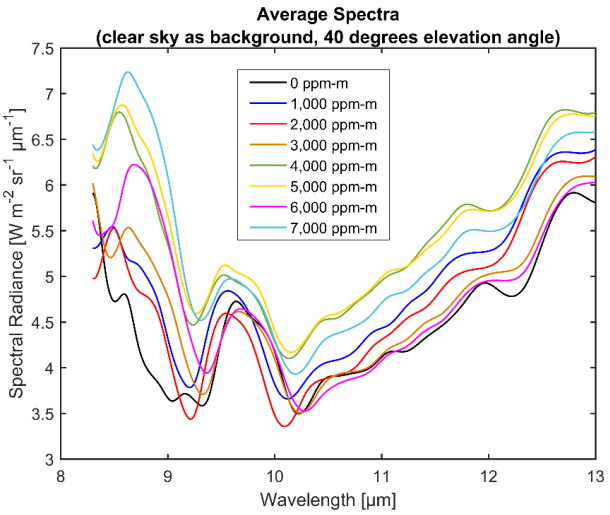

Figure 3.8. Average spectra obtained from each THI image under clear sky conditions. It can be seen that, despite the variability of the atmosphere (measurements taken over three days between July the 10th and the 12th), the algorithm was able to effectively retrieve the SO_2 path-concentration that was in the gas cells.

The SO_2–ALTA-processed clear sky THI images for the 20 °, 30 °, and 40 ° are displayed respectively in Figures 3.9, 3.10, and 3.11. Each figure contains 8 Images, numbered 1-8, corresponding to a different SO_2 path-concentration. At the same way, the SO_2–ALTA-processed cloudy sky THI images for the 20 °, 30 °, and 40 ° are displayed in Figures 3.12, 3.13, and 3.14. Finally, the SO_2–ALTA-processed mixed clear and cloudy sky THI images for the 20 °, 30 °, and 40 ° are displayed in Figures 3.15, 3.16, and 3.17. Ideally, if the algorithm worked perfectly, each of the 8 images in each of the figures should be a uniform color corresponding to the relevant SO_2 path-concentration.

For the clear sky case, it can be seen that the images displayed in Figure 3.9, which were obtained at the low elevation angle of 20 °, display several non-uniformities. These features are particularly evident in Images 5 through 8 of Figure 3.9. Since the sky was observed to be clear during the measurements (see Figure 3.2a in the chapter), it is thought that these features could be either sub-visual clouds, such as cirrus, or thermals. The images obtained at higher elevation angles, look more uniform (Figures 3.10 and 3.11).

For the cloudy sky case, Figures 3.12, 3.13, and 3.14 show the SO_2–ALTA-processed cloudy THI images for 20 °, 30 °, and 40 ° elevation angles, respectively. Images 1-8 in Figure 3.14 look uniform as they were acquired at the high elevation angle of 40 °. Images 1-8 in Figures 3.12 and 3.13 present more non-uniformities that are thought to be related to low thermal contrast and to the SO_2–ALTA algorithm not being able to correctly account for cloud features.

For the mixed clear and cloudy sky case, Figures 3.15, 3.16, and 3.17 show the SO_2–ALTA-processed mixed background THI images for 20 °, 30 °, and 40 ° elevation angles. As in the other two cases, it can

be seen that Images 1-8 look roughly uniform at higher elevation angles (Figure 3.17). In fact, as in the cloudy cases, some background features can still be seen at lower elevation angles (particularly, Images 3 through 6 in Figure 3.15).

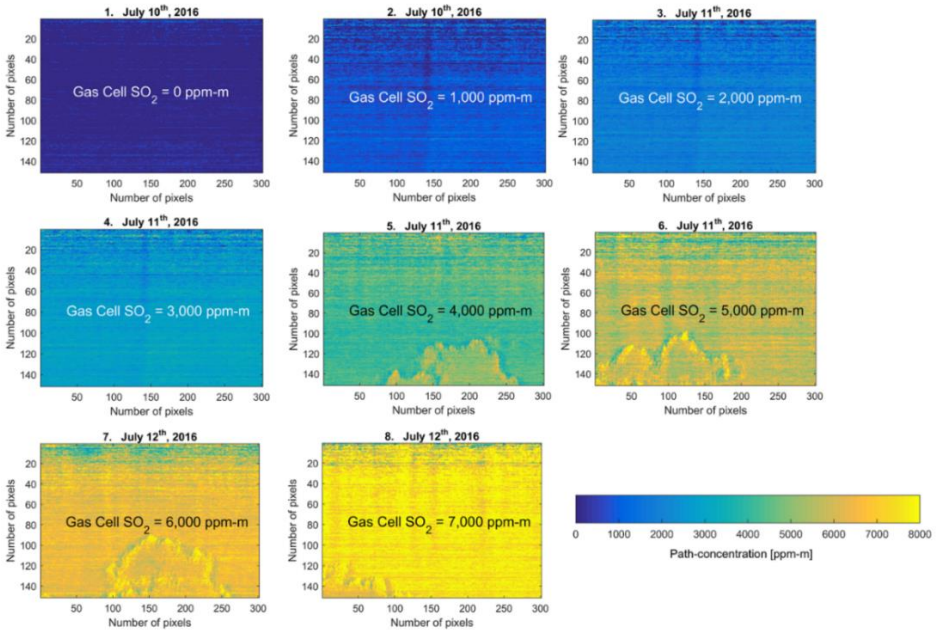

Figure 3.9. Images of clear sky background conditions when looking through a gas cell filled with known concentrations of SO_2 gas at 20° elevation angle. The images were processed using SO_2 –ALTA. The color indicates the path-concentration that was retrieved. The actual SO_2 gas concentration is written in the center of each image. Sub-visual cloudy features or thermals may be present in some of the images (particularly, Images 5 through 8).

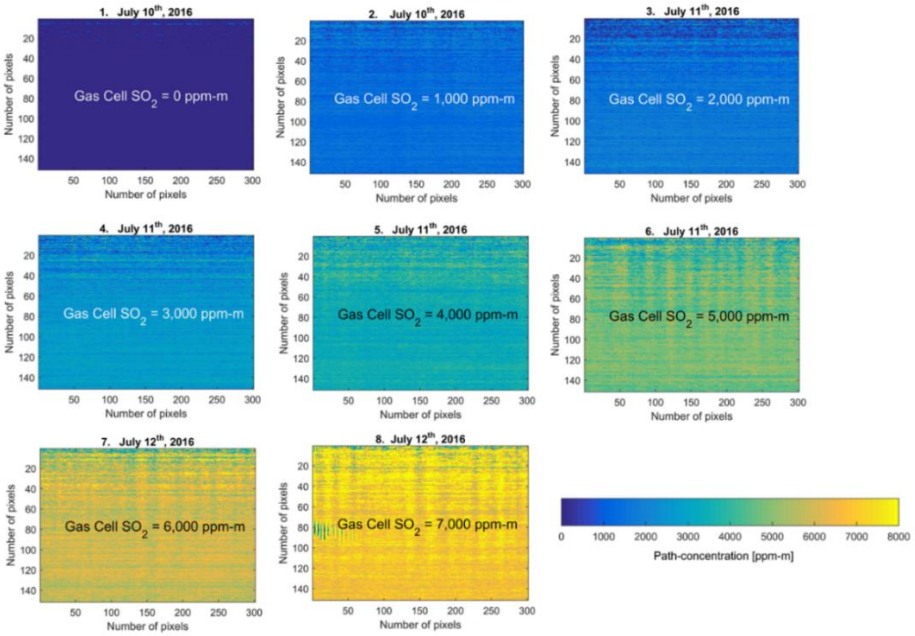

Figure 3.10. Images of clear sky background conditions when looking through a gas cell filled with known concentrations of SO_2 gas at 30° elevation angle. The images were processed using SO_2 –ALTA. The color indicates the path-concentration that was retrieved. The actual SO_2 gas concentration is written in the center of each image.

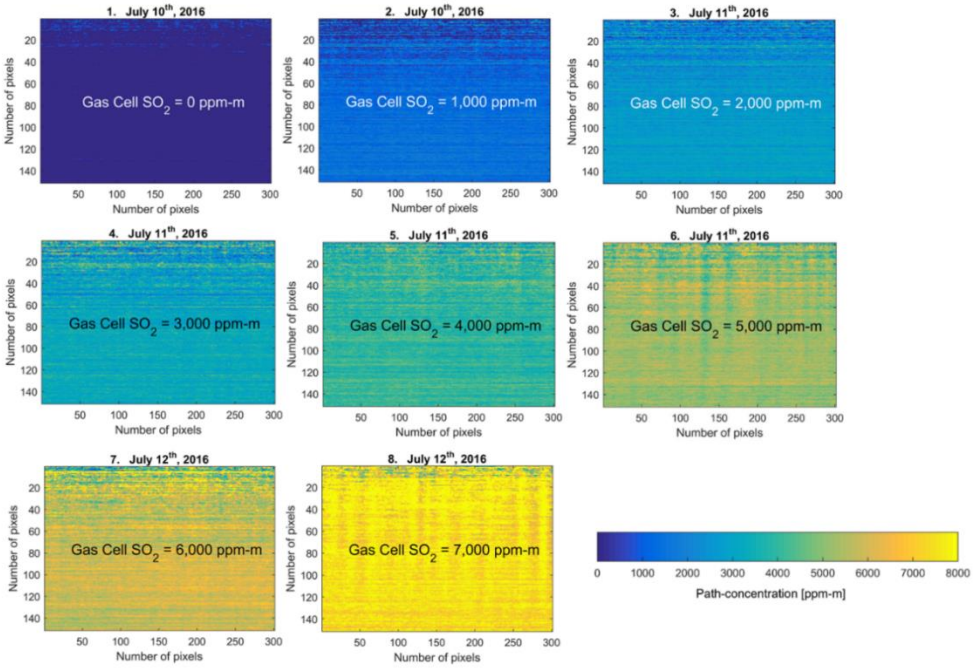

Figure 3.11. Images of clear sky background conditions when looking through a gas cell filled with known concentrations of SO_2 gas at 40° elevation angle. The images were processed using SO_2 –ALTA. The color indicates the path-concentration that was retrieved. The actual SO_2 gas concentration is written in the center of each image.

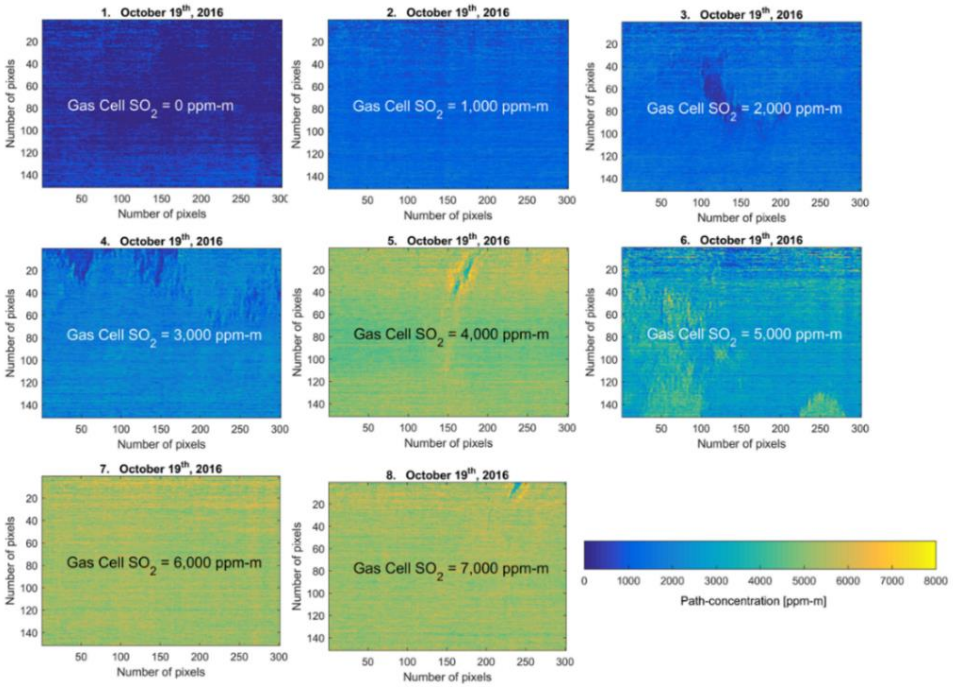

Figure 3.12. Images of cloudy background conditions when looking through a gas cell filled with known concentrations of SO_2 gas at 20 ° elevation angle. The images were processed using SO_2 –ALTA. The color indicates the path-concentration that was retrieved. The actual SO_2 gas concentration is written in the center of each image. Cloud-features or thermals that the algorithm was not able to account for can be seen.

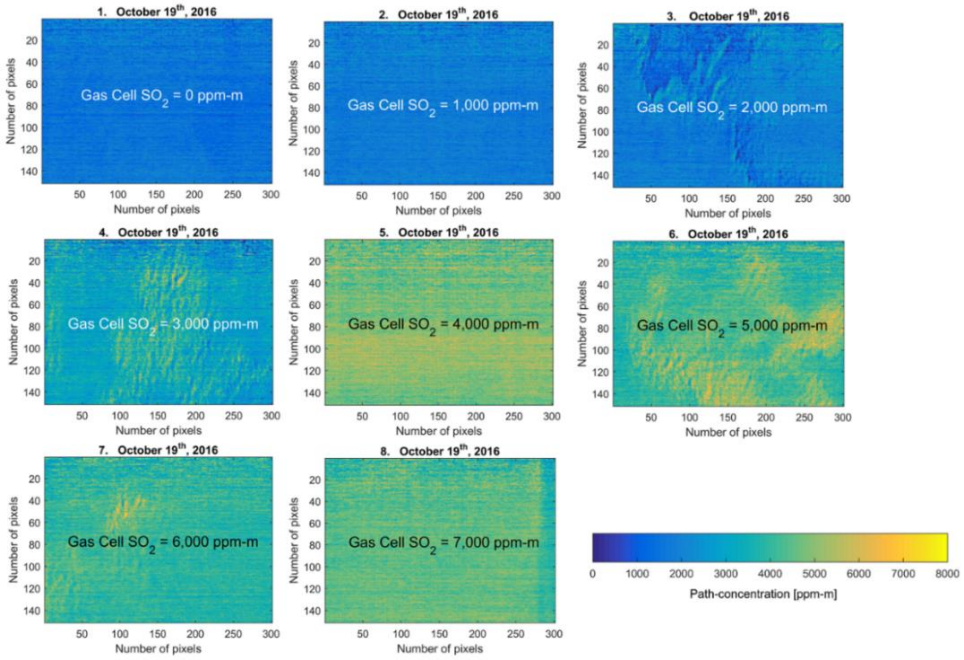

Figure 3.13. Images of cloudy background conditions when looking through a gas cell filled with known concentrations of SO_2 gas at 30° elevation angle. The images were processed using SO_2 –ALTA. The color indicates the path-concentration that was retrieved. The actual SO_2 gas concentration is written in the center of each image. Cloud-features or thermals that the algorithm was not able to account for can be seen.

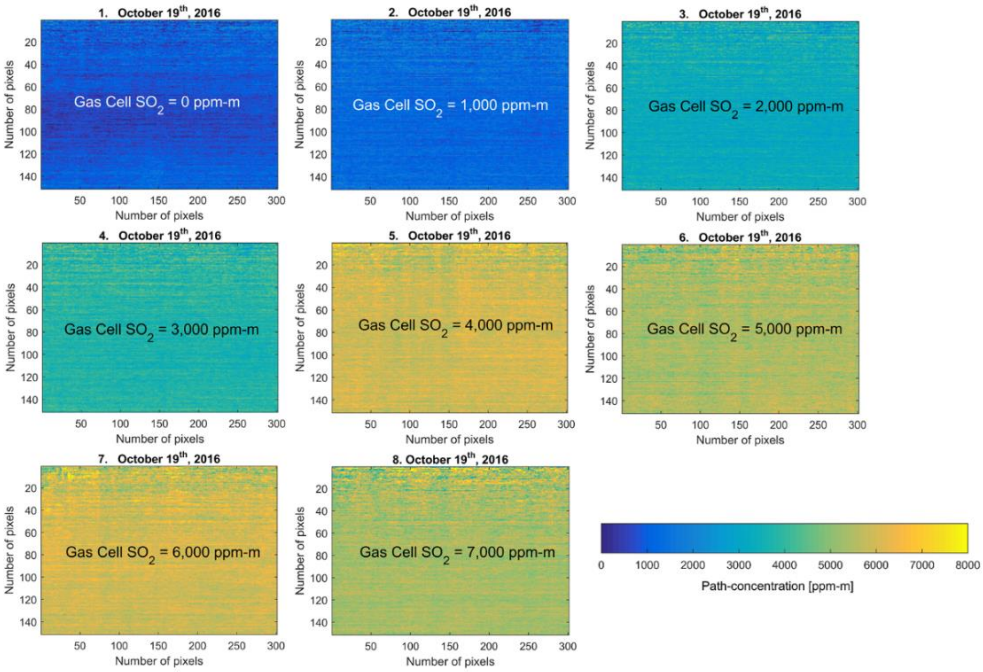

Figure 3.14. Images of cloudy background conditions when looking through a gas cell filled with known concentrations of SO_2 gas at 40° elevation angle. The images were processed using SO_2 –ALTA. The color indicates the path-concentration that was retrieved. The actual SO_2 gas concentration is written in the center of each image. These images are more uniform than those displayed in Figures 3.12 and 3.13. This is through to be related to higher elevation angles and therefore, better thermal contrast.

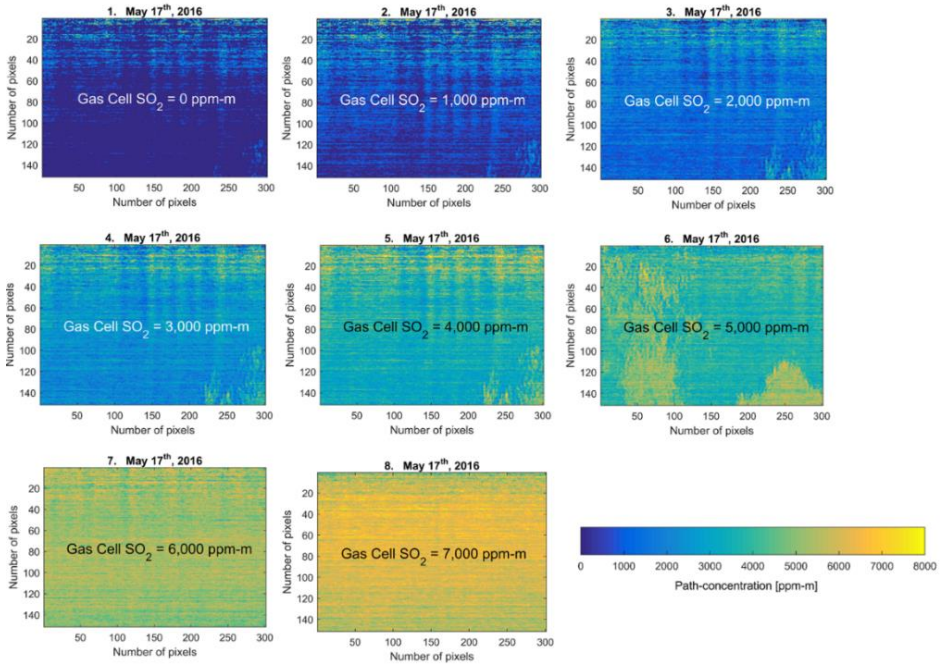

Figure 3.15. Images of the mixed background conditions when looking through a gas cell filled with known concentrations of SO_2 gas at 20 ° elevation angle. The images were processed using SO_2–ALTA. The color indicates the path-concentration that was retrieved. The actual SO_2 gas concentration is written in the center of each image.

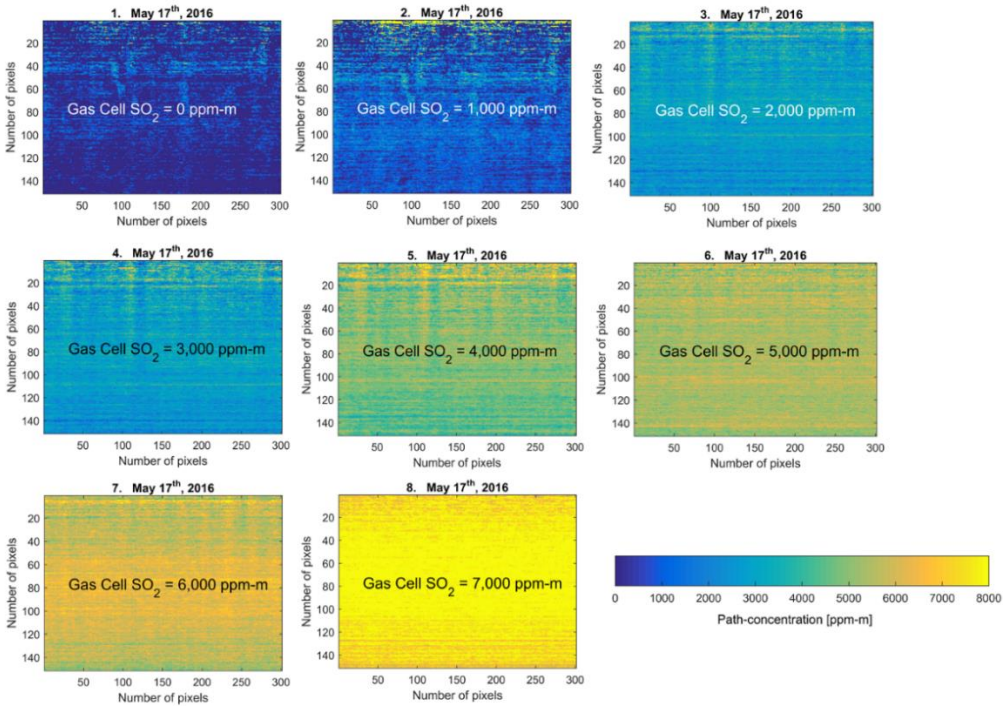

Figure 3.16. Images of the mixed background conditions when looking through a gas cell filled with known concentrations of SO_2 gas at 30 ° elevation angle. The images were processed using SO_2–ALTA. The color indicates the path-concentration that was retrieved. The actual SO_2 gas concentration is written in the center of each image.

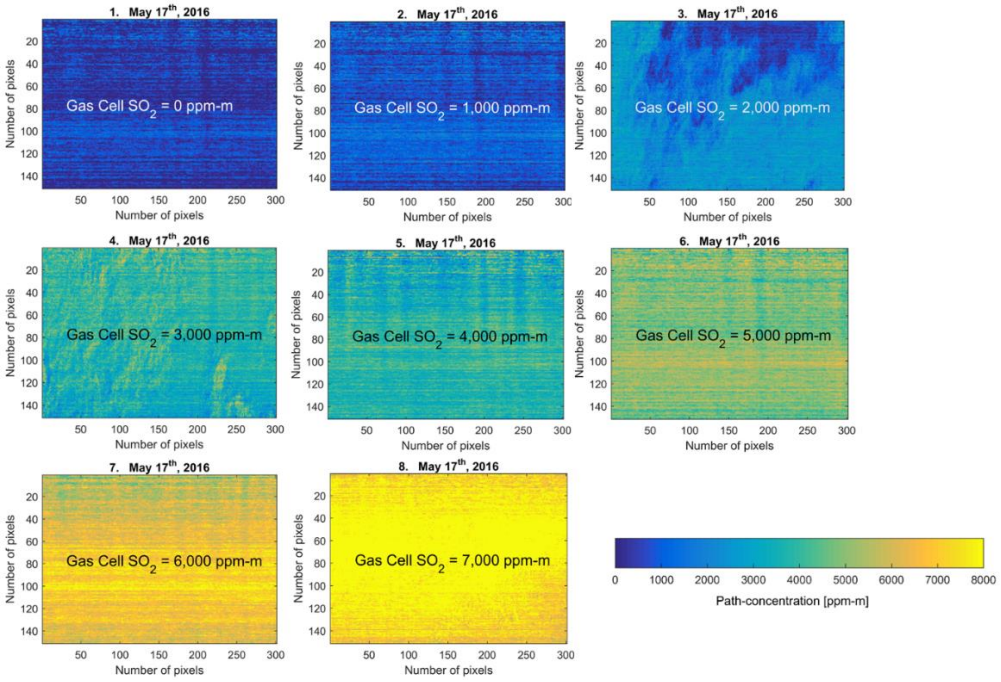

Figure 3.17 Images of the mixed background conditions when looking through a gas cell filled with known concentrations of SO_2 gas at 40 ° elevation angle. The images were processed using SO_2–ALTA. The color indicates the path-concentration that was retrieved. The actual SO_2 gas concentration is written in the center of each image.

3.7. SO_2-ALTA daytime and nighttime tests at Kīlauea volcano under clear and cloudy conditions.

To further evaluate the performance of the new single point inversion technique, THI was used to acquire images of the volcanic plume rising from the Halemaʻumaʻu vent on the summit of Kīlauea volcano. Time series of THI images were collected on 07/26/2016 during the afternoon, at sunset, and during the night (Figure 3.18). Standard Hawaiian Northeasterly trade wind weather was observed during the time of the measurements. The sky was clear during the afternoon and at sunset. After sunset, at 7:20 pm (local time), the weather changed as low altitude clouds rolled in from the East, covering the summit area. For this test, SO2-ALTA was modified to account for elevation angle changes.

Figure 3.18. THI on the rim of Kīlauea caldera, pointed at Halemaʻumaʻu crater. THI images of the volcanic plume were acquired both during daytime and nighttime conditions to test the effectiveness of SO2-ALTA.

Figure 3.19a shows both a raw THI difference image of the plume viewed against clear sky on 07/26, at 3:30 pm (local time) and the same image processed using SO2-ALTA. The raw THI difference image was obtained by subtracting channel 8.6 μm from channel 10 μm to highlight SO_2 features. The complexity of the atmosphere does not make the SO_2 gas immediately visible. The SO2-ALTA

processed THI image shows a color map of the SO_2 path-concentration as retrieved in the volcanic plume by SO_2-ALTA. The path-concentration that was retrieved for the plume ranges between 4 000 ppm-m and 8 000 ppm-m. The model was trained for SO_2 path-concentrations of up to 17 000 ppm-m. These retrieved results for the volcanic plume at Kīlauea are in the same range of other measurements carried out with both UV and TIR methods at the same site (Elias and Sutton 2012; Kern et al. 2012; Kern et al. 2013; Gabrieli et al. 2016).

The background seen next to the plume in the SO_2-ALTA processed THI image appears to have an SO_2 path-concentration that varies between 1 000 ppm-m and 2 000 ppm-m. However, no plume was visually observed in that location. This background SO_2 path-concentration anomaly is considered to be an instrumental artifact of THI due to low sensitivity during daytime conditions. In fact, Gabrieli et al. (2016) showed that, under daytime conditions at low elevation angles, the SO_2 gas detection sensitivity of THI is about 1 000 ppm-m (Figure 3.19). So, the background anomaly, observed here, appears to be related to the sensitivity of the THI instrument, rather than SO_2-ALTA. This is further investigated in Figure 3.19b. Figure 3.19b shows a raw THI image, obtained by calculating the difference between the 8.6 μm band and the 10 μm band, of the plume acquired at night with better thermal contrast and the same image processed using SO_2-ALTA.

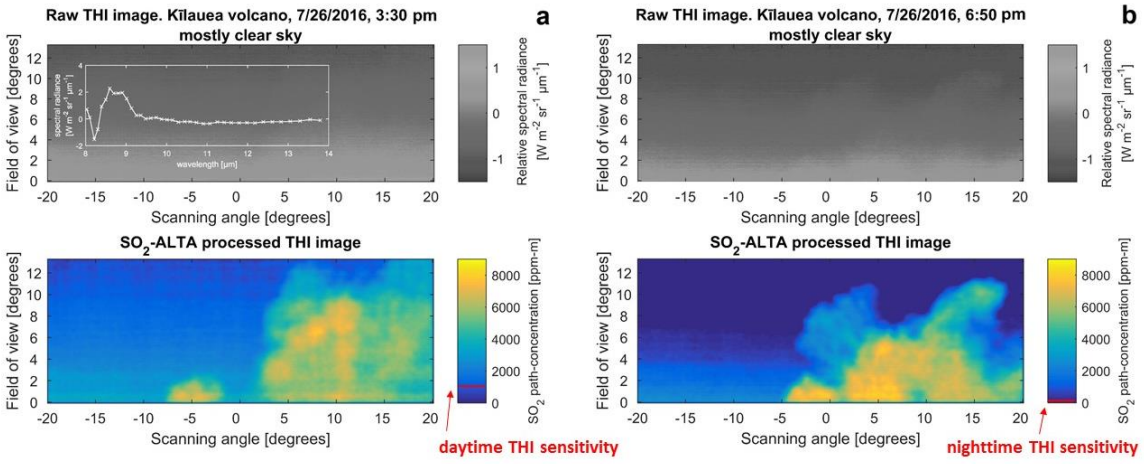

Figure 3.19. (a) Raw THI images (above in grey scale) and SO_2-ALTA processed images (below in colors) of the plume viewed against clear sky on 07/26, at 3:30 pm (local time). **(b)** Raw THI image (above) and SO_2-ALTA processed image (below) of the plume viewed against clear sky on 07/26, at night at 6:50 pm (local time). The raw THI images were obtained by subtracting channel 8.6 μm from channel 10 μm to SO_2 features, as reported in the small graph superimposed to the raw THI image of figure 3.19a. It can be seen that the raw image backgrounds are mostly homogenous: no clouds are present. The daytime and nighttime THI sensitivity are reported on the color-bar.

It can be seen that most of the background sky is dark blue and has an SO_2-ALTA-retrieved SO_2 path-concentration of roughly 0 ppm-m. In this case, the thermal contrast between the plume and the background is much higher than in Figure 3.19a. In fact, in accordance with Gabrieli et al. (2016), the SO_2 sensitivity of THI is much higher at night. During nighttime conditions and strong temperature contrast, THI can detect SO_2 gas path-concentrations as low as 100 ppm-m (Gabrieli et al. 2016).

Figure 3.20 shows a raw THI image and the same image processed using SO_2-ALTA of the plume viewed against a mixture of clouds and clear sky on 07/26, at 7:20 pm (local time). A layer of clouds can be clearly seen in light grey in the raw THI image of Figure 3.20. The SO_2-ALTA processed THI image shows a map of the SO_2 path-concentration as retrieved in the volcanic plume by SO_2-ALTA. It appears that the new model was successfully able to isolate SO_2 plume features, despite the presence of the clouds. Similarly to Figures 3.19a and b, background SO_2 gas path-concentration anomalies are present. In this case, they are related not only to instrumental effects, but they also appear to be linked to the background heterogeneities of the cloud layer.

One way to identify and correct for these background anomalies would be to employ time-series monitoring. In fact, the SO_2 gas path-concentration background anomalies would appear nearly static in

time-lapse sequences as they are related to either poor thermal contrast, low instrumental sensitivity, or background heterogeneities. On the other hand, the plume would appear to be in motion.

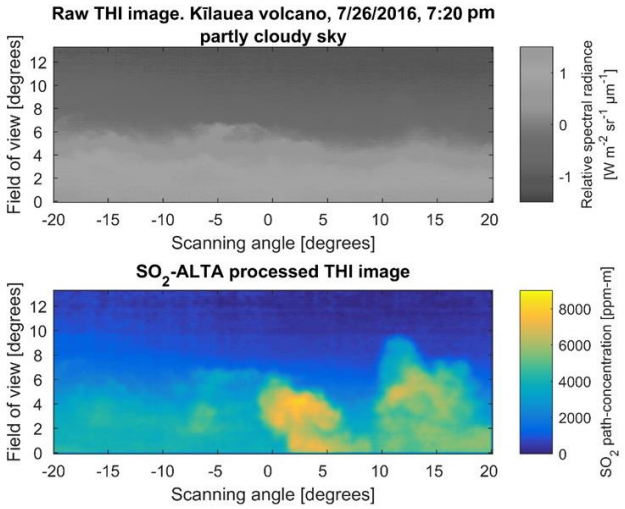

Figure 3.20. Raw THI image and SO_2-ALTA processed image of the plume viewed against clear and low-altitude clouds on 07/26/2016, at 7:20 pm (local time). The raw THI image was obtained by subtracting channel 8.6 μm from channel 10 μm. A low altitude layer of clouds can be seen in the raw THI image in light grey.

3.8. Performance Summary

Table 3.2 summarizes the three SO_2 inversion algorithms evaluated in this paper and the conditions under which they were tested. Figure 3.21 shows a summary of the performance of the two dual-view approaches and the new single point SO_2–ALTA in detecting SO_2 path-concentrations under clear sky conditions. Figure 3.22 shows a summary of the performance of the Gabrieli et al. (2016) approach and SO_2–ALTA in detecting SO_2 path-concentrations under fully cloudy conditions. Figure 3.23 shows a summary of the performance of SO_2–ALTA in detecting SO_2 path-concentrations under variable mixed conditions (both clouds and clear sky).

Table 3.2. A summary of the three SO_2 inversion algorithms being considered in this paper and the conditions under which they were tested.

	Dual-view approach	Single point approach	Tested with clear sky background ?	Tested with cloudy background ?	Tested with combination of both clear sky and cumulus clouds ?	Tested with cirrus clouds ?
Gabrieli et al. (2016)	yes	no	Tested in this study (also tested by Gabrieli et al. (2016))	Tested in this study	no	no
Prata and Bernardo (2014)	yes	no	Tested in this study (also tested by Prata and Bernardo (2014))	Indirectly tested by using Gabrieli et al. (2016) as a proxy	no	no
SO_2–ALTA	no	yes	Tested in this study	Tested in this study	Tested in this study	Tested in this study

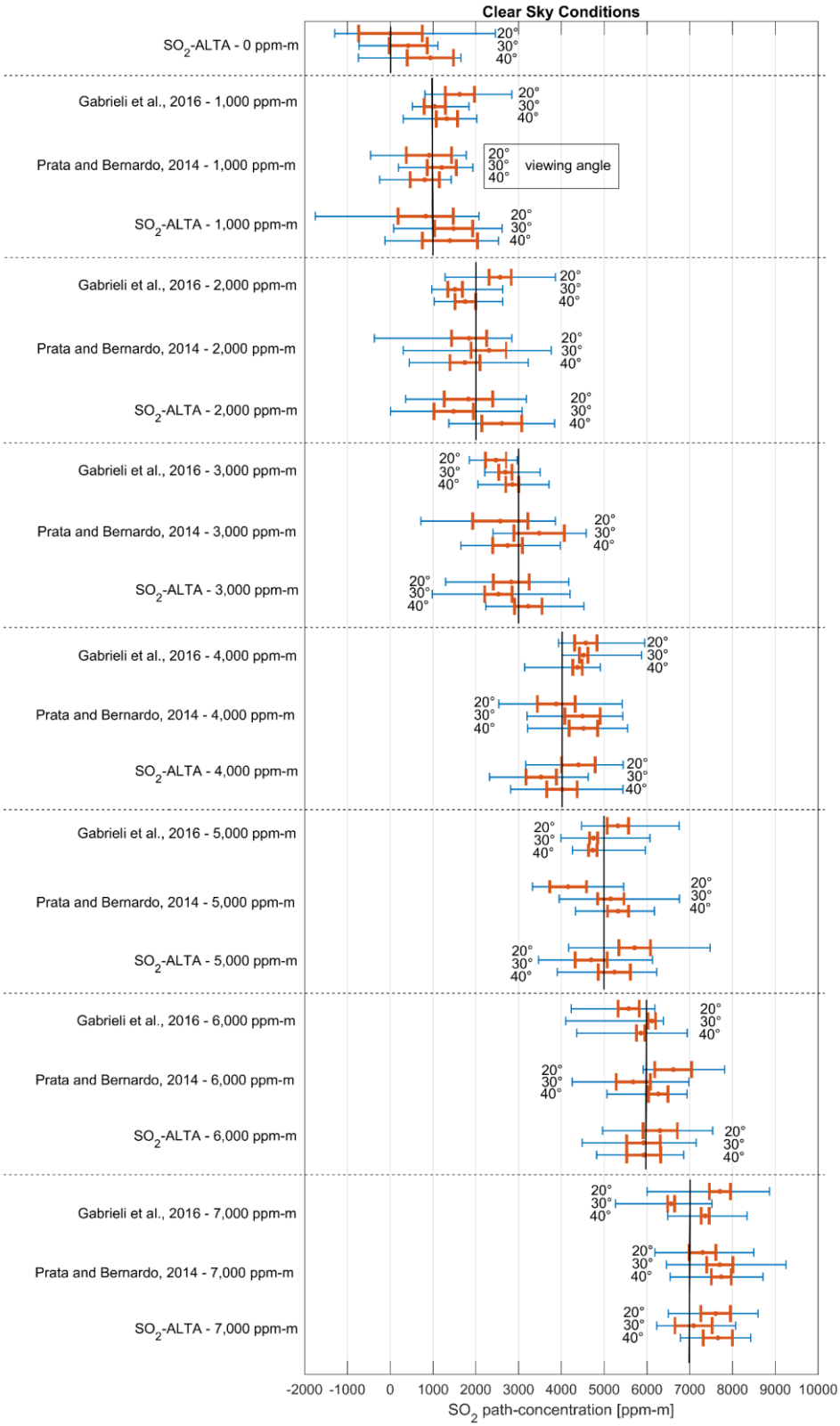

Figure 3.21. Summary of the performance of the two dual-view approaches and the new single point SO_2-ALTA in detecting SO_2 path-concentrations under clear sky conditions for all of the elevation angles and all of the SO_2 path-concentrations. The length of the red line is defined by the standard deviation limit around the mean, and the blue line is defined by the minimum and the maximum SO_2 path-concentrations retrieved. Ideally, the retrieved SO_2 path-concentrations should fall close to the vertical black line for each section.

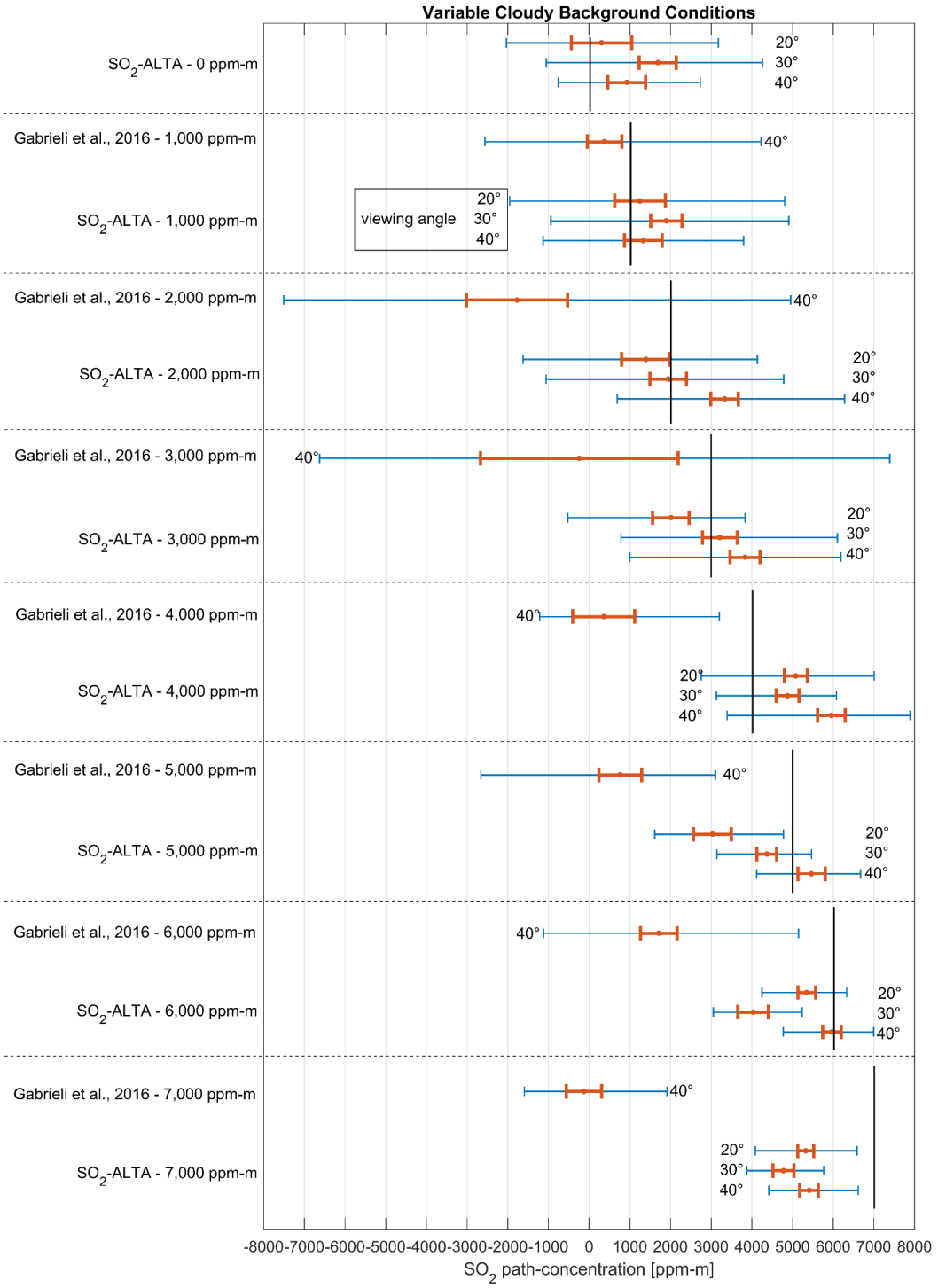

Figure 3.22. Summary of the performance of the Gabrieli et al. (2016) approach and the new SO_2–ALTA in detecting SO_2 path-concentrations variable cloudy conditions for all of the elevation angles and all of the SO_2 path-concentrations. The length of the red line is defined by the standard deviation limit around the mean, and the blue line is defined by the minimum and the maximum SO_2 path-concentrations retrieved. Ideally, the retrieved SO_2 path-concentrations should fall close to the vertical black line for each section.

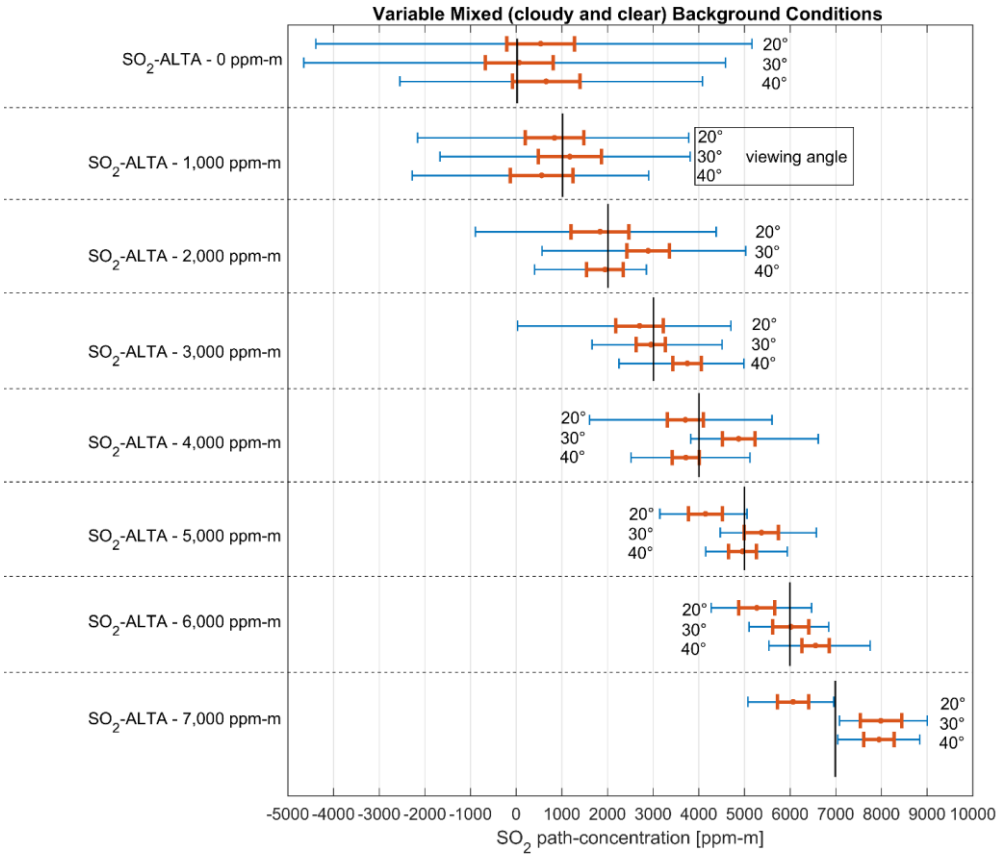

Figure 3.23. Summary of the performance of the new SO_2–ALTA in detecting SO_2 path-concentrations variable mixed (clouds and blue sky patches) conditions for all of the elevation angles and all of the SO_2 path-concentrations. The length of the red line is defined by the standard deviation limit around the mean, and the blue line is defined by the minimum and the maximum SO_2 path-concentrations retrieved. Ideally, the retrieved SO_2 path-concentrations should fall close to the vertical black line for each section.

Dual view approaches suffer from background heterogeneities and do not work when clouds are present. An additional problem with dual-view approaches is the fact that they do not properly account for the effect that the intervening atmosphere (between the plume and the sensor) has on the retrieval algorithm. Figure 3.24a shows the viewing geometry of a sensor and two hypothetical plumes at different distances. Figure 3.24b shows simulated radiances for conditions with various SO_2 gas concentrations for a plume 0.5 km and 5 km away the sensor (Figure 3.24a). Because results for SO_2 path-concentrations of 5 000 ppm-m and 2 500 ppm-m at distances of 5 and 0.5 km are very similar, it appears that almost identical spectral radiances can be obtained for different SO_2 path-concentrations if the plume is modelled at different distances. This degradation of the SO_2 signal with distance is due to absorption and emission from the atmosphere between the plume and the sensor. This plume distance effect is not properly accounted for in either of the two dual-view approaches.

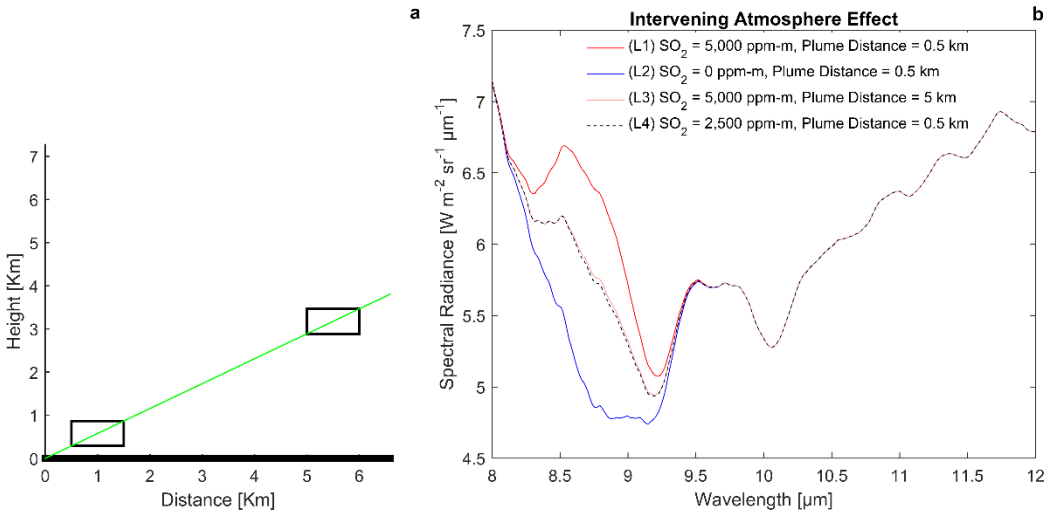

Figure 3.24. (a) Location of the two simulated plumes (represented by the two black boxes). The sensor viewing the plumes is located in the origin of the axis and the viewing path is represented by the green line. **(b)** The red line shows spectral radiances for SO_2 path-concentrations of 5 000 ppm-m at 0.5 km distance (L1). The blue line shows spectral radiances for SO_2 path-concentration of 0 ppm-m (L2). The pink and black dashed lines show the spectral radiances for SO_2 path-concentrations of 5 000 ppm-m and 2 500 ppm-m at distances of 5 km and 0.5 km, respectively (L3 and L4) simulated spectral radiances for two SO_2 concentrations.

Conversely, the SO_2-ALTA approach should be able to distinguish these two conditions (the plume distance effect) and correctly retrieve SO_2 path-concentrations. Figure 3.25 shows three curves. The red curve shows the difference between the two very similar spectral radiance curves L3 and L4, plotted in Figure 3.24b. The blue one shows the difference between L3 and L5, where L5 is a spectral radiance curve obtained for an additional hypothetical plume with 2 400 ppm-m of SO_2 at a distance of 0.5 km. The yellow curve displays the difference between L3 and L6, where L6 is a spectral radiance curve obtained for another hypothetical plume with 2 600 ppm-m of SO_2 at a distance of 0.5 km. Subtle plume distance-dependent spectral differences exist within the spectral region from 8 µm to 10 µm. These spectral differences peaks at 8.815 µm. This wavelength is thus important when distinguishing plumes of similar SO_2 concentration at different distances. The subtle spectral differences seen in Figures 3.24b and 3.25 suggest that excellent sensor signal-to-noise is necessary for SO_2 plume retrievals, particularly for high water vapor, cloudy background conditions, and if the plume distance cannot be determined accurately. The Noise Equivalent Spectral Radiance (NEdL) of the THI instrument, the sensor used in this study, at 8.82 µm is shown as the error bar in Figure 3.25. It can be seen that our current sensor is barely able to resolve spectra, with sufficient signal-to-noise, to distinguish these spectral differences.

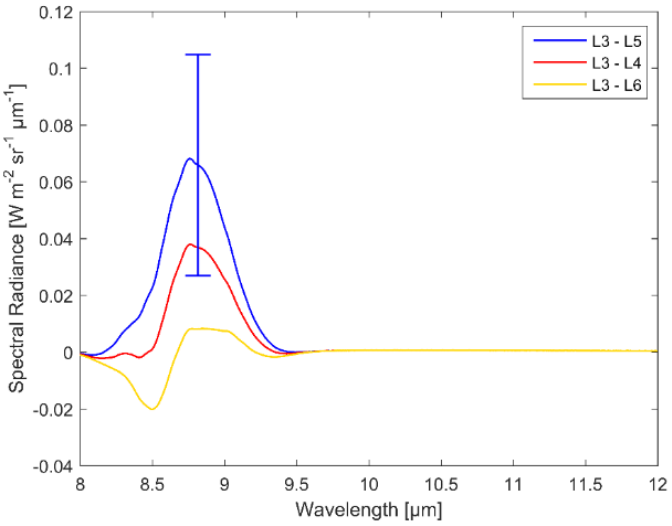

Figure 3.25. Spectral radiance differences between various spectra shown in Figure 3.20. L3, L4, L5, and L6 correspond to SO_2 path-concentrations of 5 000 ppm-m, 2 500 ppm-m, 2 400 ppm-m, and 2 600 ppm-m at distances of 5 km, 0.5 km, 0.5 km, and 0.5 km, respectively. The Noise Equivalent Spectral Radiance (NEdL) of the THI instrument at 8.82 µm is shown as the error bar.

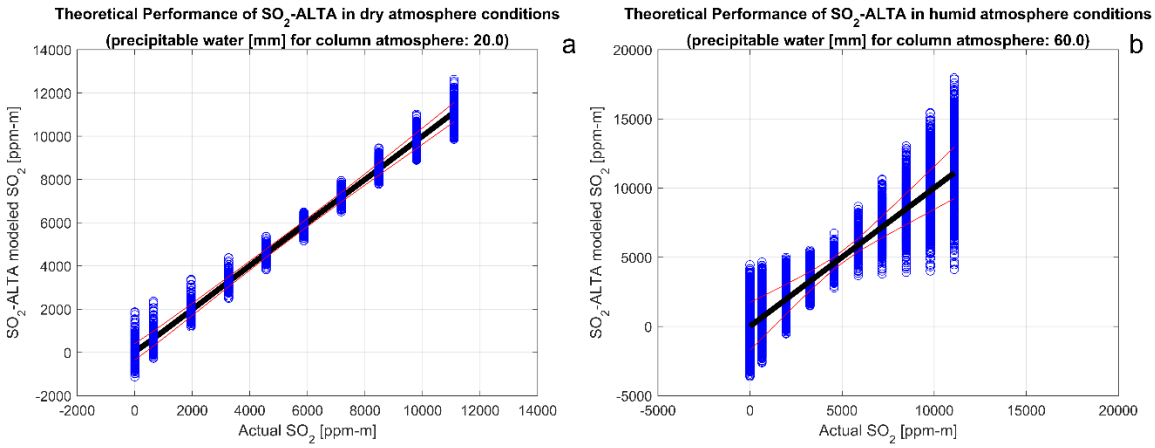

Figure 3.26. Theoretical performance of SO2-ALTA under dry and humid atmospheric conditions for 20° elevation angle. Similar concentration SO_2 plumes were modelled at different distances (0 km to 5 km in 0.1 km increments) from the sensor under (a) dry and (b) humid conditions. The red line is the standard deviation. A total of 6 120 simulations were carried out for each of the two atmospheric conditions.

This conundrum is further investigated in Figure 3.26. Here, simulated plumes with similar SO_2 concentrations are modelled at different distances between 0 km and 5 km from a hypothetical sensor. SO_2-ALTA is then used to retrieve SO_2 path-concentrations from the simulated plumes. It can be seen that SO_2-ALTA performed well in retrieving SO_2 plume concentrations at different distances under clear sky and dry conditions (the total column integrated water vapor was 20 mm) (Figure 3.26a). Under cloudy and humid atmospheric conditions (the total column integrated water vapor was 60 mm), SO_2-ALTA performed poorly (Figure 3.26b). This simulation suggests that SO_2 path-concentrations can be successfully retrieved from plumes at different distances using SO_2-ALTA under low humidity conditions. Retrievals of SO_2 path-concentrations from plumes seen against a cloudy background under high humidity conditions are much more challenging.

Similarly, the test carried out in this paper showed that SO_2–ALTA performed well in cloudy conditions when the amount of water vapor in the atmosphere was low (the partially cloudy background case). In fact, in this case, atmospheric conditions were drier and so, good SO_2-ALTA retrievals (errors less than 20%) were obtained even for lower viewing elevations (20°) and cloudy backgrounds.

Conversely, during high humidity cases and overcast sky (the fully cloudy background case), SO_2-ALTA performed less accurately with errors greater than 50%.

3.9. Discussion and conclusion

The inversion of SO_2 path-concentration using ground-based spectral TIR methods is complicated by emission and absorption processes within the plume, the background and the foreground regions. Two dual-view algorithms (Gabrieli et al. 2016; Prata and Bernardo 2014) were validated using TIR measurements with gas cells to provide realistic and known path-concentrations of SO_2. Both clear and cloudy background conditions were tested. The validation study carried out here showed that the dual-view approaches of Gabrieli et al. (2016) and Prata and Bernardo (2014) suffer from a variety of issues, which limit their usefulness in SO_2 retrievals. These issues are the assumption of clear sky background conditions and the plume distance effect. The process of comparing regions in and out of the plume assumes the background sky is homogeneous. In fact, cloudy backgrounds drastically reduce their performance

This chapter also presented a new inversion algorithm, SO_2-ALTA, which is capable of single point SO_2 path-concentration retrievals. SO_2–ALTA employs a PLSR model that was trained using MODTRAN5 spectral radiance look-up table calculations for a variety of plume and atmospheric conditions. The performance of SO_2–ALTA was similar to those of the two dual-view approaches under clear sky conditions, but much better under cloudy background conditions. The gas cell tests, which were carried out here, suggest that errors in the SO_2–ALTA retrieval procedure are 20% for the clear sky conditions and 50-60% of the cloudy sky background conditions.

The initial work described here is promising and offers the possibility of improved SO_2 retrievals. The SO_2-ALTA approach could also be used for other gases, such as SO_2, CO_2, H_2O, and SiF_4. The retrieval algorithm is currently limited to tropical atmospheres as it was trained using Hawai‘i and Puerto Rico soundings, but it would be simple to expand its geographic applicability by building appropriate MODTRAN databases to train additional PLSR models. It is expected that SO_2-ALTA will perform better at higher latitudes where less water vapor is present in the atmosphere.

CHAPTER 4

APPLICATIONS OF QUANTITATIVE THERMAL INFRARED HYPERSPECTRAL IMAGING (8-14 MICRON): MEASURING VOLCANIC SO_2 MASS FLUX AND DETERMINING PLUME TRANSPORT SPEED USING A SINGLE SENSOR

In preparation for publication as: Gabrieli, A., Wright, R., Porter, Lucey, P.G. (2018). Applications of quantitative thermal InfraRed hyperspectral imaging (8-14 μm): measuring volcanic SO2 mass flux and determining plume transport speed using a single sensor.

Abstract — Remote measurements of sulfur dioxide (SO_2) emission rate (mass flux), released by passive volcanic degassing, are a key diagnostics of volcanic behavior and are important for public health. Despite the significance of measuring SO_2 mass flux at active volcanoes, an accurate method is still very difficult to obtain due largely to uncertainties of plume velocities, which can be as high as 100%. Here, we present a new InfraRed imaging method for deriving SO_2 flux at active volcanoes with less than 20% plume transport speed uncertainties. The Thermal Hyperspectral Imager (THI) was used for this study. THI is an uncooled remote sensing long-wave TIR imaging hyperspectral sensor that can obtain ~50 samples between 8 μm and 14 μm. THI measurements of SO_2 at the summit of Kīlauea volcano are presented. Spatial distribution of SO_2 path-concentrations was obtained from the THI images by processing them using a newly developed SO_2 retrieval algorithm, the SO_2 Amenable Lookup Table Algorithm (SO_2-ALTA). The sampling rate (30 Hz) of the microbolometer camera within THI allows for wind speed derivation directly from the sequential frames. Volcanic plume motion can be thus inferred by tracking plume features in sequential frames using spatial correlation techniques and knowing the camera angular calibration. Volcanic SO_2 flux were estimated from the spatial distribution of SO_2 and wind velocity. We evaluated temporal trends of SO_2 fluxes both during the day and the night at the summit of Kīlauea volcano under both clear sky weather with Northeasterly trade winds and cloudy sky conditions with low variable wind. The camera and techniques described in this paper provide an effective tool for monitoring SO_2 fluxes remotely under a variety of background conditions (clear and cloudy sky, cold and hot backgrounds).

4.1. Introduction

Volcanic gas emission rate (flux) measurements are routinely carried out at various volcanoes in support of volcanic hazard assessment (e.g., Aiuppa et al. 2007; Gabrieli et al. 2015) and public health (EPA, 2011). These data provide insights on magma movements within a volcanic plumbing system, eruption rates (Allard et al. 1994), and mass balance (e.g., Allard et al. 2014). The primary species of interest in these measurements is SO_2, due to its ubiquitous presence in volcanic plumes and its strong absorption spectral features in the UltraViolet (UV) and absorption/emission features in the InfraRed (IR) regions of the electromagnetic spectrum. Fluxes of other volcanic gases are typically found by combining SO_2 flux data with mass ratios (i.e., X/ SO_2) determined by direct sampling, in-plume sampling or remote sensing (e.g., Gerlach et al., 1998; Wardell et al., 2001). Measuring volcanic SO_2 is also important for environmental monitoring and public health. In fact, SO_2 reacts chemically with sunlight and the atmosphere to form acidic sulfate aerosols, which can threaten people, animals, plants, and be damaging to infrastructures (e.g., Baxter 1999; Schmidt 2014; Zuccaro et al. 2014).

Remote SO_2 flux measurements are usually obtained by employing passive spectroscopic approaches. Various UV sensors have been used to obtain SO_2 flux information from point measurements by traversing underneath the volcanic plume a few km from source, by car, boat or plane, with a zenith pointing UV spectrometer, to measure integrated SO_2 concentrations across the plume's cross section and then multiplying this by the speed at which the plume passes over the traverse route (e.g., Moffat and Millan 1971; Stoiber and Jepsen 1973; Stoiber et al. 1983). Correlation spectrometers and similar, more recent, upgraded sensors, like DOAS or Flyspec, have been used for the past thirty years in this capacity (e.g., Stoiber et al. 1983; Edmonds et al. 2003; Galle et al. 2003; Horton et al. 2005; Oppenheimer et al. 2004). UV imaging has recently been performed at active volcanoes (e.g., Bluth et al. 2007; Mori and Burton 2009; Kern et al. 2013). Such imaging provides valuable synoptic views of the spatial distributions and temporal motion of SO_2 gas from which mass flux can be derived (e.g., Bluth et al. 2007). A limitation, however, is that these UV techniques, both imaging and non-imaging, can only be used in daytime conditions and only allow for SO_2 retrievals.

Open-path Fourier Transform InfraRed (FTIR) spectroscopy can be employed for retrieving fluxes of various volcanic gases of interest, such as SO_2, CO_2, H_2O, and SiF_4, which have distinctive absorption and emission features in the IR, both during the day and night (Love et al. 1998; Francis et al. 1998; Oppenheimer et al. 1998; Goff et al. 2001; Oppenheimer et al. 2006; La Spina et al. 2015). Despite the possibility of multiple gas retrievals and the high spectral resolution, FTIR is still mostly based on point measurements. Respectively in 2014 and 2016 both low spectral resolution (Prata and Bernardo 2014) and hyperspectral thermal imaging (Gabrieli et al. 2016) of volcanic SO_2 plumes have been performed.

Obtaining accurate gas fluxes at active volcanoes requires also accurate plume velocity measurements. These are usually obtained with anemometers located a few meters above ground and often several km away from the plume (Mc Gonigle et al. 2005). This is a significant issue that complicates the measurements and their processing. In fact, estimates of the true plume velocity can be subject to errors larger than 100% and the uncertainties on those measurements remain mostly unquantified in the literature (Mc Gonigle et al. 2005). Wind speed measurements carried out at anemometer heights can vary dramatically from those which could be observed a few hundred meters above the surface (Archer and Jacobson, 2003). Volcanic topography may additionally increase such discrepancies (e.g., Favalli et al. 2004). Although more accurate methods of estimating wind speed do exist (e.g., Doppler radar with reported errors of less than 10% in Walter et al. 2016), these are rarely utilized by volcanologists as they often complicate measurement campaigns at active volcanoes by being impractical in remote field environments (Mc Gonigle et al. 2005). For these reasons, plume transport speed uncertainties are the main error source in volcanic flux measurements, thus limiting the value of flux time series.

Here, we present measurements of volcanic SO_2 emission rates (obtained at Kīlauea volcano during July 2017) with a hyperspectral uncooled imaging spectrometer, the Thermal Hyperspectral Imager (THI)

(Wright et al. 2013; Gabrieli et al. 2016; and Gabrieli et al. 2017). We evaluated temporal trends of SO_2 fluxes both during day and night by employing THI images and a newly developed SO_2 retrieval algorithm, the SO_2 Amenable Lookup Table Algorithm (SO_2-ALTA).

The ability of THI to obtain images of the plume both during the day and the night makes it ideal for deriving plume transport speed with low uncertainties. In fact, THI can collect sequential hyperspectral image frames at 30 Hz, which is fast enough for tracking plume features and deriving accurate plume velocity measurements. The field of view of THI is about 12° and thus, one pixel corresponds to about 0.75 m at the 2 km vent distance in this study (Gabrieli et al. 2016).

Volcanic plume motion can be inferred with THI by tracking plume features in sequential images using spatial correlation techniques (i.e., Berryman 1985). In order to convert camera pixel motion into wind speed, the distance from the camera to the plume must be known. In a similar way, Porter and Cao (2009) used feature tracking techniques to determine cloud distance and position when measuring wind fields above the Mauna Loa Weather Observatory. Kern et al. (2013) measured SO_2 fluxes at Kīlauea volcano and assumed a known distance between the camera and the plume.

4.2. Instrument Configuration and Inversion Algorithm

The Thermal Hyperspectral Imager (THI) (Wright et al. 2013; Gabrieli et al. 2016) was employed at the summit of Kīlauea volcano between 07/24 and 07/26 2017 to obtain SO_2 path-concentration plume images and derive SO_2 fluxes. THI consists of a Sagnac interferometer and an uncooled microbolometer (a FLIR Photon 320) in rapid scanning configuration to collect hyperspectral images (Lucey et al. 2008). THI is capable of acquiring moderate spectral resolution images (40 cm^{-1}) from which SO_2 emission and absorption spectra can be retrieved. A spectrum containing 50 samples between 8 μm and 14 μm is available at each pixel in the resulting image cube. Images are radiometrically calibrated using two blackbodies at 20 °C and 70 °C and spectrally calibrated with an IR lamp with a 9.75 μm narrow band filter (Gabrieli et al. 2016). The THI spectral radiance measurements can be converted into SO_2 path-concentrations by employing the SO_2 Amenable Lookup Table Algorithm (SO_2–ALTA), a newly developed inversion code for gas species retrievals from hyperspectral images (Gabrieli et al. 2017).

The SO_2 Amenable Lookup Table Algorithm (SO_2–ALTA) uses the MODTRAN5 radiative transfer model to compute radiance for a variety (millions) of plume and atmospheric conditions. These include: SO_2 plume gas concentrations, plume sizes, plume locations, viewing geometries, and atmospheric conditions that occur at the summit of Kīlauea volcano, in Hawai'i, and in analog tropical volcanic scenarios. Rather than searching this lookup table to find the best fit for each measured spectrum (computationally intensive), the library was used to train a Partial Least Square Regression (PLSR) model. The PLSR coefficients are used to invert measured radiance spectra to path-concentration. SO_2–ALTA is a fast and efficient inversion, designed for single point SO_2 retrievals with cloud free or cloudy background. To validate this approach, THI measurements of sky radiance were collected using gas cells filled with various known SO_2 gas concentrations to replicate a volcanic plume. The performance of this new algorithm was thoroughly evaluated under clear, cloudy, and partly cloudy sky background condition and its results were compared with existing SO_2 inversion algorithms using well calibrated laboratory and field experiments (Chapter 3, Gabrieli et al. 2017).

4.3. Spatial Correlation-Based Feature Tracking Algorithm to Obtain the Velocity of the Plume

In order to determine volcanic gas flux rates, a method is needed to derive wind speed from plume motion. By knowing the plume-camera distance and the camera angular calibration, it is possible to derive plume wind speeds using a spatial correlation-based feature tracking algorithm and the THI hyperspectral frames (Figure 4.1a).

Plume transport speed was derived by tracking the motion of plume features seen in sequential hyperspectral image frames, which are N frames apart (N was set to 20, 23, 26, 29, and 31) and were acquired at 30 Hz. Six template boxes were used for this purpose. The boxes were defined for each frame and were squares with sides 45 pixels long. The algorithm determines the length of motion vectors by tracking how features move in each of the six template boxes using a correlation threshold of 0.4. When converting plume motion into wind speeds, the motion of the THI scanner was accounted for. Median wind speeds were considered. In regions where trees or no plume features were present, it was not possible to derive valid wind speeds. Only the frames with trackable plume features allowed wind speed derivation (Figure 4.1b). By using this procedure, it was possible to obtain estimated errors on the plume velocity less than 25% in case the motion of the plume was perpendicular to the central line sight of the observing camera.

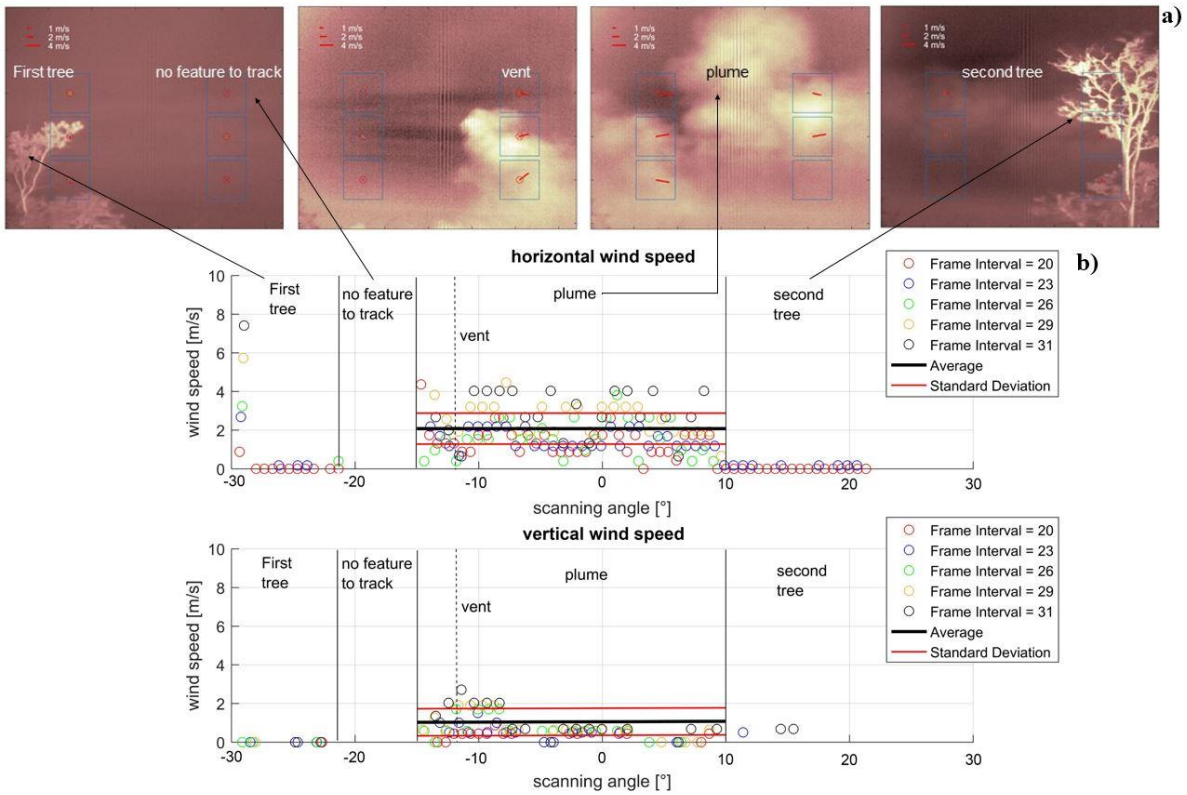

Figure 4.1. a) Wind speeds were derived by tracking the motion of plume features seen in sequential hyperspectral image frames that are N frames apart (N was set to 20, 23, 26, 29, and 31). In converting cloud motion into wind speeds, the motion of the THI scanner was accounted for. **b)** Median wind speeds plotted vs THI scanning (viewing) angle. In regions where trees or no plume features were present, it is not possible to derive valid wind speeds. Only the frames with trackable plume features allowed wind speed derivation. Plume velocity errors of less than 25% can be obtained using this procedure if the measured wind speed is compared to measurements carried out at a National Weather Station-maintained weather station in Volcano Village, HI.

Ideally, the plume motion should be perpendicular to the central line sight of the camera. If the motion of the plume is not perpendicular to the central line sight of the observing camera, then an angular correction is applied. Figure 4.2 shows a theoretical simulation of how the error on the plume transport speed changes with the angle between the plume motion direction and the central line sight of the sensor. If such plume-camera angle is less than 20 degrees or larger than 160 degrees, then the algorithm does not perform effectively as errors become increasingly large.

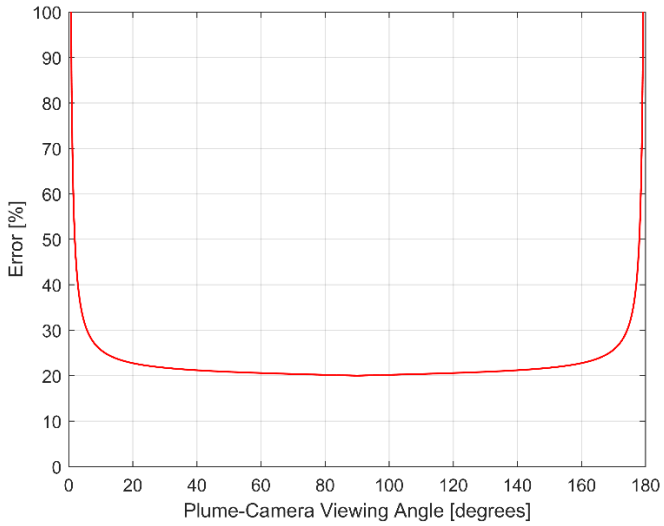

Figure 4.2. Simulation of how the wind speed error varies with the plume-camera angle.

4.4. Measurement Methodology

Time series THI images containing plume radiance were carried out with THI on the summit of Kīlauea volcano during two different field testing campaigns. The first one was carried out on July 24-26, 2017 and the second one on February 5-6, 2018. In July 2017, the weather was characterized by standard Hawaiian Northeasterly trade winds and clear sky conditions. In February 2018, weather conditions consisted of low and variable Southwesterly (Kona) winds and cloudy sky conditions. THI image data cubes were acquired every two minutes. The frames within each data cube were used to retrieve plume transport speed. Every data cube was then processed using SO_2-ALTA and SO_2 path-concentrations were derived for each pixel in the final image. In order to derive a mass flux, it was necessary to sum each path-concentration value along a closed line above the vent (displayed in red in Figure 4.3) and then multiplying the sum by the perpendicular plume velocity, both vertical and horizontal, that was derived for each hyperspectral image cubes. The resulting time series have both SO_2 flux and wind speed (vertical and horizontal) data points every 2 minutes.

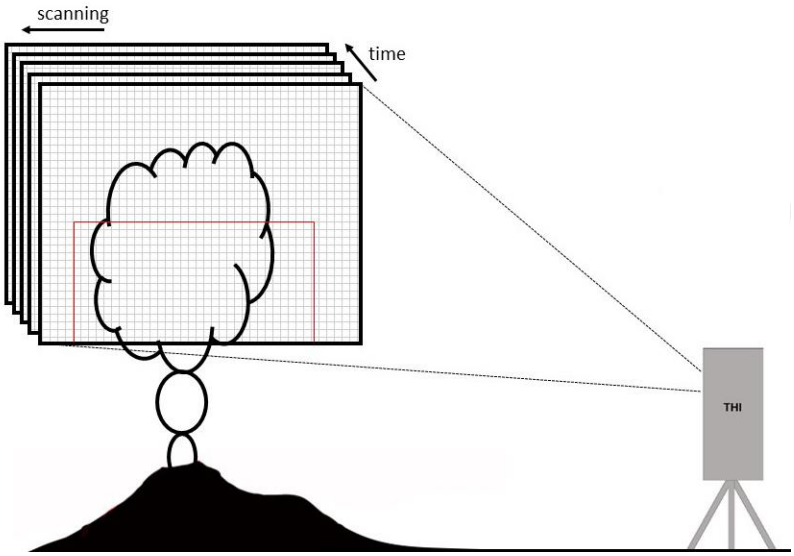

Figure 4.3. Schematics of how a mass flux can be obtained from the THI images.

Figure 4.4 shows various sequential SO_2-ALTA processed THI images of the volcanic plume acquired on 07/26/2017 during clear sky conditions. Figure 4.5 shows various sequential SO_2-ALTA processed THI images of the volcanic plume acquired on 07/26/2017 during cloudy sky conditions. The images were acquired every 2 minutes and were used to derive SO_2 fluxes

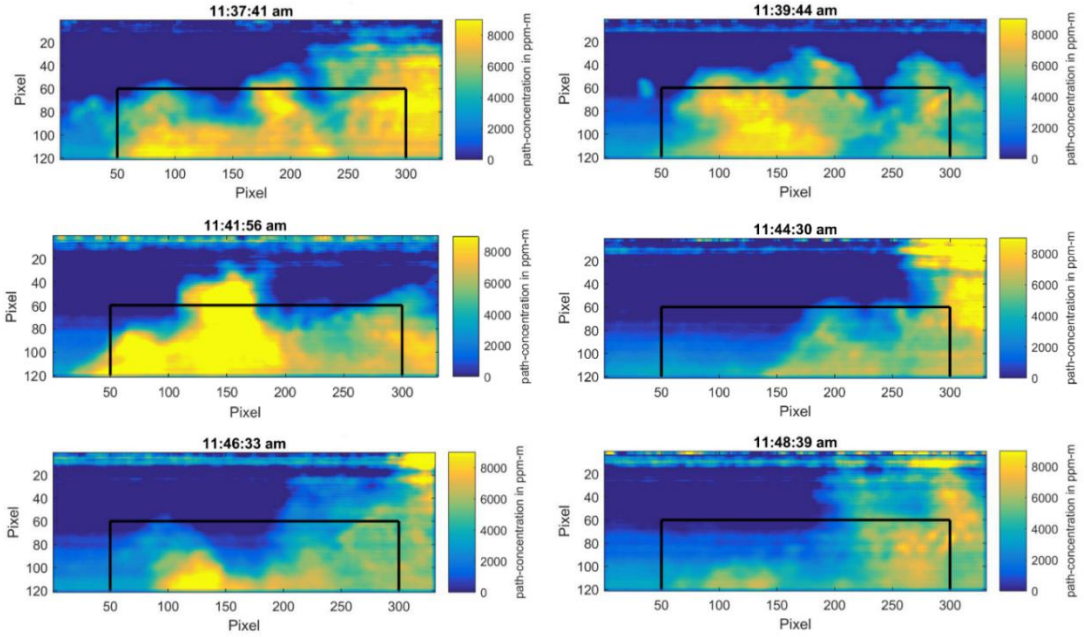

Figure 4.4. Sequential SO_2-ALTA processed THI images of the volcanic plume acquired on 07/26/2017. The images were acquired every 2 minutes and were used to derive SO_2 fluxes. X and Y axes plume velocities were used in the calculations respectively for the vertical path sections and the horizontal ones. The color-bar indicates the retrieved SO_2 path-concentrations and the black line above the vent is the line along which fluxes, which cross the line, ware calculated.

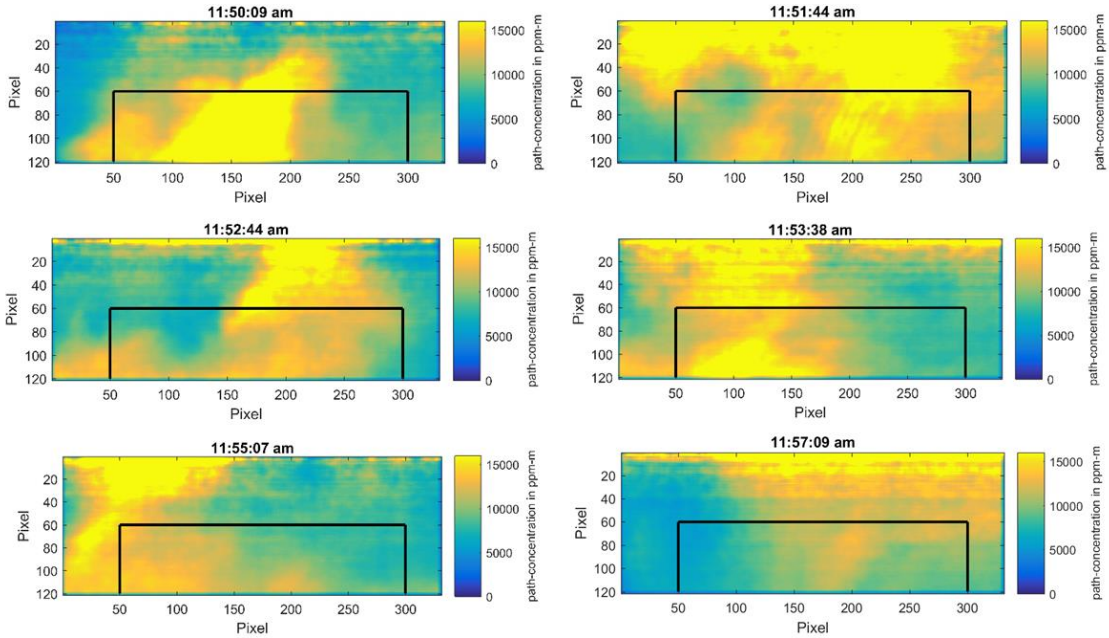

Figure 4.5. Sequential SO_2-ALTA processed THI images of the volcanic plume acquired on 02/6/2018. The images were acquired every 2 minutes and were used to derive SO_2 fluxes. X and Y axes plume velocities were used in the calculations respectively for the vertical path sections and the horizontal ones. The color-bar indicates the retrieved SO_2 path-concentrations and the black line above the vent is the line along which fluxes, which cross the line, ware calculated.

4.5. THI-derived SO_2 mass flux

Figure 4.6 shows an example of a 1 hour long time series of THI measurements of the volcanic plume, which were collected every two minutes. The time series was obtained on 07/24/2017 as the sun was setting. SO_2 flux, horizontal, and vertical wind speed are shown respectively in Figures 4.6a, 4.6b, and 4.6c. It can be seen that the usual structure of the Kīlauea's SO_2 flux time series, characterized by the repetition of medium-amplitude (<20 kg/s) gas flux oscillations produced by emission of single gas puffs (Kern et al. 2015), was captured by the THI sensor. Figure 4.6b illustrates a comparison between plume transport speed measurements obtained every 2 minutes by THI (the red line) and wind speed measurements acquired every 30 minutes by the Volcano Village weather station of the National Weather Service (NWS) network for the same time of the THI measurements. The decrease in wind speed, caused by the common (for this location) sea-land day-night wind inversion pattern, was captured by THI.

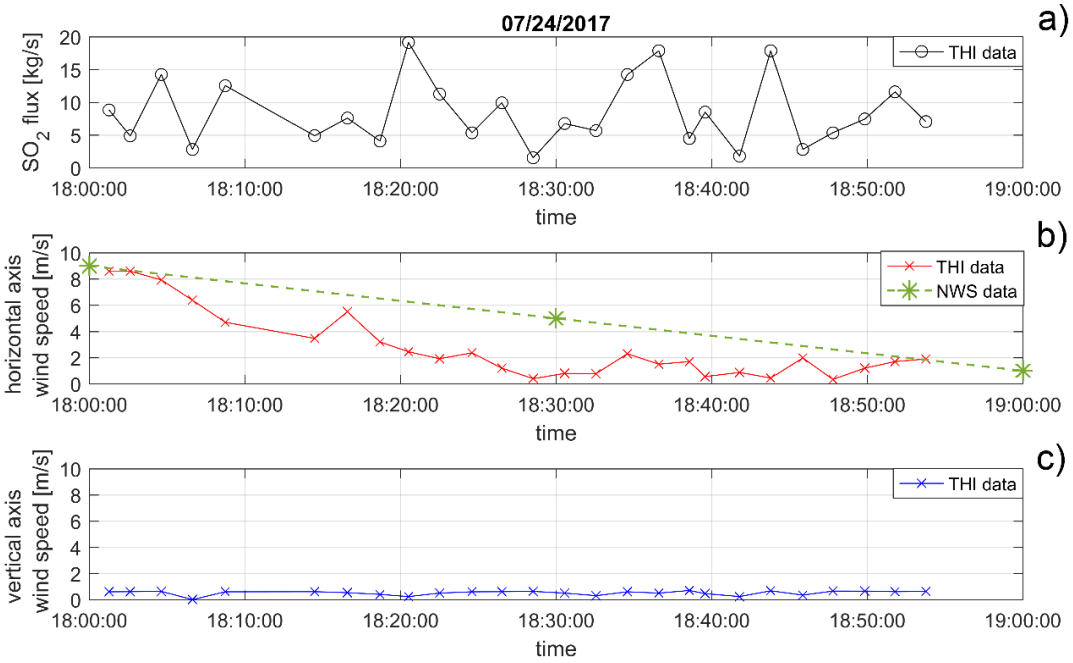

Figure 4.6. 1 hour time series of THI measurements of the volcanic plume obtained at sunset on 7/24/2017. **a)** The THI-derived SO_2 flux in kg/s. **b)** Comparison between the horizontal wind speed measurements obtained respectively from THI (the red line) and from the Volcano Village weather station from the National Weather Service for the same time of the THI measurements (the green dotted line). **c)** THI-derived vertical plume speed.

Figure 4.7 shows a nighttime 1 hour time series of THI measurements of the volcanic plume, which was collected on the evening of 07/25/2017. Figure 4.7b shows a comparison between the plume velocity derived from the THI hyperspectral frames (the red line) and wind observations obtained from aforementioned weather station (the green dotted line). The THI-derived wind speed is characterized by pulses, which are not present in the wind speed measurements obtained from the National Weather Service's weather station. The agreement in this case is poor.

Figure 4.8 shows a daytime example of time series of THI measurements of SO_2 flux, horizontal, and vertical wind speed at Kīlauea volcano. The time series was obtained on 07/26/2017 under very windy, occasionally gusty, conditions. Again, the classical structure of Kīlauea's SO_2 pulsing flux (Kern et al. 2015), was captured by the THI sensor. Figure 4.8b shows a comparison between the THI-derived horizontal 2 minutes interval wind speed (the red line) and 30 minutes interval wind speed measurements obtained from the Volcano Village weather station. In this case, the agreement between the two curves is good.

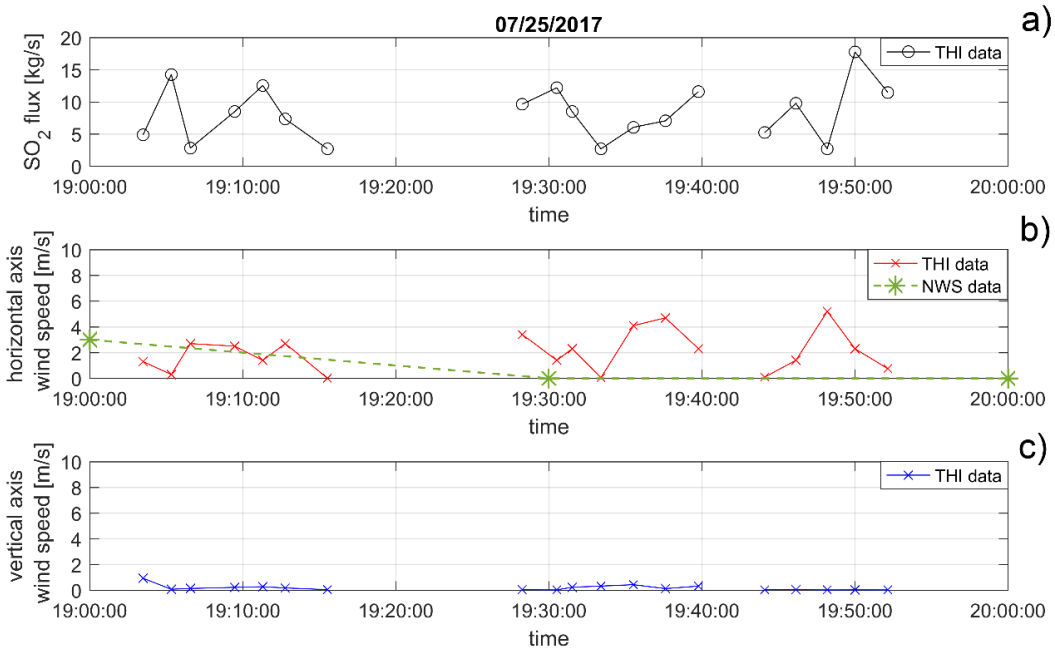

Figure 4.7. 1 hour long time series of THI measurements of the volcanic plume obtained during nighttime on 7/25/2017. **a)** The THI-derived SO_2 flux in kg/s. **b)** Comparison between the horizontal wind speed measurements obtained respectively from THI (the red line) and from the Volcano Village weather station from the National Weather Service for the same time of the THI measurements (the green dotted line). **c)** THI-derived vertical plume speed.

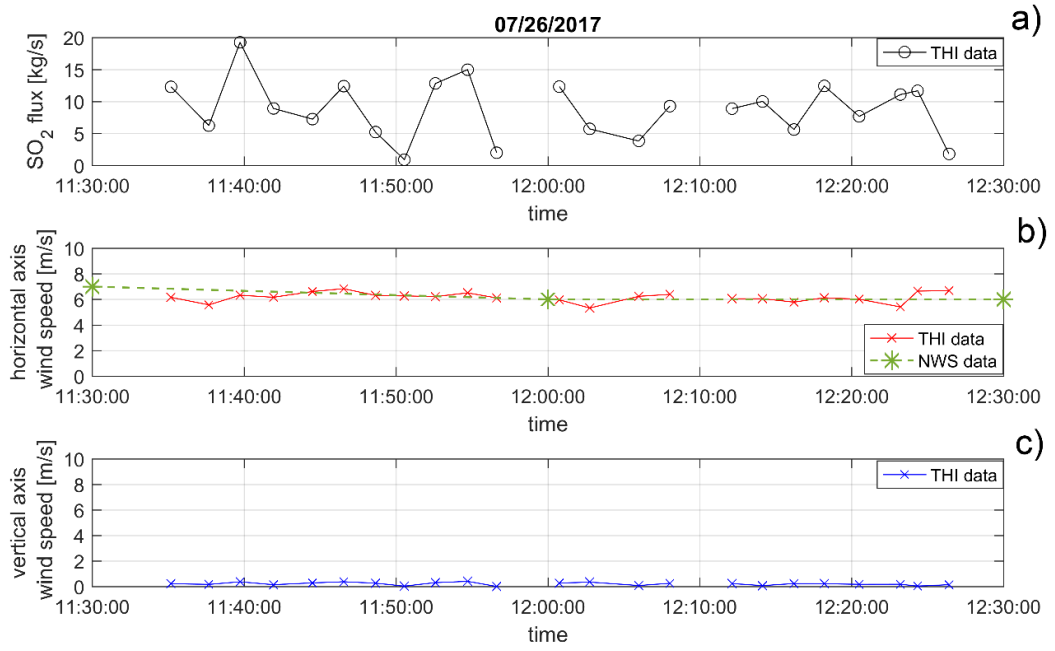

Figure 4.8. 1 hour long time series of THI measurements of the volcanic plume obtained during daytime on 7/26/2017. **a)** The THI-derived SO_2 flux in kg/s. **b)** Comparison between the horizontal wind speed measurements obtained respectively from THI (the red line) and from the Volcano Village weather station from the National Weather Service for the same time of the THI measurements (the green dotted line). **c)** the THI-derived vertical plume speed.

Figure 4.9a shows a longer time series of THI SO_2 flux measurements of the volcanic plume, acquired on 02.05/18. Here, a weighted average line was added to better illustrate the SO_2 flux trend overtime. It can be seen that one major peck higher than 20 kg/s occurred shortly after noon, Hawai'i Standard

Time. In this case, the THI-measured SO_2 flux time series was compared with ground shaking amplitude measurements carried out at the Halema‘uma‘u vent by the Hawaiian Volcano Observatory of the US Geological Survey and shown in Figure 4.9b. It can be seen that the anomalous flux peak, higher than 20 kg/s, occurred at the same time of an increase in the measured ground shaking amplitude. This illustrates that the observed peak in SO_2 flux is probably related to the activity of the lava lake present in the Halema‘uma‘u vent.

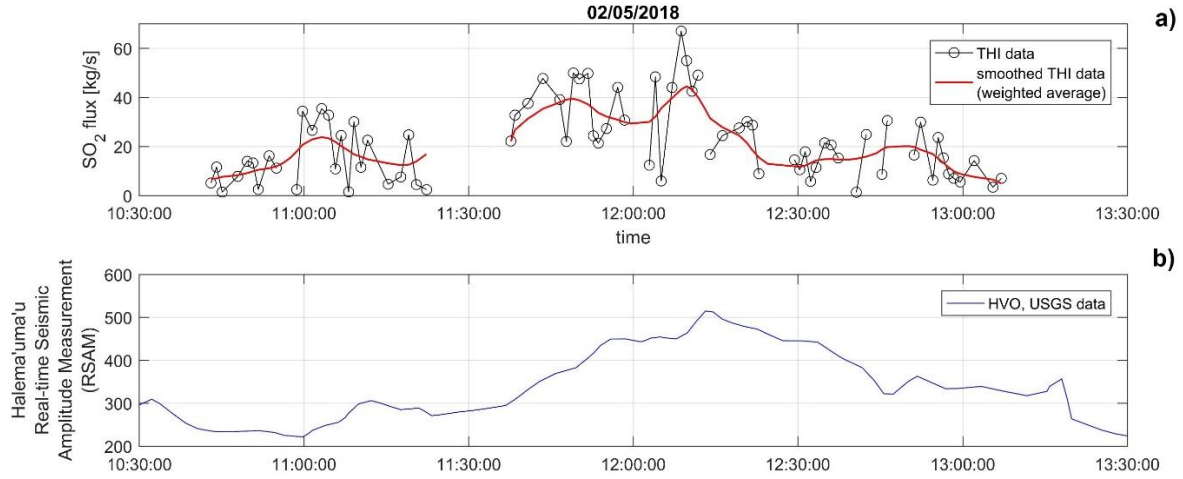

Figure 4.9. a) 4 hour time series of SO_2 flux THI measurements in kg/s of the volcanic plume obtained during daytime on 02/05/2018. **b)** The Real-time Seismic Amplitude Measurement (RSAM) from the active Halema‘uma‘u vent measured by the Hawaiian Volcano Observatory of the US Geological Survey.

4.6. Summary and discussion

SO_2 flux measurements are needed for both volcanic eruption forecast and public health (EPA, 2011). This arduous task requires accurate plume velocity measurements. Classically, plume motion velocity estimation is carried out by using anemometers located from a few meters above ground to often several km away from the plume (Mc Gonigle et al. 2005). This significantly complicates the measurements and their processing as uncertainty on the true plume velocity can sometimes be as large as 100% (Mc Gonigle et al. 2005). Furthermore, plume transport motion measurements carried out at anemometer heights can vary dramatically from those which could be observed a few hundred meters above the surface (Archer and Jacobson, 2003) and volcanic topography may further increase such discrepancies (e.g., Favalli et al. 2004).

Here, we presented measurements of volcanic SO_2 mass flux obtained at Kīlauea volcano during July 2017 and February 2018 under different weather conditions at the summit of Kīlauea volcano. The plume transport speed was estimated by using the sequential hyperspectral frames, acquired at 30 Hz by a novel hyperspectral uncooled imaging spectrometer, the Thermal Hyperspectral Imager (THI) (Wright et al. 2013; Gabrieli et al. 2016; and Gabrieli et al. 2017). Temporal trends of SO_2 flux were evaluated at different times of the day and the night by employing THI images and a newly developed SO_2 retrieval algorithm, the SO_2 Amenable Lookup Table Algorithm (SO_2-ALTA). The THI instrument was able to acquire sequential hyperspectral image frames at 30 Hz from which it is possible to derive wind speed in the volcanic plume by employing spatial correlation techniques to convert camera pixel motion into wind speed (i.e., Berryman 1985). This procedure was developed in order to avoid the standard and often large uncertainty prone practice of taking ground-based anemometer readings as proxies for plume velocity.

The test carried out here indicated that the proposed feature tracking algorithm can be successfully applied to derive plume velocity. The best case observing scenario for the proposed technique is that

the plume motion is perpendicular to the central line sight of the camera. If the motion of the plume is not perpendicular to the central line sight of the observing camera, angular corrections were applied. In the case of Kīlauea volcano, the needed corrections were determined easily as the wind directions are usually NW-SW. Particular care is needed if the angle between the central line sight of the camera and the plume motion direction cannot be determined accurately. In case of volcanoes with less consistent and practicable wind patterns, a system of stereo vision cameras might need to be implemented to accurately determine wind direction and speed.

CHAPTER *5*

CONCLUSION

Thermal IR hyperspectral imaging offers unique advantages for measuring volcanic plume emissions during both daytime and nighttime. Spectral absorption and emission features are present in the thermal IR for many gases, including SO_2, CO_2 and H_2O, and, with appropriate methods, it is possible to derive plume gas path-concentrations. This study focused on the potential for THI, a thermal IR hyperspectral imaging system – the Thermal Hyperspectral Imager–, to make SO_2 volcanic plume measurements. The sensor was characterized for measuring SO_2 gas path-concentrations in the second chapter. The third chapter dealt with testing existing dual view-based inversion algorithms for converting radiance measurements into SO_2 path-concentration as well as the development of a new Partial Least Squares Regression-based single point inversion technique. The fourth chapter presented sulfur dioxide flux measurements at Kīlauea, which is what volcanologists need, using the hyperspectral imaging technique, characterized and tested in the previous chapters.

THI employs a Sagnac interferometer and an uncooled microbolometer in rapid scanning configuration to collect hyperspectral images of volcanic plumes. Each pixel in the resulting image yields a spectrum with 50 samples between 8 μm and 14 μm. Images are spectrally and radiometrically calibrated using respectively an IR source with a narrow band filter and two blackbodies. THI is able to obtain measurements within the spectral region from 8 μm to 14 μm, which covers a SO_2 absorption and emission band (centered at 8.6 μm).

In the second chapter of this dissertation, the sensitivity of THI to measure SO_2 was determined using gas cells filled with known concentrations of SO_2 and using NIST-traceable blackbodies to simulate a range of realistic background conditions. To confirm the robustness of the THI measurements, THI data were benchmarked against those obtained from a commercial off-the-shelf non-imaging Michelson FTIR spectrometer. As part of this work, I showed that THI is able to detect SO_2 gas path-concentrations as low as 100 ppm-m with a background temperature of -10°C (i.e., somewhat ideal observation conditions, at night with a high elevation angle) and as low as 1 000 ppm-m with a background temperature of $+10$°C (i.e., much less ideal observations conditions, during the day, at low elevation angles). I also carried out studies where THI measurements were compared with theoretical thermal IR spectral radiances, computed with MODTRAN5 for the same optical conditions. A good agreement between THI measured and theoretical spectra under controlled conditions was shown.

THI was also field-tested at Kīlauea volcano, Hawai‘i by imaging the volcanic plume raising from the Halema‘uma‘u vent. The hyperspectral thermal IR data cube, collected by THI, was processed using a simplified MODTRAN5-based inversion algorithm based on measured spectral radiance ratio calculations between the averages of in plume and out of plume pixels. Spectra collected in and out of the plume were used to illustrate the SO_2 absorption-emission band. This SO_2 feature was modeled with MODTRAN5, using the same geometry and environmental conditions of the day of the measurements. A path-concentration of 7 150 ppm-m was retrieved from measurements made near the Halema‘uma‘u vent. This SO_2 path-concentration was within the range of those reported by Grutter et al. 2008, Elias and Sutton 2012, Kern et al. 2012, and Kern et al. 2013 at the Kīlauea volcanic plume.

After the sensitivity of the THI sensor to measure SO_2 was established, it was necessary to focus more on how to convert radiance measurements into path-concentrations. In fact, the inversion of SO_2 path-concentration using ground-based spectral TIR methods is complicated by emission and absorption processes within the plume, the background and the foreground regions. Existing algorithms use spectra collected in and out of the plume to illustrate the SO_2 absorption-emission band and they were referred to as dual view approaches. Dual-view approaches suffer from a variety of issues, which limit their usefulness in SO_2 retrievals. These issues are the assumption of clear sky background conditions and the plume distance effect. The process of comparing regions in and out of the plume assumes the background

sky is homogeneous. In fact, cloudy backgrounds drastically reduce their performance. This was the topic of chapter 3.

In the first part of chapter 3, two dual-view algorithms were validated using TIR measurements with gas cells to provide realistic and known path-concentrations of SO_2. Both clear and cloudy background conditions were tested. In the second part of chapter 3, a new inversion algorithm, SO_2-ALTA, which is capable of single point SO_2 path-concentration retrievals, was introduced. SO_2–ALTA employs a PLSR model that was trained using MODTRAN5 spectral radiance look-up table calculations for a variety of plume and atmospheric conditions. The performance of SO_2–ALTA was similar to those of the two dual-view approaches under clear sky conditions, but much better under cloudy background conditions.

Chapter 4 dealt with obtaining sulfur dioxide flux measurements using the hyperspectral imaging technique and the single point inversion technique, characterized and tested in the two previous chapters. The advantage of the imaging technique is to have synoptic views of the plume. This was used to obtain accurate plume velocity measurements by using the sequential hyperspectral frames, acquired at 30 Hz by THI. Temporal trends of SO2 flux at Kīlauea were evaluated at different times of the day and the night by employing THI images and SO2-ALTA. The THI instrument was able to acquire sequential hyperspectral image frames at 30 Hz from which it is possible to derive wind speed in the volcanic plume by employing spatial correlation techniques to convert camera pixel motion into wind speed. This procedure was developed in order to avoid the standard and often large uncertainty prone practice of taking ground-based anemometer readings as proxies for plume velocity.

The test, reported in chapter 4, showed that the proposed feature tracking algorithm can be successfully applied to derive plume velocity. The best case observing condition for the proposed technique is that the plume motion is perpendicular to the central line sight of the camera. If the motion of the plume is not perpendicular to the central line sight of the observing camera, angular corrections were applied. In the case of Kīlauea volcano, the needed corrections were determined easily as the wind directions are usually NW-SW. Particular care is needed if the angle between the central line sight of the camera and the plume motion direction cannot be determined accurately. In case of volcanoes with less consistent and practicable wind patterns, a system of stereo vision cameras might need to be implemented to accurately determine wind direction and speed.

The study carried out and summarized in this dissertation suggests that thermal IR hyperspectral imaging can be successfully employed to image volcanic plumes and derive SO_2 path concentrations, which in turn can be converted into mass flux. The single point retrieval algorithm, presented in this study, is currently limited to tropical atmospheres as it was trained using Hawai‘i and Puerto Rico soundings, but it would be simple to expand its geographic applicability by building appropriate MODTRAN databases to train additional PLSR models.

Future studies using PLSR may also include different training techniques for these inversion algorithms, such as Neural Network. Additionally, more SO_2-ALTA models may be created to account for observations carried out from air-borne sensors or satellites. These new models may be trained with emissivity spectra for different kind of background (i.e., rocks and vegetation) at various temperatures. Additional models may be created for other volcanic gases of interest, such as CO_2, or volcanic ash.

REFERENCES

Abdi, H. (2010). "*Partial least squares regression and projection on latent structure regression (PLS-Regression)*". Wiley Interdisciplinary Reviews: Computational Statistics. 2: 97–106. doi:10.1002/wics.51.

Aiuppa, A., Moretti, R., Federico, C., Giudice, G., Gurrieri, S., Liuzzo, M., Papale, P., Shinohara, H., Valenza, M. (2007). Forecasting Etna eruptions by real-time observation of volcanic gas composition. Geology, vol. 35, issue 12, p. 1115. doi: 10.1130/G24149A.

Allard, P., Carbonnelle, J., Me´trich, N., Loyer, H., Zettwoog P. (1994) "*Sulphur output and magma degassing budget of Stromboli volcano"*, Nature, 368, 326 – 330, doi:10.1038/368326a0.

Allard, P., Aiuppa, A., Beatuducel, F., Gaudin, D., Di Napoli, R., Calabrese, S., Parello, F., Crispi, O., Hammouya, G., Tamburello, G. (2014) "*Steam and gas emission rate from La Soufriere volcano, Guadeloupe (Lesser Antilles): Implications for the magmatic supply during degassing unrest*" Chemical Geology 384: 76-93.

Anderson, G.P., Berk, A., Acharya, P.K., Bernstein, L.S., Adler-Golden, S.M., Lee, J., Muratov, L. (2009) "*Reformulated Atmospheric Band Model Method for Modeling Atmospheric Propagation at Arbitrarily Fine Spectral Resolution and Expanded Capabilities*," U.S. Patent #7593835, issued September 22, 2009.

Anderson, K., Segall, P. (2013). *Bayesian inversion of data from effusive volcanic eruptions using physics-based models: Application to Mount St. Helens 2004-2008*, Journal of Geophysical Research, 118 (5), 20 pp., doi:10.1002/jgrb.50169

Archer, C. L., and Jacobson M. Z. (2003), Spatial and temporal distributions of U.S. winds and wind power at 80 m derived from measurements, J. Geophys. Res., 108(D9), 4289, doi:10.1029/2002JD002076.

Asimow, P.D. (2000). *Melting the mantle.* Published in: Sigurdsson, H., Houghton, B., McNutt, S.R., Rymer, H., Stix, J., *Encyclopedia of Volcanoes.* Academic Press, 55-68.

Baxter, P.J., Gresham, A. (1997). *Deaths and injuries in the eruption of Galeras volcano, Colombia, 14 January 1993.* Journal of Volcanology and Geothermal Research 77: 325-338

Baxter, P.J. (1999) "*Impacts of Eruptions on Human Health*". Published in: Sigurdsson, H., et al (eds.) Encyclopedia of Volcanoes. San Diego: Academic Press. 1035-1043.

Berlo, K., Tuffen, H., Smith, V.C., Castro, J.M., Pyle, D.M., Mather, T.A., Geraki, K. (2003). *Element variations in rhyolitic magma resulting from gas transport.* Geochimica et Cosmochimica Acta 121: 436-451

Berk, A., Acharya, P.K., Bernstein, L.S., Anderson, G.P., Lewis, P., Chetwynd, J.H., Hoke, H.L. (2008). *Band Model Method for Modeling Atmospheric Propagation at Arbitrarily Fine Spectral Resolution.* U.S. Patent #7433806, issued October 7, 2008.

Berryman, J.G. (1985). Measurement of Spatial Correlation Functions Using Image Processing Techniques. Journal of Applied Physics. Volume 57, Number 7. Pages 2374-2384

Bluth, G.J.S., Shannon, J.M., Watson, I.M., Prata, A.J., Realmuto, V.J. (2007) *Development of an ultra-violet digital camera for volcanic SO2 imaging.* Journal of Volcanology and Geothermal Research 161 (2007) 47–56

Campion, R. (2014). *New lava lake at Nyamuragira volcano revealed by combined ASTER and OMI SO_2 measurements.* Geophysical Research Letters 41: 7485-7492

Carn, S.A., Krueger, A.J., Bluth, G.J.S., Schaffer, S.J., Krotkov, N.A., Watson, I.M., Datta, S. (2003). *Volcanic eruption detection by the Total Ozone Mapping Spectrometer (TOMS) instruments: a 22-year record of sulfur dioxide and ash emissions.* Published in: Oppenheimer, C., Pyle, D.M., Barclay, J., *Volcanic degassing*. Geological Society, London, Special Publications 213: 177-202

Castro, J.M., Bindeman, I.N., Tuffen, H., Schipper, C.I. (2014). *Explosive origin of silicic lava: textural and δ D –H_2O evidence for pyroclastic degassing during rhyolite effusion.* Earth and Planetary Science Letters 405: 52-61

Collins, W.D., Hackney, J.K., Edwards, D.P., (2002). "*An updated parameterization for infrared emission and absorption by water vapor in the National Center for Atmospheric Research Community Atmosphere Model*". Journal of Geophysical Research. doi:10.1029/2001JD001365, 2002

Cramer, C.E., Woodward IV, J.T., Lykke, K.R., Stubbs, C.W., Vaz, A., Fraser, G.T. (2015). "*A Comparison of MODTRAN5 Atmospheric Extinction Predictions with Narrowband Astronomical Flux Observations*". Proc. SPIE 9608, Infrared Remote Sensing and Instrumentation XXIII, 96080R; doi:10.1117/12.2188453

Daag, A.S., Tubianosa, B.S., Newhall, C.G., Tuñgol, N.M., Javier, D., Dolan, M.T., Reyes, P.J.D., Arboleda, R.A., Martinez, M.M.L., Regalado, T.M. (1996). *Monitoring sulphur dioxide emission at Mount Pinatubo.* [Online] Available at: < http://pubs.usgs.gov/pinatubo/daag1/>, [Accessed on 11/3/2014]

Dalton, M.P., Watson, I.M., Nadeau, P.A., Werner, C., Morrow, W., Shannon, J.M. (2009) *Assessment of the UV camera sulfur dioxide retrieval for point source plumes.* Journal of Volcanology and Geothermal Research 188 (2009) 358–366

De Boer, J.Z., Hale, J.R., Chanton, J. (2001). *New evidence for the geological origins of the ancient Delphic oracle (Greece).* Geological Society of America, Geology 29: 707-710

Demirgian, J., Dedecker, R. (2005). *Atmospheric Emitted Radiance Interferometer (AERI) handbook. ARMTR-054.* [Online]. Available at: <http://www.arm.gov/publications/tech_reports/handbooks/>

Doukas, M.P., Gerlach, T.M. (1995). *Sulfur dioxide scrubbing during the 1992 eruption of Crater Peak, Mount Spurr volcano, Alaska.* Published in: Keith, T.E.C., *The 1992 eruptions of Crater Peak vent, Mount Spurr volcano, Alaska.* US Geological Survey Bulletin B-2139: 47-57

Duncan, M.S., Dasgupta, R. (2013). *CO_2 solubility and speciation in rhyolitic sedimental partial melts at 1.5-3.0 GPa. Implications for carbon flux in subduction zones.* Geochimica et Cosmochimica Acta 124: 328-347

Düzgün, H.Ş., Demirel, N. (2011). *Remote sensing of the mine environment.* CRC Press

Edmonds, M., Herd R. A., Galle B., and Oppenheimer C. M. (2003), Automated, high time-resolution measurements of SO2 flux at Soufrière Hills Volcano, Montserrat, Bull. Volcanol., 65, 578–586, doi:10.1007/s00445-003-0286-x.

Edmonds, M. (2008). *New geochemical insights into volcanic degassing.* Philosophical transactions of the Royal Society A, London 366: 4559-4579

Elias, T., Sutton, A.J. (2012). Sulfur dioxide emission rates from Kīlauea Volcano, Hawai'i, 2007–2010: U.S. Geological Survey Open-File Report 2012–1107, 25 p. (Available at <http://pubs.usgs.gov/of/2012/1107/>.)

EPA, *National Ambient Air Quality Standards (NAAQS)*, 2011 [Online], Available at https://www.epa.gov/ttn/naaqs/criteria.html

ESRL-NOAA. (2014). *Trends in atmospheric carbon dioxide.* [Online] Available at: < http://www.esrl.noaa.gov/gmd/ccgg/trends/global.html>, [Accessed on 10/15/2014]

Exton, J.R., US National Aeronautics and Space Administration (1976) *Stack Plume Visualization System*, U.S. Pat. 3931462.

Favalli, M., Mazzarini F., Pareschi M. T., and Boschi E. (2004), *Role of local wind circulation in plume monitoring at Mt. Etna volcano (Sicily): Insights from a mesoscale numerical model*, Geophys. Res. Lett., 31, L09105, doi:10.1029/2003GL019281.

Fellgett, P.B. (1949) *On the ultimate sensitivity and practical performance of radiation detectors. J. Opt. Soc. Am. (OSA) 39 (11): 970–976.*

Ferrec, Y., Taboury, J., Sauer, H., Chavel, P. (2006). *Optical geometry for Sagnac and Michelson interferometers used as spectral imagers.* Optical Engineering 45: 115601

Fisher, T.P. (2008). *Fluxes of volatiles (H_2O, CO_2, N_2, Cl, F) from arc volcanoes.* Geochemical Journal 42: 21-38

Foster, J., Bevis, M., Raymond, W. (2006) *Precipitable water and the lognormal distribution.* J. Geophys. Res., 111, D15102, doi:10.1029/2005JD006731.

Francis, P., Maciejewski, A., Oppenheimer, C., Chaffin, C. (1996). *New methods make volcanology research less hazardous.* Eos, Transactions American Geophysical Union 77, 396-397

Francis, P, M. Burton, C. Oppenheimer. (1998) *Remote measurements of volcanic gas compositions by solar occultation spectroscopy.* Nature. 396, 567-570.

Francis, P., Horrocks, L., Oppenheimer, C. (2000). *Monitoring gases from andesite volcanoes.* Philosophical transactions of the Royal Society A, London 358: 1567-1584

Francis, P., Oppenheimer, C. (2004). *Volcanoes – second edition.* Oxford University Press

Freeth, S.J. (1992). *The Lake Nyos gas disaster.* Published in: Freeth, S.J., Ofoegbu, C.O., Onuoha, K.M., *Natural hazards in West and Central Africa.* International Monograph Series: 63-82

Gabrieli, A., L. Wilson, S. Lane. (2015). *Volcano-Tectonic Interactions as Triggers of Volcanic Eruptions.* Journal of the Geologists' Association, UK. DOI: 10.1016/j.pgeola.2015.10.002

Gabrieli, A., R. Wright, P.G. Lucey, J.N. Porter, H. Garbeil, E. Pilger, M. Wood. (2016). *Characterization and initial field test of a long wave thermal infrared hyperspectral imager for measuring SO2 in volcanic plumes.* Bulletin of Volcanology, DOI: 10.1007/s00445-016-1068-6.

Gabrieli, A., R. Wright, J.N. Porter, and P.G. Lucey. (2017). *Validating the accuracy of SO2 gas retrievals in the thermal infrared (8–14 μm).* Bulletin of Volcanology, DOI: DOI 10.1007/s00445-017-1163-3.

Galle, B., Oppenheimer, C., Geyer, A., McGonigle, A.J.S., Edmonds, M., Horrocks, L. (2002) *A miniaturised ultraviolet spectrometer for remote sensing of SO2 fluxes: a new tool for volcano surveillance.* Journal of Volcanologyand Geothermal Research 119 (2002) 241-254

Galle, B., Johansson, M., Rivera, C., Zhang, Y., Kihlman, M., Kern, C., Lehmann, T., Platt, U., Arellano, S., Hidalgo, S. (2010). *Network for observation of volcanic and atmospheric change (NOVAC) – a global network for volcanic gas monitoring: network layout and instrument description.* Journal of Geophysical Research 115: D05304

Genda, H., Hamano, K., Abe, Y. (2013). *Formation and early evolution of atmosphere and ocean on the Earth.* International Astrobiology Workshop

Gerlach, T.M. (1986). *Exsolution of H_2O, CO_2 and S during eruptive episodes at Kīlauea volcano, Hawai'i.* Journal of Geophysical Research 91: 12.177-12.185

Gerlach, T.M., Casadevall, T.J. (1986). *Evaluation of gas data from high temperatures fumaroles at Mount St. Helens, 1980-1982.* Journal of Volcanology and Geothermal Research 28: 107-140

Gerlach, T.M. (1991). Etna's greenhouse pump. Nature 351: 352-353

Gerlach, T.M. (1993a). *Oxygen buffering of Kīlauea volcanic gases and the oxygen fugacity of Kīlauea basalt.* Geochimica et Cosmochimica Acta 57: 795-814

Gerlach, T.M. (1993b). *Thermodynamic evaluation and restoration of volcanic gas analyses: an example based on modern collection and analytical methods.* Geochemical Journal 27: 305-322

Gerlach, T. M., McGee K. A., Sutton A. J., and Elias T. (1998), Rates of volcanic CO2 degassing from airborne determinations of SO2, emission rates and plume CO2/SO2: Test study at Pu'u 'O'o cone, Kīlauea volcano, Hawaii, Geophys. Res. Lett., 25, 2675–2678.

Giambelluca, T.W., Chen, Q., Frazier, A.G., Price, J.P., Chen, Y.-L., Chu, P.S., Eischeid, J.K., Del Parte, D.M. (2013). *Online Rainfall Atlas of Hawai'i.* Bulletin of the American Meteorological Society 94: 313-316

Giggenbach, W.F. (1975). *A simple method for the collection and analysis of volcanic gas samples.* Bulletin of Volcanology 39: 15-27

Giggenbach, W.F. (1983). *Chemical surveillance of active volcanoes in New Zealand.* Published in: Tazieff, H., Sabroux J.C., *Forecasting volcanic events.* Elsevier: 311-322

Giggenbach, W.F., Goguel, R.L. (1989). *Collection and analysis of geothermal and volcanic water and gas discharges.* DSIR Chemistry Report CD 2401\

Giggenbach, W.F. (1987). *Redox processed governing the chemistry of fumarolic gas discharges from White Island, New Zealand.* Applied Geochemistry 2: 143-161

Giggenbach, W.F., Matsuo, S. (1991). *Evaluation of results from second and third IAVCEI field workshops on volcanic gases, Mt Usu, Japan and White Island, New Zealand.* Applied Geochemistry Journal 6: 125-141`

Giggenbach, W.F. (1996). *Chemical composition of volcanic gases.* Published in: Scarpa, R., Tilling, R.I., *Monitoring and mitigation of volcano hazards.* Springer-Verlag: 221-256

Goff, F., Love, S.P., Warren, R.G., Counce, D., Obenholzner, J., Siebe, C., and Schmidt, S.C. 2001. *Passive infrared remote sensing evidence for large, intermittent CO2 emissions at Popocatépetl Volcano, Mexico.* Chemical Geology 177, 133-156.

Grahn, H.F., Geladi, P. (2007). *Techniques and applications of hyperspectral image analysis.* Wiley

Grezechnik, A., Mc Millan, P.F. (1998). *Temperature dependence of the OH absorption in SiO_2 glass and melt to 1975 K.* American Mineralogist 83: 311-338

Griffith, D. 2012. Matlab Class Wrapper for Modtran5. Matlab File Exchange [Online] Available at: <http://www.mathworks.com/matlabcentral/fileexchange/31961-matlab-class-wrapper-for-modtran-5>

Gritschneder, M., Lin, D.N.C., Murray, S.D., Yin, Q.-Z., Gong, M.-N. (2011). *The supernova triggered formation and enrichment of our Solar System.* [Online] Available at: <http://www.usm.uni-muenchen.de/~gritschm/Gritschneder_2011_sun.pdf>, [Accessed on 10/13/2014]

Grutter, M., Basaldud, M., Rivera, C., Harig, R., Junkerman, W., Caetano, E., Delgado-Granados, H. (2008). SO_2 emissions from Popocatepetl volcano: emission rates and plume imaging using optical remote sensing techniques. Atmos. Chem. Phys., 8, 6655–6663

Halliday, A.N. (2013). *The origins of volatiles in the terrestrial planets.* Geochimica et Cosmochimica Acta 105: 146-171

Hamilton, D.L., Burnham, C.W., Osborn, E.F. (1964). *The solubility of water and effects of oxygen fugacity and water content on crystallization in mafic magmas.* Journal of Petrology 5: 21-39

Hards, V. (2005). *Volcanic contributions to the Global Carbon Cycle.* British Geological Survey

Head, J.W., Wilson, L. (1987). *Lava fountain heights at Pu'u 'O'o, Kīlauea, Hawai'i: indicators of amount and variations of exsolved magma volatiles.* Jorunal of Geophysical Research 92: 13715-13719

Holloway, J.R. (1976). *Fluid in the evolution of granitic magmas: consequences of finite CO_2 solubility.* Geological Society of America Bulletin 87: 1513-1518

Hooper, A., Prata, F., Sigmundsson, F. (2013). *Remote sensing of volcanic hazards and their precursors.* Proceedings of the IEEE 100: 2908-2930

Hort, M. (1997). *Abrupt change in magma liquidus temperature because of volatile loss or magma mixing: effects on nucleation, crystal growth and thermal history of the magma.* Journal of Petrology 39: 1063-1076

Horton, K.A., Williams-Jones, G., Garbeil, H., Elias, T., Sutton, A.J., Mouginis-Mark, P., Porter, J.N., Clegg, S. (2006). Real-time measurement of volcanic SO2 emissions: Validation of a new UV correlation spectrometer (FLYSPEC). DOI: 10.1007/s00445-005-0014-9

Hoskuldsson, P. (1988), *PLS Regression Methods*, Journal of Chemometrics, 2, 211-228.

Houghton, B.F., Wilson, C.J.N., Del Carlo, P., Coltelli, M., Sable, J.E., Carey, R. (2004). *The influence of conduit processes on changes in style of basaltic Plinian eruptions: Tarawera 1886 and Etna 122 BC.* Journal of Volcanology and Geothermal Research 123: 1-14

Jaupart, C. (2000). *Magma ascent at shallow levels.* Published in: Sigurdsson, H., Houghton, B., McNutt, S.R., Rymer, H., Stix, J., *Encyclopedia of Volcanoes.* Academic Press, 237-245.

Jeanloz, R. (2000). *Mantle of the Earth.* Published in: Sigurdsson, H., Houghton, B., McNutt, S.R., Rymer, H., Stix, J., *Encyclopedia of Volcanoes.* Academic Press, 41-54.

Jugo, P.J., Luth, R.W., Richards, J.P. (2005). *Experimental data on the speciation of sulfur as a function of oxygen fugacity in basaltic melts.* Geochimica et Cosmochimica Acta 69: 497-503

Kenyon, S.J., Bromley, B.C. (2006). *Terrestrial Planet Formation: The transition from oligarchic growth to chaotic growth.* Astronomical Journal 131, 1837-1850

Keppler, H. (1999). *Experimental evidence for the source of excess sulfur in explosive volcanic eruptions.* Science 284: 1652-1654

Kern, P., Werner, C., Sutton, J., Elias, T., Thelen, W., Kelly, P., Mastin, L. (2012). *Ultraviolet SO_2 imaging systems allow insights into degassing processing occurring on short timescales at Kīlauea's summit. [Online]. Available at: http://hilo.hawaii.edu/~kenhon/HawaiiChapman/documents/PKern2012HawaiiChapmanPoster.pdf*

Kern, C., Werner, C., Elias, T. Sutton, A.J., and Luebcke, P., 2013, Applying UV cameras for SO2 detection to distal or optically thick volcanic plumes, Journal of Geophysical Research, v. 262, p. 80–89.

Krueger, A.J. (1983). *Sighting of El Chichón sulfur dioxide clouds with the Nimbus 7 Total Ozone Mapping Spectrometer.* Science 220: 1377-1379

Larocque, A.C.L., Stimac, J.A., Keith, J.D., Huminicki, A.E. (2000). *Evidence for open-system behaviour in immiscible Fe-S-O liquids in silicate magmas: implications for contributions of metals and sulfur to ore-forming fluids.* The Canadian Mineralogist 38: 1233-1249

La Spina, A., M. Burton, P. Allard, S. Alparone, F. Mure. (2015) *Open-path FTIR spectroscopy of magma degassing processes during eight lava fountains on Mount Etna.* Earth and Planetary Science Letters. 2015; 413: 123-134.

Le Guern, F., Gerlach, T.M., Nohl, A. (1982). *Field gas chromatograph analyses of gases from a glowing dome at Merapi volcano, Java, Indonesia, 1977, 1978, 1979.* Journal of Volcanology and Geothermal Research 14: 223-245

Levelt, P.F., Van den Oord, G.H.J., Dobber, M.R., Mälkki, A., Visser, H., de Vries, J., Stammes, P., Lundell, J.O.V., Saari, H. (2006). *The Ozone Monitoring Instrument.* IEEE Transactions on Geoscience and Remote Sensing 44: 1093-1100

Lissauer, J.J. (1993). *Planet formation.* Annual Reviews Astronomy and Astrophysics 31: 129-172

Longpré, M-A., Stix, J., Burket, C., Hansteen, T., Kutterolf, S. (2014). *Sulfur budget and global climate impact of the A.D. 1835 Cosigüina volcano, Nicaragua.* Geophysical Research Letters 41: 6667-6675

Lopez, F., Nicolau, V., Maldague, X., Ibarra-Castanedo, C., (2013) *Advances in Signal Processing for Non Destructive Evaluation of Materials*. Proceedings of the VIIth International Works. 16th International Symposium on Applied Electromagnetics and Mechanics (ISEM 2013)

Love, S.P., Goff, F., Counce, D., Siebe, C., Delgado, H. (1998). *Passive infrared spectroscopy of the eruption plume at Popocatépetl volcano, Mexico.* Nature 396, 563-567

Lucey, P., Wilcox, B.B. (2003). *Mini-SMIFTS: an uncooled LWIR hyperspectral sensor.* Published in: Shen, S.S., Lewis, P.E., Imaging Spectrometry IX. Proceedings of the SPIE 5159: 275-282

Lucey, P.G., Horton, K.A., Williams, T. (2008) *Performance of a long-wave infrared hyperspectral imager using a Sagnac interferometer and an uncooled microbolometer array.* Apply. Optics, 47(28), F107-F113. <7700>

Lyakhovsky, V., Hurwitz, S., Navon, O. (1996). *Bubble growth in rhyolitic melts: experimental and numerical investigation.* Bulletin of Volcanology 58: 19-32

McCormick, B.T., Edmonds, M., Mather, T.A., Campion, R., Hayer, C.S.L., Thomas, H.E., Carn, S.A. (2013). *Volcano monitoring applications of the Ozone Monitoring Instrument.* Published in: Pyle, D.M., Mather, T.A., Biggs, J., *Remote sensing of volcanoes and volcanic processes: integrating observation and modelling.* Geological Society, London, Special Publication 380.

McKenzie, D., Nimmo, F. (1999). *The generation of Martian fluids by the melting of ground ice above dykes.* Nature 397, 231-233

Mader, H.M. (1998). *Conduit flow and fragmentation.* Published in: Gilbert, J.S., Sparks, R.S.J., *The physics of explosive volcanic eruptions.* Geological Society Special Publication

Martens, H., Naes, T. (1989). *Multivariate Calibration.* Wiley, New York. Z. Mathematical Reviews (MathSciNet): MR91e:62050

Mattu, M.J., G.W., Small, R.J., Combs, R.B., Knapp, R.T., Kroutil, (2000) *Quantitative Analysis of Sulfur Dioxide with Passive Fourier Tranform Infrared Remote Sensing Interferogram Data.* Applied Spectroscopy, 54, 341-348

Mc Gonigle, A.J.S., S. Inguaggiato, A. Aiuppa, A.R. Hayes, C. Oppenheimer. (2005). *Accurate measurements of volcanic SO2 flux: Determination of plume transport speed and integrated SO2 concentration with a single device.* Geochemistry, Geophysics, Geosystems. DOI: 10.1029/2004GC000845.

Mercalli, G. (1907). *I Vulcani attivi della Terra.* Lampi Di Stampa, 2011

Mertz, L. (1965) *Transformation in Optics.* Wiley, N.Y.

Mia, Md.B., Bromley, C.J., Fujimitsu, Y. (2012). *Heat flux using satellite based imagery at Karapiti ("Craters of the Moon") fumarole area, Tauopo, New Zealand.* Stanford University

Millán, M. (2008). *Absorption correlation spectrometry.* Published in: Williams-Jones, G., Stix, J., Hickson, C., *The COSPEC Cookbook: making SO_2 measurements at active volcanoes.* IAVCEI, Methods in Volcanology 1: 1-62

Minnett, P.J., Knuteson, R.O., Best, F.A., Osborne, B.J., Hanafin, J.A., Brown, O.B. (2000). The Marine-Atmospheric Emitted Radiance Interferometer: A High-Accuracy, Seagoing Infrared Spectroradiometer. Journal of Atmospheric and Ocean Technology 18: 994-1013

Moffat, A.J., Millan, M.M. (1971) *The applications of optical correlation techniques to the remote sensing of SO2 plumes using sky light.* Atmos Environ 5:677–690

Montmerle, T., Augereau, J-C., Chaussidon, M., Gounelle, M., Marty, B., Morbidelli, A. (2006). *Solar System formation and early evolution: the first 100 million years.* Earth, Moon and Planets 98: 39-95

Mori, T., M. Burton. (2006). *The SO2 camera: A simple, fast and cheap method for ground-based imaging of SO2 in volcanic plumes.* Geophysical Research Letters 33, L24804, doi:10.1029/2006GL027916.

Moore, G., Vennemann, T., Carmicheal, I.S.E. (1998). *An empirical model for the solubility of H_2O in magmas to 3 kilobars.* American Mineralogist 83: 36-42

Mori, T., Notsu, K., Tohjima, Y., Wakita, H. (1993). *Remote detection of HCl and SO_2 in volcanic gas from Unzen volcano, Japan.* Geophysical Research Letters 20: 1335-1358

Mori, T., M. Burton. (2009) *Quantification of the gas mass emitted during single explosions on Stromboli with the SO2 imaging camera.* Joruanl of Volcanology and Geothermal Research, 188, 395–400

Moffat, A.J., Millan, M.M. (1971) *The applications of optical correlation techniques to the remote sensing of SO2 plumes using sky light.* Atmos Environ 5:677–690

Noguchi, K., H. Kamiya. (1963) *Prediction of volcanic eruption by measuring the chemical composition and amounts of gases.* Bulletin of Volcanology 26, 367–378

Notsu, K., Mori, T., Igarishi, G., Tohjima, Y., Wakita, H. (1993). *Infrared spectral radiometer: a new tool for remote measurement of SO_2 of volcanic gas.* Geochemical Journal 27: 361

Oppenheimer, C., P. Francis, M. Burton, A.J.H. Maciejewski, L. Boardman. (1998) *Remote measurement of volcanic gases by Fourier Tranform infrared spectroscopy.* Applied Physics B Laser and Optics. 67, 505-515

Oppenheimer, C., McGonigle A. J. S., Allard P., Wooster M. J., and Tsanev V. (2004), Sulfur, heat, and magma budget for Erta 'Ale lava lake, Ethiopia, Geology, 32, 509–512, doi:10.1130/G20281.

Oppenheimer, C., P. Bani, J.A. Calkins, M.R. Burton, G.M. Sawyer. (2006) *Rapid FTIR sensing of volcanic gases released by Strombolian explosions at Yasur volcano, Vanuatu* Applied Physics B Laser and Optics. 85, 453-460

Parfitt, E., Wilson, L. (2008). *Fundamentals of physical volcanology.* Blackwell Publishing

Parks, M.M., Caliro, S., Chiodini, G., Pyle, D., Mather, T.A., Berlo, K., Edmunds, M., Biggs, J., Nomikou, P., Raptakis, C. (2013). *Distinguishing contributions to diffuse CO_2 emissions in volcanic areas from magmatic degassing and thermal decarbonation using soil gas ^{222}Rn-$\delta^{13}C$ systematics: application to Santorini volcano, Greece.* Earth and Planetary Science Letters 377, 378: 180-190

Pecsock, R.L., Schields, L.D. (1968). *Modern methods of chemical analysis.* Wiley, New York

Plank, M., Morton Maius, M.A. (1914). *The theory of heat radiation.* The Maple Press, York, Pennsylvania

Plutarchus, L.M. (c.100 AD). *De defectu oraculorum.* Published in: Plutarchus, L.M. *Moralia, volume 5*

Plutarchus, L.M. (c.100 AD). *De Pythiae Oraculis.* Published in: Plutarchus, L.M. *Moralia, volume 5*

Prata, J., C. Bernardo. (2014) *Retrieval of sulfur dioxide from a ground-based thermal infrared imaging camera* Atmospheric Measurement Techniques 7, 2807–2828

Raga, G.B., Baumgardner, D., Ulke, A.G., Brizuela-Torres, M., Kucienska, B. (2013). *The environmental impact of Puyehue-Cordón Caulle 2011 volcanic eruption on Buenos Aires.* Natural Hazards and Earth Systems Sciences 12: 2318-2330

Rampino, M.R., Ambrose, S.H. (2000). *Volcanic winter in the Garden of Eden: the Toba super eruption and the Late Pleistocene human population crash.* Published in: McCoy, F.W., Heiken, G., *Volcanic hazards and disasters in human antiquity.* Geological Society of America. Special Paper 345: 71-82

Realmuto, V.J., Worden, H.M. (2000). *Impact of atmospheric water vapor on the thermal infrared remote sensing of volcanic sulfur dioxide emissions: A case study from the Pu'u 'O'o vent of Kīlauea Volcano, Hawaii.* Journal of Geophysical Research vol. 105, no. B9, pages 21,497–21,508

Roman, C.D., Gardine, M.D. (2013). *Seismological evidence for long-term and rapidly accelerating magma pressurization preceding the 2009 eruption of Redoubt volcano, Alaska.* Earth and Planetary Science Letters 371, 372: 226-234

Rosipal, R., and N. Kramer (2006) Overview and recent advances in partial least squares. *Subspace, Latent Structure and Feature Selection: Statistical and Optimization Perspectives Workshop (SLSFS 2005), Revised Selected Papers (Lecture Notes in Computer Science 3940)*, pp. 34–51, Springer-Verlag, Berlin, Germany.

Scandone, R., Giacomelli, L. (2004). *Vulcanologia. Principi fisici e metodi di indagine.* Liguori

Schmidt, A. (2014). "*Volcanic gas and aerosol hazards from a future Laki-type eruption in Iceland*". Published in: Papale, P. and Shroder, J.F. (eds.) Volcanic hazards, risks and disasters. Elsevier, pp 377-397

Schmincke, H-U. (2004). *Volcanism.* Springer

Schwartz, T.A., Bunce, D.M., Silberman, R.G., Stanitsky, C.L., Stratton, W.J., Zipp, A.P. (1996). *Chemistry in context: applying chemistry to society.* Journal of Geochemical Education 72: A71

Self, S., Zhao, J-X., Holasek, R.E., Torres, R.C., King, A.J. (1999). *The atmospheric impact of the 1991 Mount Pinatubo eruption.* [Online] Available at: < http://pubs.usgs.gov/pinatubo/self/>, [Accessed on 11/14/2014]

Sellar, R.G., Boreman, G.D., Kirkland, L.E. (2002). *Comparison of signal collection abilities of different classes of imaging spectrometers.* Published in: Shen, S.S., *Spectrometry VIII.* Proceesings of the SPIE 4816: 389-396

Shinohara, H. (2008). *Excess deassing from volcanoes and its role on eruptive and intrusive activity.* Reviews of Geophysics 46: 4005

Sigurdsson, H. (1982). *Volcanic pollution and climate: the 1783 Laki eruption.* Eos, Transactions American Geophysical Union 63: 32

Sparks, R.S.J. (2003). *Dynamics of magma degassing.* Published in: Oppenheimer, C., Pyle, D.M., Barclay, J., *Volcanic degassing.* Geological Society, Special Publication 213: 5-22

Spiller, H.A., Hale, J.H., De Boer, J.Z. (2000). *The Delphic Oracle: a multidisciplinary defense of the gaseous vent theory.* Clinical Toxicology 40: 189-196

Stix, J., Gaonac'h, H. (2000). *Gas, plume, and thermal monitoring.* Published in: Sigurdsson, H., Houghton, B.F., McNutt, S.R., Rymer, H., Stix, J. (eds) Encyclopedia of Volcanoes, Academic Press, pp. 1141-1163

Sthoners, R.B. (1984). *The great Tambora eruption in 1815 and its aftermath.* Science 224, 1191-1198

Stoiber, R.E., Jepsen, A. (1973) *Sulfur dioxide contributions to the atmosphere by volcanoes.* Science 182:577–578

Stoiber, R.E., Malinconico, J.L.L.,Williams, S.N. (1983) *Use of the correlation spectrometer at volcanoes.* Published in: Tazieff, H., Sabroux, J.C. (eds) Forecasting volcanic events. Elsevier, New York, pp 424–444

Sun, W., Videen, G., Kato, S., Lin, B., Lukashin, C., Hu, Y. (2011). "*A study of subvisual clouds and their radiation effect with a synergy of CERES, MODIS, CALIPSO, and AIRS data*" Journal of Geophysical Research. doi: 10.1029/2011JD016422

Symonds, R.B., Rose, W.I., Bluth, G.J.S., Gerlach T.M. (1994). *Volcanic-gas studies: methods, results and applications.* Published in: Carroll, M.R., Holloway, J.R., *Volatiles in magmas.* Reviews in Mineralogy 30: 1-66

Symonds, R.B., Janik, C.J., Evans, C.W., Ritchie, B.E., Counce, D., Poreda, R.J., Iven, M. (2003). *Scrubbing masks magmatic degassing during repose at Cascade-range and Aleutian-arc volcanoes.* US Geological Survey, Open File Report 03-435

Swinbank, W.C. (1963). *Long-wave radiation from clear skies.* Quarterly Journal of the Royal Meteorological Society 89.381: 339-348.

Turcotte, D.L. (1982). *Magma migration.* Annual Reviews of Earth and Planetary Science 10: 397-408

University of Wyoming (2016). Upper Air Daily Soundings. [Online]. Available at: < http://weather.uwyo.edu/upperair/sounding.html >

VMAP: Vog Map and Prediction Project. (2013). *Vog model.* [Online]. Available at: <http://weather.hawaii.edu/vmap/hysplit/>, [Accessed on 10/20/2014]

Wallace, P., Carmichael, I.S.E. (1992). *Sulfur in basaltic magmas.* Geochimica et Cosmochimica Acta 56: 1863-1874

Wallace, P., Anderson, Jr., A.T. (2000). *Volatiles in magmas.* Published in: Sigurdsson, H., Houghton, B., McNutt, S.R., Rymer, H., Stix, J., *Encyclopedia of Volcanoes.* Academic Press, 149-170

Wallace, P.J. (2001). *Volcanic SO_2 emissions and the abundance and distribution of exsolved gas in magma bodies.* Journal of Volcanology and Geothermal Research 108: 85-106

Wallace, P.J. (2005). *Volatiles in subduction zone magmas: concentrations and fluxes based on melt inclusion and volcanic gas data.* Journal of Volcanology and Geothermal Research 140: 217-240

Wallace, P., Plank, T., Edmonds, M., Hauri, E.H. (2015) *Volatiles in Magmas.* Published in: Sigurdsson, H., Houghton, B.F., McNutt, S.R., Rymer, H., Stix, J. (eds) Encyclopedia of Volcanoes, second edition, Elseiver, pp. 168-183.

Waller, J.A., Simoni, D., Dance S. L. and Nichols N. K. (2016). *Diagnosing Observation Error Correlations for Doppler Radar Radial Winds in the Met Office UKV Model Using Observation-Minus-Background and Observation-Minus-Analysis Statistics.* American Meteorology Society. DOI: 10.1175/MWR-D-15-0340.1

Wardell, L. J., Kyle P. R., Dunbar N., and Christenson B. (2001), White Island volcano, New Zealand: Carbon dioxide and sulfur dioxide emission rates and melt inclusion studies, Chem. Geol., 177, 187–200.

Wardell, L.J., Kyle, P.R., Chaffin, C. (2004). *Carbon dioxide and carbon monoxide emission rates from an alkaline intra-plate volcano: Mt. Erebus, Antarctica.* Journal of Volcanology and Geothermal Research 131: 109-121

Watson, I.M., Realmuto, V.J., Rose, W.I., Prata, A.J., Bluth, G.J.S., Gu, Y., Bader, C.E., Yu, T. (2004). *Thermal infrared remote sensing of volcanoes emissions using the moderate resolution spectroradiometer.* Journal of Volcanology and Geothermal Research 135: 75-89

Weibring, P., Edner, H., Svanberg, S., Caltabiano, T., Condarelli, D., Cecchi, G., Pantani, L. (1998) *Monitoring of volcanic sulphur dioxide emissions using differential absorption lidar (DIAL), differential optical absorption spectroscopy (DOAS) and correlation spectroscopy (COSPEC). Appl Phys B 67:419-426*

Weibring, P., Swartling, J., Edner, H., Svanberg, S., Caltabiano, T., Condarelli, D., Cecchi, G., Pantani, L. (2002) *Optical monitoring of volcanic sulphur dioxide emissions: comparison between four differemy remote-sensing spectroscopic techniques. Opt Las El 37: 267-284*

Werner, C., Kelly, P., Doukas, M., Lopez, T., Pfeffer, M., McGimsey, R., Neal, C. (2013) *Degassing associated with the 2009 eruption of Redoubt Volcano, Alaska.* J.Volcanol. Geotherm. Res., doi:10.1016/j.jvolgeores.2012.04.012

Wetherill, G.W. (1980). *Formation of the terrestrial planets.* Annual review of astronomy and astrophysics 18: 77-113

Williams-Jones, G., Stix, J., Hickson, C. (2008). *The COSPEC Cookbook: making SO_2 measurements at active volcanoes.* IAVCEI, Methods in Volcanology 1

Williams-Jones, G., Stix, J., Nadeau, P.A. (2008). *Using the COSPEC in the field.* Published in: Williams-Jones, G., Stix, J., Hickson, C., *The COSPEC Cookbook: making SO_2 measurements at active volcanoes.* IAVCEI, Methods in Volcanology 1: 63-119

Wilson, L., Head, J.W. (1981). *Ascent and eruption of basaltic magma on the Earth and the Moon.* Journal of Geophysical Research 86: 2971-3001

Wilson, L., Walker, G.P.L. (1987). *Explosive volcanic eruptions VI. Ejecta dispersal in Plinian eruptions: the control of eruptions conditions and atmospheric properties.* Geophysical Journal of the Royal Astronomical Society 89: 657-679

Wright, R., Lucey, P., Crites, S., Horton, K., Wood, M., & Garbeil, H. (2013). BBM/EM design of the thermal hyperspectral imager: An instrument for remote sensing of earth's surface, atmosphere and ocean, from a microsatellite platform. Acta Astronautica, 87, 182-192.

Yang, H., Griffiths, P.R., Tate, J.D. (2003). *Comparison of partial least squares regression and multi-layer neural networks for quantification of nonlinear systems and application to gas phase Fourier transform infrared spectra.* Analytica Chimica Acta 489: 125-136

Young, S.R., Francis, P.W., Barclay, J., Casadevall, T.J., Gardner, C.A., Daroux, B., Davies, M.A., Delmelle, P., Norton, G.E., Maciejewski, A.J.H., Oppenheimer, C.M.M., Stix, J., Watson, I.M. (1988). *Monitoring SO_2 emission at the Soufriere Hills volcano: implications for changes in eruptive conditions.* Geophysical Research Letters 25: 3681-3684

Zuccaro, G., De Gregorio, D., Baxter, P. (2014). "*Human and Structural Vulnerability to Volcanic Processes*". Published in: Papale, P. and Shroder, J.F. (eds.) Volcanic hazards, risks and disasters. Elsevier, pp 261-288